INFLUENCE OF ELECTRODE GEOMETRY ON LOCAL AND GLOBAL IMPEDANCE RESPONSE

By

SHAO-LING WU

A DISSERTATION PRESENTED TO THE GRADUATE SCHOOL
OF THE UNIVERSITY OF FLORIDA IN PARTIAL FULFILLMENT
OF THE REQUIREMENTS FOR THE DEGREE OF
DOCTOR OF PHILOSOPHY

UNIVERSITY OF FLORIDA

2010

To my parents.

ACKNOWLEDGMENTS

I sincerely thank my advisor, Prof. Mark Orazem, who has always been patient and encouraging during my doctoral research at the University of Florida. Not only his enthusiasm and wide knowledge showed me the beauty of research in electrochemistry, but also his great personalities taught me to become a better person. The years I spent in the research group will definitely benefit the rest of my life.

I would like to thank Dr. Bernard Tribollet and Dr. Vincent Vivier from the CNRS Laboratory in Paris for their constant help and advices during various stages of this research work. I also thank Prof. Anuj Chauhan and Prof. Charles Martin for their suggestions on my proposal and dissertation. I thank my lovely group members, Vicky Huang, Sunil Roy, Patrick McKinney, Bryan Hirschorn, and Erin Patrick who gave me lots of memories during my doctoral years in the research group. I really appreciate their company and friendship.

My deepest gratitude goes to my family for their continuous love and support throughout my life. This dissertation is dedicated to them.

TABLE OF CONTENTS

LIST OF TABLES

LIST OF FIGURES

LIST OF SYMBOLS

Roman

A lumped parameter in expression for impedance response of reactions with adsorbed intermediate, S/cm^{2}s, see equation (4–14)

A constant used for the velocity expansion for a rotating disk in equations (6–12) and (6–13), $A = 0.934$

a constant used for the velocity expansion for a rotating disk in equations (6–10) and (6–11), $a = 0.51023$

B lumped parameter in expression for impedance response of reactions with adsorbed intermediate, 1/s, see equation (4–14)

B constant used for the velocity expansion for a rotating disk in equations (6–12) and (6–13), $B = 1.208$

b constant used for the velocity expansion for a rotating disk in equation (6–11), $b = 0.616$

b kinetic parameter, $\beta F/RT$ or $(1-\beta)F/RT$, V^{-1}

C_0 double-layer capacitance, μF/cm^2

c constant used for the velocity expansion for a rotating disk in equations (6–12) and (6–13), $c = 0.88447$

c_i concentration of species i, mol/cm^3

D_i diffusion coefficient of species i, cm^2/s

F dimensionless fluid velocity in the radial direction

F Faraday's constant, 96,487 C/equiv

f frequency, Hz

H dimensionless fluid velocity in the axial direction

I total current, A

i current density, A/cm^2

i_0 exchange current density, A/cm^2

i_{C}	double-layer charging current density, A/cm^2
i_{F}	Faradaic current density, A/cm^2
i_{lim}	mass-transfer-limited current density, A/cm^2
J	dimensionless exchange current density
j	complex number, $\sqrt{-1}$
K	dimensionless frequency
k	reaction rate constant, A/cm^2 or Acm/mol
n	number of electrons transferred in electrode reaction
N_i	flux of species i, mol/cm^{2}s
Q	CPE coefficient, s$^\alpha/\Omega$cm^2
q	surface charge density, C/cm^2
R	universal gas constant, 8.314 J/molK
r	radial distance, cm
r_0	radius of disk electrode, cm
R_{e}	electrolyte or Ohmic resistance, Ω or Ωcm^2
R_{t}	charge-transfer resistance, Ω or Ωcm^2
s_i	stoichiometric coefficient of species i
T	temperature, K
t	time, s
u_i	mobility of species i, cm^{2}mol/Js
$\mathbf{v}$	fluid velocity, cm/s
V	interfacial potential, V
V_0	equilibrium potential, V
v_r	fluid velocity in the radial direction, cm/s
v_y	fluid velocity in the axial direction, cm/s
y	axial distance, cm
Z	global impedance, Ω or Ωcm^2

Z_0 global interfacial impedance, Ω or Ωcm^2

Z_e global Ohimc impedance, Ω or Ωcm^2

Z_F global Faradaic impedance, Ω or Ωcm^2

z local impedance, Ωcm^2

z_0 local interfacial impedance, Ωcm^2

z_e local Ohmic impedance, Ωcm^2

z_F local Faradaic impedance, Ωcm^2

z_i charge associated with species i

Greek

α CPE exponent

α constant used in the interpolation function (6–15) to weigh the velocity expansions for a rotating disk

β symmetry factor

δ thickness, cm

ϵ dielectric constant

ϵ_0 permittivity of vacuum, 8.8542 $\times$ 10^{-14} F/cm

η total overpotential, V

η_c concentration overpotential, V

η_s surface overpotential, V

Γ maximum surface coverage, mol/cm^2

Γ_i surface excess concentration of species i, mol/cm^2

γ fractional surface coverage

κ electrolyte conductivity, S/cm

ν electrolyte viscosity, cm^2/s

Ω rotation speed of disk, rad/s

ω angular frequency, rad/s

Φ electric potential, V

ϕ phase angle, rad or degree

ζ dimensionless distance from the disk

General Notation

$\langle X \rangle$ averaged value of X over electrode surface

$\widetilde{X}$ oscillating part of $X(t)$

$\mathrm{Re}\{X\}$ real part of X

$\overline{X}$ steady-state part of $X(t)$

Subscripts

0 at the inner limit of diffusion layer

a anodic half reaction

c cathodic half reaction

d in the diffuse layer

ihp at inner Helmholtz plane

j imaginary part of impedance

m at metal surface

ohp at outer Helmholtz plane

r real part of impedance

∞ in the bulk solution or far away from electrode surface

Abstract of Dissertation Presented to the Graduate School
of the University of Florida in Partial Fulfillment of the
Requirements for the Degree of Doctor of Philosophy

INFLUENCE OF ELECTRODE GEOMETRY ON LOCAL AND GLOBAL IMPEDANCE RESPONSE

By

Shao-Ling Wu

August 2010

Chair: Mark E. Orazem
Major: Chemical Engineering

Distributions of current and potential associated with the electrode geometry are essential issues in studying the electrochemical systems. The nonuniform distributions that cause time-constant dispersion along the electrode surface can obscure results from the electrochemical measurements and lead to an incorrect interpretation of experimental data. The electrode configuration of interest is a disk electrode embedded in an insulator, which is one of the most popular geometries used in the electrochemical measurements. The geometry effect can be observed at high frequencies for a blocking disk electrode and for a disk electrode subject to a single Faradaic reaction. The present study involves more complicated electrode processes that include, first, a coupled Faradaic reactions by an adsorbed intermediate, and then incorporate the nonuniform mass transfer on a rotating disk electrode (RDE) for a general redox reaction.

On a stationary disk electrode, while the frequency or time-constant dispersion due to the dependence of the radial distribution of interfacial potential was shown to have an effect at high frequencies, the time-constant dispersion was also found to influence the impedance response at low frequencies due to the potential dependence of the fractional surface coverage of the adsorbed intermediate. The geometry effects were reflected in values for the local Ohmic impedance, which had complex behavior at both high and low frequencies. The dispersion of time constant was described in terms of a local constant-phase element (CPE) that represented the impedance response at low

frequencies as well as at high frequencies. The geometry effect can be eliminated by use of a recessed electrode on which the current and potential distributions are uniform. Experimental verification was obtained by applying local electrochemical impedance spectroscopy (LEIS) on an iron disk electrode immersed in a 1 M sulfuric acid solution.

The nonuniform mass transfer distribution together with the effect of electrode geometry was investigated on a RDE below the mass-transfer-limited current. A two-dimensional impedance model was proposed to study the influence of nonuniform current and potential distributions associated with both mass-transfer and Ohmic effects on the global and local impedance response. The concentration and potential distributions were calculated simultaneously throughout the system domain by taking into account the transport of species from diffusion, electric migration, and convection.

Under the assumption that the Faradaic reaction and the charging of the double layer cannot be separated *a priori*, part of the flux of reacting species contributes to the charging of the interface as well as to Faradaic reaction. A double-layer model following the Gouy-Chapman type of double layer was used to assess the charge density on electrode without specific adsorption, and to evaluate interfacial properties, such as the double-layer capacitance and the change of charge associated with the variation of ionic concentrations. The local interfacial impedance showed a depressed semicircle that cannot be attributed to the geometry-induced current and potential distributions. The appearance of CPE behavior was attributed to the frequency-dependent effective double-layer capacitance that accounted for the contribution of flux in charging the double layer.

CHAPTER 1
INTRODUCTION

Electrochemical impedance spectroscopy (EIS) is a transient technique that is widely used to characterize electrode process. Impedance measurement is performed by applying a small perturbation of potential or current to an electrochemical system at steady state and measuring the output response (current or potential) at different perturbation frequencies. The features of EIS include capturing the real-time changes of electrode process without destroying the specimen surface and also characterizing different electrode processes by their associated time constants within just one single measurement over a sufficient broad range of frequency.

While EIS is particularly useful to distinguish among transport and kinetic phenomena, geometry-induced current and potential distributions give rise to frequency dispersion that distorts the impedance response and could lead to an incorrect estimation of kinetic and transport parameters.[4] The frequency or time-constant dispersion was originally attributed to the dispersion of double-layer capacitance or the dependence of capacitance on frequency. It is now generally attributed to the nonuniform current and potential distributions associated with factors such as electrode morphology and heterogeneity.

Among all kinds of electrode, disk electrode is one of the popular geometries used in electrochemical measurements. The geometry of a disk electrode embedded in an insulator is simple to construct and easy to perform post processing on the electrode surface. The well-defined geometry also makes possible the analytical solutions for current and potential distributions, frequency dispersion, and fluid mechanics on a disk electrode.[1,5,6] The contributions related to the use of disk electrodes in the area of electrochemistry are shown in Figure 1-1. The amount of studies increases dramatically since the 1980's and keep increasing after 2000. The application of impedance technique accounts 10% of these work. Therefore, it is important to understand the effect of

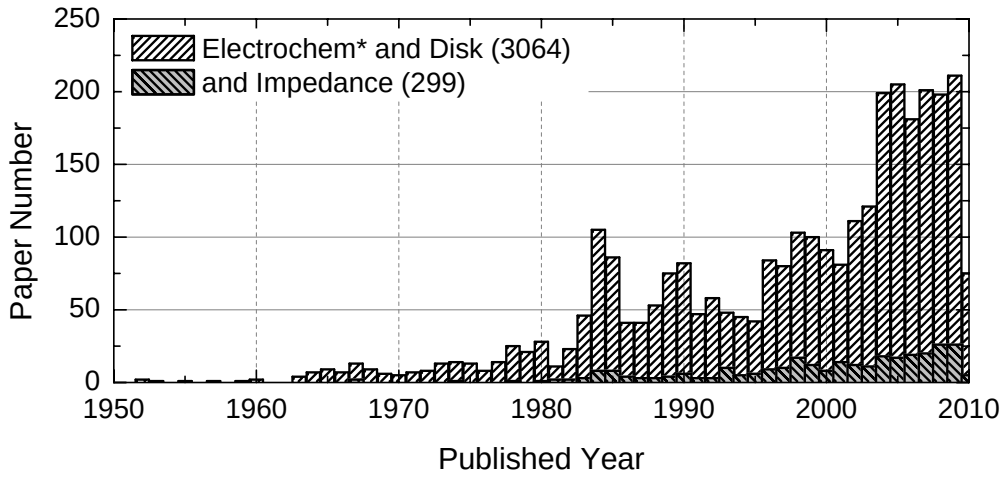

Figure 1-1. Online records for the use of disk electrodes in the area of electrochemistry provided by Engineering Village database before June, 2010.

disk geometry on impedance response and give a proper interpretation to experimental results.

Numerous approaches have been apply to study the transient behavior of a disk electrode in the presence of a time-constant dispersion. Analytical solutions were obtained for the transient potential and current responses under galvanostatic and potentiostatic control.[7–9] Numerical simulations facilitated the calculation of impedance response of a disk electrode that was ideally polarized[10,11] or was subject to a single Faradaic reaction.[12] Local electrochemical impedance spectroscopy (LEIS) could provide local information of electrode surface and confirm the variation of local impedance resulting from the nonuniform current and potential distributions.[2,13,14] The presence of geometry-induced current and potential distributions causes a depression of impedance plot that deviates from the standard semicircle. The measured global impedance, or the conventional impedance, cannot be properly interpreted by known electrical circuit elements such as resistor, capacitors, and inductors, and is generally expressed in terms of a constant-phase element (CPE) in equivalent circuits.

In this dissertation, fundamental concepts for the transient technique, EIS and LEIS, and the relevant issues such as geometry-induced current and potential distributions, and the origin of CPE behavior are presented in Chapter 2. Theoretical developments and simulation and experimental studies on the impedance response associated with nonuniform current and potential distributions on a disk electrode and mass-transfer distribution on a rotating disk electrode are reviewed in Chapter 3.

In a series of papers presented by Huang and coworkers,[10–12] the nonuniform current and potential distributions on a disk electrode were shown to influence the impedance response only at high frequencies. The work suggested experimentalists could avoid the associated complications by simply performing impedance measurements below a critical frequency given as a function of disk radius, disk capacitance, and solution conductivity. As an extension to this series of work, the objective of the present work is to investigate whether the geometry effect may also play a role at lower frequencies. The mathematical development, the calculated local and global impedance results, and the discussion on CPE behavior and complex Ohmic impedance are presented in Chapter 4. The impedance model is expected to predict experimental results and to provide guidelines of inspection and interpretation of the measured impedance data. An experimental verification performed on an iron disk electrode in acidic solution is presented in Chapter 5.

For reactions associated with mass transfer of reacting species, the current and potential distributions are affected by the nonuniform mass transfer on electrode. The rotating disk electrode (RDE) is used extensively in electrochemistry and the fluid mechanics is well understood. The current distribution is uniform only at the mass-transfer-limited current where the concentration of reacting species is equal to zero over the entire disk. One-dimensional models cannot account for the radial distribution of convective diffusion at currents below the limiting current.[15] Newman considered both the radial and axial distribution of mass transfer in a thin diffusion layer above electrode

surface. Two-term velocity expansions were used for fluid flow near the electrode surface. For exploring the nonuniform mass transfer in addition to the geometry effect on a RDE, a two-dimensional model is presented in Chapter 6 to account for the flux of each species in electrolyte associated with diffusion, migration, and convection. The system is treated as a single integral domain governed by the convective diffusion equation. An analytic velocity expression valid for the entire domain is developed using an appropriate interpolation function to weight inner and outer velocity expansions. This approach is preferable to dividing the domain of interest into a diffusion region near the electrode surface, and an outer region with uniform concentration as was done by Newman.[1] The steady-state analysis of the nonuniform current distribution below the mass-transfer-limited current can be used to explore the contribution of the radially dependent convective diffusion to the impedance response which is presented in Chapter 8.

Most impedance models assume negligible contribution of mass flux to the charging of electric double layer at the electrode-electrolyte interface, *i.e.,* the mass flux only contributes to the charge-transfer reactions. The assumption of the *a priori* separation of Faradaic and double-layer charging currents is relaxed in the present study. A simple double-layer model following the Gouy-Chapman theory is given in Chapter 7. The nonuniform mass and potential distributions result in a nonuniform charge distribution, and therefore a nonuniform distribution of double-layer capacitance in the interfacial region. The current and the flux of each species at electrode boundary are corrected by the presence of double-layer charging. The improved two-dimensional model is expected to provide a more general approach in assessing the impedance response on a RDE associated with the electrode geometry and mass-transfer effects. The impedance response with the correction of double-layer effect is also presented in Chapter 8.

CHAPTER 2
ELECTROCHEMICAL IMPEDANCE SPECTROSCOPY

Electrochemical impedance spectroscopy (EIS) is a powerful technique that has been widely used in studying the interfacial electrochemistry. The change of electrode properties are revealed during impedance measurements. The electrode process associated with reaction kinetics and surface morphology can therefore be diagnosed.

The impedance measurement involves the perturbation of an electrochemical system with a small sinusoidal signal and recording the output response. As shown in Figure 2-1, the output signal responds to the input signal with the same frequency and a phase shift. The conversion of the time-dependent signals into frequency domain gives the transfer function a complex feature. Impedance is therefore a complex quantity defined by the ratio of potential and current

$$Z = \frac{|\triangle V|}{|\triangle I|} e^{j\phi} = Z_r + jZ_j \tag{2–1}$$

where ϕ is the phase difference between the potential and current, j is a complex number equal to $\sqrt{-1}$, and Z_r and Z_j are the real and imaginary components of the impedance, respectively. If the potential and current are in phase, the impedance is a real number and is actually a resistance

$$Z_{\text{resistor}} = R \tag{2–2}$$

If the current leads or lags the applied potential by 90 degrees, the impedance is a pure imaginary number, which relates to capacitance or inductance by

$$Z_{\text{capacitor}} = \frac{1}{j\omega C} \tag{2–3}$$

and

$$Z_{\text{inductor}} = j\omega L \tag{2–4}$$

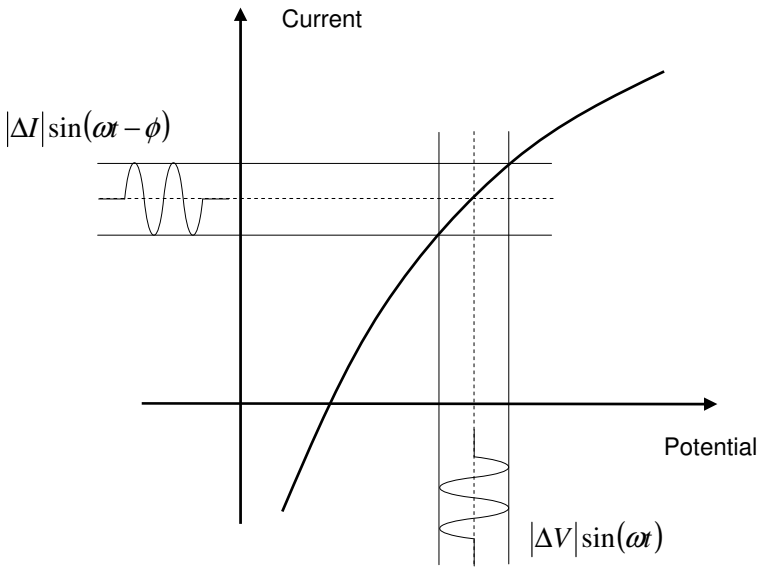

Figure 2-1. Perturbation of an electrochemical system at steady state with a small sinusoidal signal, where $\triangle V$ and $\triangle I$ represent the potential and current oscillating at the same frequency ω. The phase difference between potential and current is ϕ.

In an electrochemical system, the measured impedance is usually a complex number having real and imaginary components, which means that the system can be described by a combination of resisters, capacitors, and inductors.

Impedance data are often represented in a complex plane, which is also known as the Nyquist plot. Figure 2-2 shows a typical impedance plot corresponding to a RC circuit (the combination of a double-layer capacitance in parallel with a polarization resistance). The value of the polarization resistance can be read from the low-frequency limit. The characteristic frequency or time constant for the system

$$f = \frac{1}{2\pi\omega} = \frac{1}{2\pi RC} \tag{2–5}$$

can be obtained from the peak at which the negative value of imaginary part of the impedance is maximum. One of the attractive features of EIS is the characterization of different electrode processes by their associated time constants within one single measurement over a sufficient broad range of frequency. The transient response of

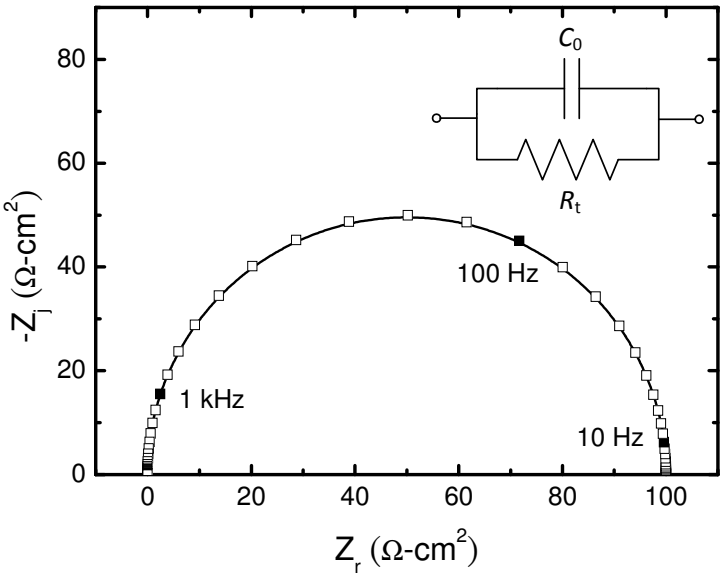

Figure 2-2. Nyquist plot of impedance data corresponding to a RC circuit of $R_{\mathrm{t}} = 100\Omega\text{-cm}^2$ and $C_0 = 10\mu\mathrm{F}/\mathrm{cm}^2$. The resistance from the electrolyte is not shown in this figure.

current and potential about their steady-state values gives the information of electron and mass transfer at the electrode-electrolyte interface. The charging of the electric double layer can be observed at high frequencies, and the diffusion of ionic species to the interfacial region is more significant at lower frequencies. Therefore, EIS is useful to distinguish among transport and kinetic phenomena.

While the impedance data given in Figure 2-2 traces a perfect semicircle, experimental data rarely show ideal behavior in real systems. The nonideal behavior for an electrode process is observed in the impedance plane of a depressed semicircle, which is difficult to be explained by simple circuit elements. The impedance data reflecting a nonuniform distribution of reactivity on electrode surface cab be described by using a constant-phase element (CPE) in equivalent circuits.

2.1 Constant-Phase Element

A constant-phase element literally means a circuit element that displays a constant phase angle, such as the resistor, capacitor, and inductor. The term, however, has been

specifically used to describe the nonideal behavior of the interfacial capacitance showing a frequency-dependent phase angle different from 90 degrees.[16] The impedance expression of the CPE is given by

$$Z_{\mathrm{CPE}} = \frac{1}{(j\omega)^{\alpha} Q} \tag{2–6}$$

where α and Q are constant. When $\alpha = 1$, Q has units of a capacitance, *i.e.,* F/cm^2, and resembles as an ideal capacitor. When $\alpha \neq 1$, Q has units of $\mathrm{s}^{\alpha}/\Omega$-cm^2. Usually, the electrochemical interface of a real cell is not ideal and behaves like a CPE in which the exponent α is between 0.5 and 1.

The nonideal behavior leading to a CPE can be attributed to the frequency or time-constant distribution along the area of the electrode or along the direction normal to the electrode surface. The surface distribution may arise from the surface heterogeneities such as different crystalline size or faces with different electrochemical characteristics.[17] A normal distribution may be attributed to the change of composition of oxide layers[18] or to the surface roughness and porosity.[19,20] The schematic representations for surface and normal distributions at electrode are given in Figure 2-3 by using equivalent circuits. The variations of reaction reactivity and double-layer capacitance at the electrode-electrolyte interface, and the variation of film properties in the oxide layer cause a frequency or time-constant distribution at electrode surface. This distributions are observed during the impedance measurements in the form of a CPE.

The presence of CPE behavior, however, is very common even for a homogenous and relatively smooth surface. The accessibility to the electrode surface could be constrained by the configuration of electrode with the surrounding insulator, and cause a geometry-induced time constant dispersion leading to CPE behavior.

2.2 Current and Potential Distributions

Current and potential distributions are essential properties of an electrode. Impedance response can be strongly influenced by the nonuniform distributions of

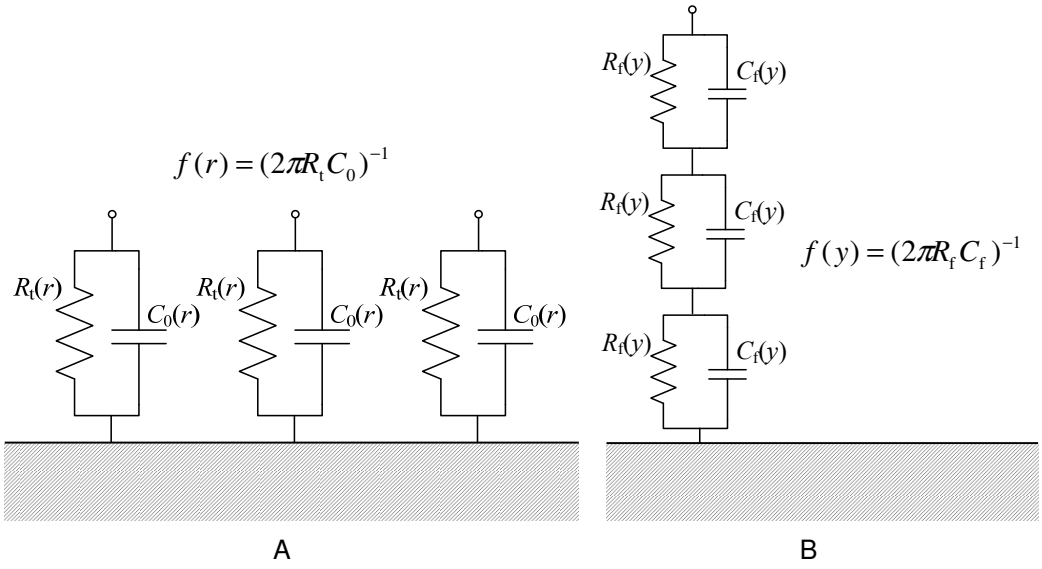

Figure 2-3. Schematic representation of a time-constant distribution A) at the electrode-electrolyte interface, and B) in the oxide layer, where R_t is the charge-transfer resistance, C_0 is the double-layer capacitance, and R_f and C_f are the resistance and capacitance of an oxide film.

current and potential associated with the geometry of electrode under study. One of the common geometries used in electrochemical measurements is a disk electrode embedded in an insulator. The geometry of the disk constrains the current flow and potential distribution in such a manner that both cannot simultaneously be uniform. Under the assumption of negligible concentration gradient, Newman[1,5] solved the Laplace's equation for potential using rotational elliptic coordinate. The distributions are considered to be primary or secondary depending on the presence of electrode polarization.

2.2.1 Primary Distribution

When the polarization resistance at electrode is small compared to the Ohmic resistance in electrolyte, the potential in solution adjacent to the electrode can be depicted by an equipotential surface. The current flows to electrode following the Ohm's law. This condition is taken as a primary distribution. The primary current distribution on

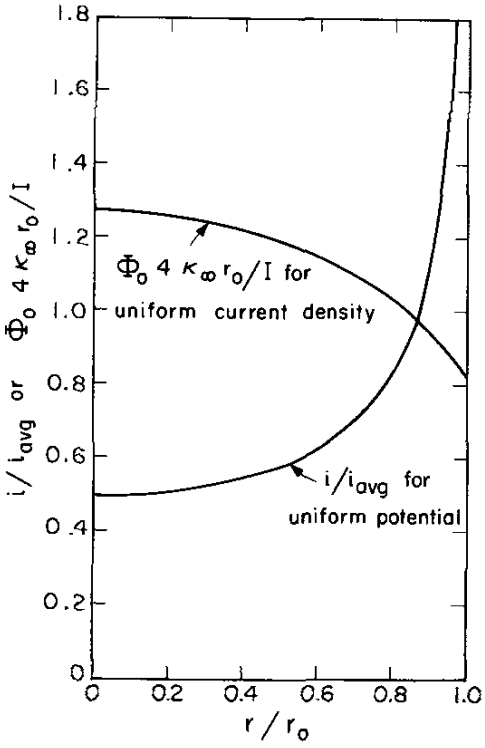

Figure 2-4. Primary current and potential distributions on a disk electrode.[1]

a disk electrode embedded in an infinite insulating plane is given by

$$\frac{i}{i_{\text{avg}}} = \frac{1}{2\sqrt{1-(r/r_0)^2}} \tag{2–7}$$

where r_0 is the radius of the disk, and i_{avg} is the average current density on the electrode. The total current to the disk is

$$I = 4\kappa_\infty r_0 \Phi_0 \tag{2–8}$$

where κ_∞ is the conductivity of the bulk solution, and Φ_0 is the potential is solution adjacent to the electrode surface. The analytical result shown in Figure 2-4 illustrates an infinite current density at the edge and half the value of average current density at the center of the disk when the electrode is subject to a uniform potential distribution. The primary distribution represents an extreme case where the Ohmic resistance dominates and the current distribution is the most nonuniform.

On the other hand, the primary potential distribution was calculated under the condition when the current is limited by the mass transfer of reacting species to the disk.[1] The potential curve in Figure 2-4 is normalized by the total current given in equation (2–8) so as to easily compare with the primary current distribution. A larger Ohmic potential drop is present at electrode center, and a smaller potential drop is observed at electrode periphery. The potential distributes in such a way that more current is forced to flow from the periphery to the center of the disk in order to maintain a uniform current density on the electrode surface as compared to the primary current distribution.

A classic solution for the Ohmic resistance on a disk electrode was provided by Newman[5] as

$$R_{\mathrm{e}} = \frac{1}{4\kappa_{\infty} r_0} \tag{2–9}$$

This simple form was obtained assuming that a hemispherical counter electrode is placed at infinity. The Ohmic resistance is only associated with the geometry factor of the disk, *i.e.,* the electrode radius, and the value of Ohmic resistance varies when the probe position changes.

2.2.2 Secondary Distribution

When electrode kinetics is taken into account, the potential adjacent to electrode is affected by the charge-transfer reactions taking place in the interfacial region, and can no longer be considered as an equipotential surface. The current is controlled by the Ohmic potential drop and the interfacial potential, and the distribution is taken as a secondary distribution.

The secondary current distribution were discussed in two cases where the electrode reactions follow the linear kinetics at small current densities, and the Tafel kinetics at larger current. In both cases, the current distributions are determined by the relative contribution from the charge-transfer resistance and the Ohmic resistance. A dimensionless parameter J was given to weigh the contribution from the two resistances

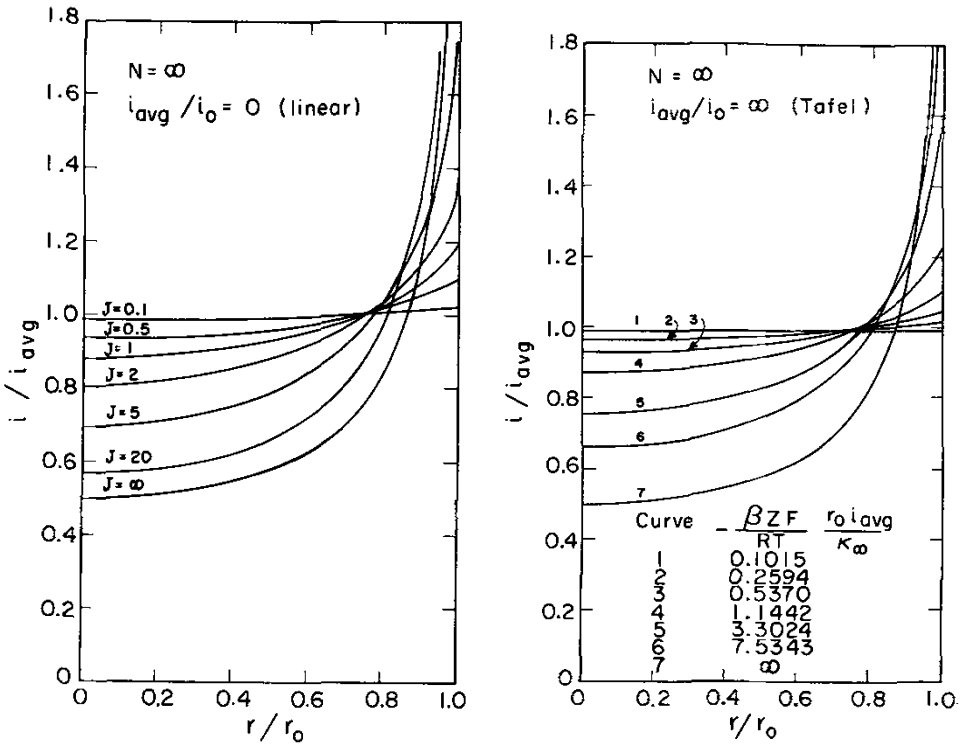

Figure 2-5. Secondary current distribution on a disk electrode for A) linear kinetics and B) Tafel kinetics.[1]

as

$$J = \frac{4}{\pi}\frac{R_e}{R_t} \tag{2–10}$$

Larger values of J are seen when the Ohmic resistance is important, and smaller values are seen when the system is dominated by slow electrode kinetics. The calculated secondary current distributions for linear and Tafel polarizations are shown in Figure 2-5 as a function of J. When J approaches infinity, fast kinetics applies and the Ohmic potential drop in solution dominates. The current under this condition is considered to be the primary distribution. When J approaches zero, a uniform current distribution is observed implying that the current is only dependent on the nature of the polarization reaction and not the electrode geometry.

2.2.3 Tertiary Distribution

Tertiary current and potential distributions apply when the assumption of uniform concentration is relaxed. The concentrations of charged species are now taken into account in addition to the potential. Newman[1] solved the convective diffusion equation for concentration within the diffusion layer, and the Laplace's equation for potential in the bulk solution. These equations were solved simultaneously and were coupled through the flux and current density at electrode boundary. A dimensionless parameter N, similar to J in the secondary distribution, was used in representing the relative importance of the Ohmic resistance and the mass-transfer resistance. More discussions on the effect of concentration polarization on the current and potential distributions are given elsewhere.[1,21]

The assumption of concentration variation only in the diffusion layer is relaxed in the present study. The approach made by Newman is modified by coupling the concentrations and potential through the mass conservation and charge conservation equations. The mathematical development and the calculation results for the current and potential distributions on a rotating disk electrode are presented in Chapter 6.

2.3 Local Electrochemical Impedance Spectroscopy

The results of conventional EIS represent an average response over the entire surface. Local impedance measurements provide local information of specimen surface and are useful in studying the time-constant distribution leading to a CPE behavior. The influence of electrode geometry on the impedance response were studied numerically and experimentally by Orazem and coworkers[2,3,10–14,22,23] in which the LEIS technique was used to confirm the resulting nonuniform behavior.

2.3.1 Experimental Configuration

The use of local electrochemical impedance spectroscopy (LEIS) was pioneered by Isaacs *et al.*[24–26] for the determination of surface heterogeneities. The technique

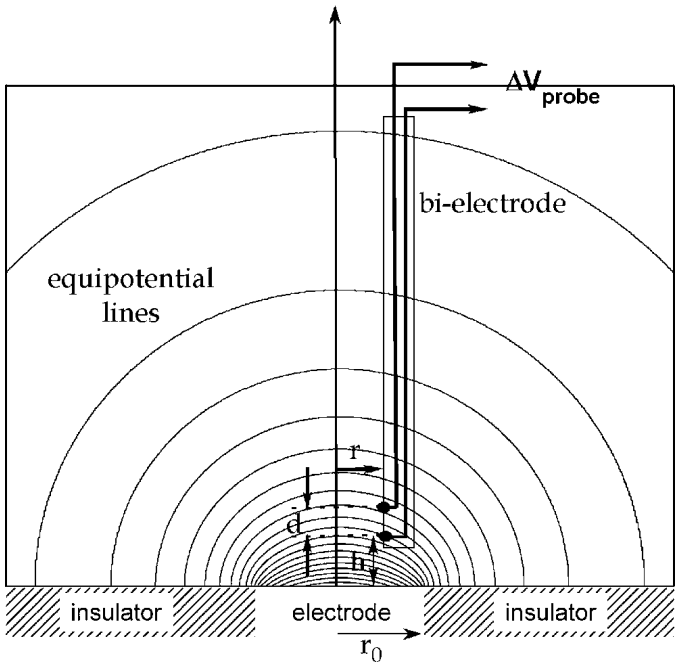

Figure 2-6. Schematic representation of the electrochemical cell used to perform local electrochemical impedance measurements.[2]

is performed with a bielectrode consisting of two platinum wires. The schematic representation of LEIS measurements is given in Figure 2-6. A perturbation of potential is applied to the electrode. The potential difference between the probes $\triangle V_{\mathrm{probe}}(\omega)$ are measured at different perturbation frequencies. The local current density $i_{\mathrm{loc}}(\omega)$ oscillated at the same frequency can be obtained through the Ohm's law following

$$i_{\mathrm{loc}}(\omega) = \frac{\triangle V_{\mathrm{probe}}(\omega)\kappa}{d} \tag{2–11}$$

where κ is the electrolyte conductivity, d is the distance between the probes, and ω is the oscillation frequency. The local impedance $z(\omega)$ is then defined by

$$z(\omega) = \frac{\widetilde{V}(\omega) - \Phi_{\mathrm{ref},\infty}}{i_{\mathrm{loc}}(\omega)} = \frac{\widetilde{V}(\omega)}{\triangle V_{\mathrm{probe}(\omega)}}\frac{d}{\kappa} \tag{2–12}$$

where $\widetilde{V}(\omega)$ is the perturbation of electrode potential and $\Phi_{\mathrm{ref},\infty}$ is the potential of reference electrode placed in the bulk solution.

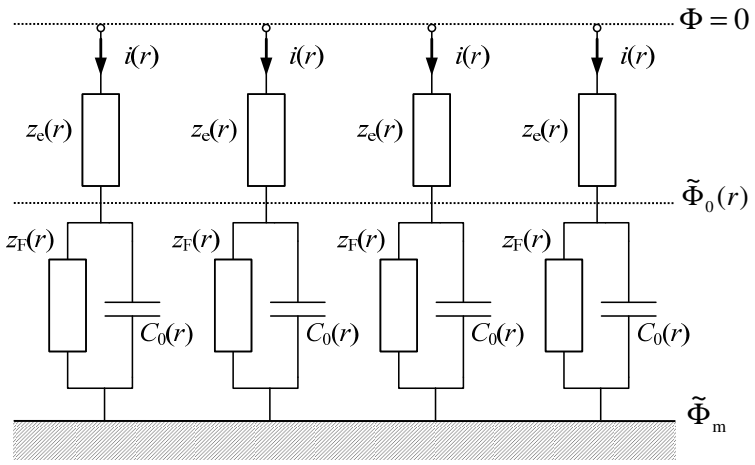

Figure 2-7. Local equivalent circuits correspond to local impedances that vary with the radial positions on the electrode surface.

The use of a bielectrode enables the measurement of local current density. The Commercial LEIS instrumentation yields a resolution with a dimension of about 1 mm. Custom-built instrumentation can yield resolutions on the order of 100 μm.[14,27] With a four-channel frequency response analyzer, the global and local impedances can be measured simultaneously.[11]

2.3.2 Definition of Terms

The notations of local impedance presented in this study follow the definitions proposed by Huang *et al.*[10] where the lower-case letter z was used to represent the local impedance, and the upper-case letter Z was used to represent the global impedance obtained from the conventional EIS measurements. To help envision the local and global properties, equivalent circuits are used to describe the interfacial electrochemistry. As seen in Figure 2-7 a series of equivalent circuits are present at the electrode surface. Each equivalent circuit corresponds to a local electrode process consisted of a double-layer capacitance in parallel with a Faradaic impedance. Blocks are used to stand for undetermined reaction mechanisms at the electrode surface. The electrolyte properties are also depicted by blocks in order to reflect the complex feature of the Ohmic contribution. The perturbation of electrode potential is denoted by $\widetilde{\Phi}_{\mathrm{m}}$, and the oscillation in

the adjacent solution in response to the electrode perturbation is denoted by $\widetilde{\Phi}_0$. The position of $\widetilde{\Phi}_0$ is located at the outer limit of the diffuse double layer. These potentials are referenced to a distant electrode which value is zero. The definitions of local and global impedances are given as follow using the conventions illustrated in Figure 2-7.

The local impedance variables are dependent on radial position along the electrode surface and are calculated from local current densities and potentials defined at different locations. The local impedance involves the electrode potential with respect to a distant electrode and is expressed by

$$z(r) = \frac{\widetilde{\Phi}_{\mathrm{m}}}{\widetilde{i}(r)} \tag{2–13}$$

where $\widetilde{i}$ is the oscillation of the local current density. The local interfacial impedance involves the potential difference across the electrode-electrolyte interface and is defined by

$$z_0(r) = \frac{\widetilde{\Phi}_{\mathrm{m}} - \widetilde{\Phi}_0(r)}{\widetilde{i}(r)} \tag{2–14}$$

The local Ohmic impedance involves the Ohmic potential drop in the solution and is given by

$$z_{\mathrm{e}}(r) = \frac{\widetilde{\Phi}_0(r)}{\widetilde{i}(r)} \tag{2–15}$$

From the definitions of the local impedance variables given above, the local impedance

$$z(r) = z_0(r) + z_{\mathrm{e}}(r) \tag{2–16}$$

can be represented by the sum of local interfacial and local Ohmic impedances.

The global impedance variables represent averaged properties of the electrode surface and are not dependent on radial positions. The global impedance, similar to the local impedance, involves the electrode potential with respect to the reference electrode placed far away from the disk, and is defined by

$$Z = \frac{\widetilde{\Phi}_m - \widetilde{\Phi}_0}{I} \tag{2–17}$$

where the oscillation of total current is related to the local current density by

$$I = \int_0^{r_0} \widetilde{i}(r) 2\pi r \mathrm{d}r \tag{2–18}$$

The global impedance can also be obtained from the local impedance values by

$$\frac{1}{Z} = \int_0^{r_0} \frac{1}{z(r)} 2\pi r \mathrm{d}r \tag{2–19}$$

which is actually the global admittance represent by the integration of local admittance over the disk surface. Following the same strategy, the global interfacial impedance can be obtained by integrating the local interfacial admittance

$$Z_0 = \left[\int_0^{r_0} \frac{1}{z_0(r)} 2\pi r \mathrm{d}r \right]^{-1} \tag{2–20}$$

The global Ohmic impedance is therefore defined to be

$$Z_e = Z - Z_0 \tag{2–21}$$

which is the difference between the global and global interfacial impedances. The high-frequency limit of the global impedance, which corresponds to the global Ohmic impedance, should reach a dimensionless value of 0.25 which is obtained from the analytical solution by Newman.[5]

CHAPTER 3
LITERATURE REVIEW

Impedance models are usually based on the assumption of uniformly active electrode surface. Electrochemical systems, however, rarely show an ideal behavior because the current and potential adjacent to the electrode are constrained by electrode geometry. Numerous studies were made to investigate the current and potential distributions associated with electrode geometry. A literature review is presented in this Chapter for the geometry-induced current and potential distributions and the nonuniform mass transfer on a rotating disk electrode.

3.1 Geometry-Induced Current and Potential Distributions

The current and potential distributions in the electrolyte adjacent to a disk electrode embedded in an insulating plane are constrained by the electrode geometry. Newman has shown that the Ohmic potential drop in solution causes a nonuniform current distribution at the electrode surface.[5] He also calculated the secondary current distribution, which accounts for the additional influence of the charge-transfer resistance.[1] The presence of potential drop across the electrode-electrolyte interface reduces the contribution from the Ohmic potential drop in solution and therefore makes the distributions of current and potential more uniform. Nisancioglu and Newman[7,8] have investigated the transient response of a disk electrode with a single Faradaic reaction subject to a step change in applied current and a step change in applied potential. The model did not account for mass transfer effects, and the analytical solution to the Laplace's equation was obtained using a transformation to rotational elliptic coordinates with a series expansion in terms of Legendre polynomials.

Geometry-induced current and potential distributions cause a frequency dispersion that distorts the impedance response and reflects a distribution of electrode reactivity.[6] The frequency or time-constant dispersion was originally attributed to the dispersion of double-layer capacitance or the dependence of capacitance on frequency. It is now

generally attributed to the nonuniform current and potential distributions associated with factors such as electrode morphology,[20] heterogeneity,[17] or composition variation in oxide layers,[18] and is generally expressed in terms of a constant phase element (CPE) in equivalent circuits.[16] The frequency dispersion resulting from electrode geometry is apparent in systems where the Ohmic resistance dominates, leading to a CPE behavior.

The nonuniform current and potential distributions could lead to an error in estimation of both the charge-transfer resistance and the interfacial capacitance.[4] Huang and coworkers[2,10–12] have presented a series of papers describing the influence of electrode geometry on the impedance response. They defined three local impedances in addition to the global impedance obtained from the usual impedance measurements. Simulations showed that the local impedance and local Ohmic impedance exhibited time-constant dispersion associated with the disk geometry, and the calculated global impedance had quasi-CPE behavior at high frequencies for blocking electrode[10,11] and electrodes subject to a single Faradaic reaction.[12] The geometry effect was reflected in the local Ohmic impedance in which nonzero imaginary components were observed. These effects can be eliminated by recording the impedance data below the characteristic frequency. Predictions made by Huang *et al.*[10–12] were in agreement with observations of Frateur *et al.*[2] for the local electrochemical impedance spectroscopy (LEIS) measurements on a stainless steel electrode. Jorcin *et al.*[13] also observed a CPE behavior on a disk electrode made of magnesium alloy that may be associated with a radial distribution of local resistance.

The origin of Ohmic impedance was discussed by Blanc *et al.*[23] The local variations of axial and radial current densities cause the Ohmic contribution to be represented by a complex number. The complex character of the Ohmic impedance is not only a property of electrolyte conductivity, but also a property of electrode geometry and interfacial impedance.

3.2 Nonuniform Mass Transfer on a Rotating Disk Electrode

The well-developed hydrodynamics and convective transport characteristics make rotating disk electrode (RDE) a popular tool to study the reaction kinetics and mass transfer in the diffusion layer. At the mass-transfer-limited current, the concentration of reacting species is zero over the entire surface of the disk and the convective fluid brings fresh reactant to the electrode surface. Under such condition, the current distribution may be uniform on the electrode surface and the fluid velocity in the radial direction can be neglected. Levich[28] calculated the mass-transfer-limited current by using the first term of velocity expansion in the axial direction,[29] which satisfies only when the Schmidt (Sc) number is infinitely large. Newman[30] provided a correction for a Sc number of 1,000 which reduced 3% of the value of limiting current from Levich's results.

The assumption of uniform current distribution was relaxed by Newman[1] by taking into account the concentration distribution in both radial and axial directions in the diffusion layer. The convective diffusion equation is given by

$$\upsilon_r \frac{\partial c}{\partial r} + \upsilon_y \frac{\partial c}{\partial y} = D \frac{\partial^2 c}{\partial y^2} \tag{3–1}$$

where c is the concentration and D is the diffusion coefficient of the reacting species, and υ_r and υ_y are the radial and axial components of the velocity which can be expressed by Cochran's[29] two-term expansion for fluid velocity near the electrode surface. Outside the diffusion layer assuming a uniform concentration in bulk solution, the electrolytic potential can be obtained from Laplace's equation following

$$\nabla^2 \Phi = 0 \tag{3–2}$$

The migration of species was modified by transference number. The nonuniform current distribution on electrode surface was then calculated for electrode reaction of metal

deposition. This approach was extended for general electrode reactions depending on both reactant and product concentrations.[31]

The steady-state solution for the uniform distributions of concentration and current cannot be applied to the development of impedance model due to the fact that impedance is a transient technique that relies on the perturbation of potential or current below the mass-transfer-limited current. Deslouis *et al.*[32,33] developed analytical solutions for the responses of current and potential to a sinusoidal perturbation of rotation speed, also known as electrohydrodynamic (EHD) impedance spectroscopy, at the mass-transfer-limited plateau. They used only the first term of the axial velocity expansion. The theoretical solutions were in agreement with the experimental results obtained from redox reactions with fast kinetics and large values of Sc number (Sc = 3,400 and 8,600). In the unsteady-state calculations, neglecting high order terms in the velocity expansion could result in a larger error when assessing the Sc number. For a Sc number of 1,000, an error of 24.4% was found,[34] which is more significant than that derived from steady-state calculations. Tribollet and Newman[15] used two terms of the velocity expansion in the derivation of EHD impedance and tabulated the Warburg impedance as a function of Sc number. The use of this look-up table reduces the time for regression to experimental results. The application of these one-dimensional models to impedance measurements, however, are not valid below the mass-transfer-limited current and often lead to anomalously large Sc numbers.

The nonuniform mass transfer on a RDE and the nonuniform Ohmic potential drop due to electrode geometry result to a distribution of current on electrode surface that requires a two-dimensional analysis at both steady and unsteady states. Appel and Newman[35] provided a mathematical model that considered the radial convective diffusion. The disk electrode was subject to a step change in concentration and the oscillating concentration distribution was calculated. This preliminary development, valid for infinite Sc number, could be used as part of a model for the influence of radially

dependent convective diffusion on the impedance response. Durbha and Orazem[36] extended the work to a steady-state treatment of current and potential distributions that accounted for a finite value of Sc number and for a distribution of charge in the diffuse part of double layer. Similar to Newman's calculation,[1] three terms of the radial and axial velocity expansions were used. In the subsequent work,[37] a two-dimensional impedance model was developed. Discrepancies were seen between the two-dimensional and one-dimensional models. Although the one-dimensional model provided a good fit to experimental data, the regressed Sc number could be as much as 22% higher than the expected value in cases where the discrepancy between models was significant.[38]

CHAPTER 4
ELECTRODE REACTION WITH ADSORBED INTERMEDIATES: MODEL

The behavior of adsorbed intermediates in Faradaic processes has been studied in the 1950s.[39,40] The procedures involving electrosorption steps in H_2 evolution or O_2 evolution reaction have an adsorption capacitance which is related to the coverage by intermediates dependent on electrode potential.[41] Epelbin and Loric[42] analyzed systems for metal dissolution and the measured impedances showed low-frequency inductive loops caused by adsorbed intermediates. The kinetics of reactions was discussed by Armstrong*et al.*[43] with considering the diffusion of species in solution and by Epelboin*et al.*[44] with more than one adsorbed species.

Systematic classifications of the impedance response for multi reactions involving an adsorbed intermediate under potentiostatic control was given by Armstrong and Edmondson[45] and Cao.[46] The high-frequency impedance loop is attributed to the charging of double layer and charge-transfer reactions at electrode surface, and the low-frequency loop is related to the relaxation of surface coverage by adsorbed intermediates.[44] Bai and Conway[47] discussed the dependence of impedance response on electrode potential and characterized the values of surface coverage at steady state. For a reversible reaction with two electron-transfer steps, the relative value of rate constant for each reaction step had an effect on the shape of impedance. Low-frequency inductive loops were observed in a narrow potential range near the maximum or minimum value of the surface coverage.

In this chapter, the geometry-induced current and potential distributions are applied to electrochemical systems with adsorbed intermediates. A general discussion for the influence of electrode geometry on the global and local impedance response is presented. This work is an extension of the previous studies for a blocking electrode,[10,11] and for electrode with single Faradaic reaction.[12] The objective of the present study is to

investigate whether the geometry effects may play a role at low frequencies where the relaxation of surface coverage is observed.

4.1 Mathematical Development

The approach presented here to account for low-frequency impedance loops associated with adsorbed intermediates was pioneered by Epelboin *et al.*[44,48] The first part of this section demonstrates that such low-frequency loops cannot be observed for reactions represented by linear kinetic expressions. The subsequent parts provides the model development under the assumption of Tafel kinetics and potential distribution constrained by electrode geometry.

4.1.1 Linear Kinetics near the Equilibrium Potential

The general reactions for two successive charge-transfer steps with an adsorbed intermediate can be described by

$$\mathrm{M} \rightleftharpoons \mathrm{X}^{+}_{\mathrm{ads}} + \mathrm{e}^{-} \tag{4–1}$$

and

$$\mathrm{X}^{+}_{\mathrm{ads}} \rightleftharpoons \mathrm{P}^{2+} + \mathrm{e}^{-} \tag{4–2}$$

Reactions near equilibrium potential can be expressed as linear functions of surface overpotential. Thus, the current density at the electrode surface for reactions (4–1) and (4–2) can be expressed by

$$i_{\mathrm{M}} = K_{\mathrm{M}}(1-\gamma)(b_{\mathrm{Ma}} + b_{\mathrm{Mc}})V \tag{4–3}$$

and

$$i_{\mathrm{X}} = K_{\mathrm{X}}\gamma(b_{\mathrm{Xa}} + b_{\mathrm{Xc}})V \tag{4–4}$$

where K_{M} and K_{X} are the effective rate constants, γ is the surface coverage by the adsorbed intermediate $\mathrm{X}^{+}_{\mathrm{ads}}$, V is the interfacial potential defined by the difference between the electrode potential Φ_{m} and the solution potential adjacent to the electrode

Φ_0, and b_{M} and b_{X} are kinetic parameters for reactions (4–1) and (4–2) where the subscripts a and c, respectively, represent the anodic and cathodic half reactions. The summation of the current density of each reaction yields the Faradaic current density as

$$i_{\mathrm{F}} = i_{\mathrm{M}} + i_{\mathrm{X}} \tag{4–5}$$

The variation of the surface coverage is related to the reaction rates as

$$\frac{\mathrm{d}\gamma}{\mathrm{d}t} = \frac{i_{\mathrm{M}} - i_{\mathrm{X}}}{\Gamma F} \tag{4–6}$$

where Γ is the maximum surface concentration by intermediate, and F is the Faraday constant. At steady state, the reaction rates reach constant values, and the surface coverage does not change with time, *i.e.,* $\mathrm{d}\gamma/\mathrm{d}t = 0$. The steady-state value of γ can therefore be calculated from equations (4–3) and (4–4) as

$$\bar{\gamma} = \frac{K_{\mathrm{M}}(b_{\mathrm{Ma}} + b_{\mathrm{Mc}})}{K_{\mathrm{M}}(b_{\mathrm{Ma}} + b_{\mathrm{Mc}}) + K_{\mathrm{X}}(b_{\mathrm{Xa}} + b_{\mathrm{Xc}})} \tag{4–7}$$

where the bar notation represents the steady-state condition. Equation (4–7) indicates that, in the linear regime, the steady-state surface coverage is not dependent upon the surface overpotential. The surface coverage remains uniform along the electrode and is a function of kinetic parameters only. The current density for each reaction, however, is a function of surface overpotential, and therefore the Faradaic impedance of the system is the charge-transfer resistance given by

$$R_{\mathrm{t}} = \frac{\partial \overline{V}}{\partial \bar{i}_{\mathrm{F}}} = \frac{1}{K_{\mathrm{M}}(1-\overline{\gamma})(b_{\mathrm{Ma}} + b_{\mathrm{Mc}}) + K_{\mathrm{X}}\overline{\gamma}(b_{\mathrm{Xa}} + b_{\mathrm{Xc}})} \tag{4–8}$$

As the Faradaic impedance is in parallel with the double-layer capacitance, the impedance diagram shows a single capacitive loop in the Nyquist plane. Inductive and capacitive loops are not evident at low frequencies under the assumption of linear kinetics. In order to investigate the influence of adsorbed intermediates on the impedance response, the electrode kinetics is assumed to be in the anodic Tafel regime.

4.1.2 Tafel Kinetics for Anodic Reactions

When the surface overpotential is large, the electrode behavior obeys Tafel kinetics. Reactions (4–1) and (4–2) are now taken to be irreversible as

$$\mathrm{M} \rightarrow {\mathrm{X}_{\mathrm{ads}}}^{+} + e^{-} \tag{4–9}$$

and

$${\mathrm{X}_{\mathrm{ads}}}^{+} \rightarrow \mathrm{P}^{2+} + e^{-} \tag{4–10}$$

The reactant could be a metal M which dissolves through an adsorbed intermediate ${\mathrm{X}_{\mathrm{ads}}}^{+}$, and then further reacts to form the final product P^{2+}. Similar mechanisms were proposed by Epelboin and Keddam[48] for calculating the impedance of iron dissolution through two steps involving an adsorbed FeOH intermediate, and by Peter *et al.*[49] for the impedance model of the dissolution of aluminum in three consecutive steps with two adsorbed intermediates. Under the assumption of Tafel kinetics and negligible diffusion processes, the steady-state current densities for reactions (4–9) and (4–10) are expressed by

$$\bar{i}_{\mathrm{M}} = K_{\mathrm{M}}(1-\overline{\gamma})\exp[b_{\mathrm{M}}\overline{V}] \tag{4–11}$$

and

$$\bar{i}_{\mathrm{X}} = K_{\mathrm{X}}\overline{\gamma}\exp[b_{\mathrm{X}}\overline{V}] \tag{4–12}$$

The expression for steady-state surface coverage can be calculated from equations (4–11) and (4–12) as

$$\overline{\gamma} = \frac{K_{\mathrm{M}}\exp[b_{\mathrm{M}}\overline{V}]}{K_{\mathrm{M}}\exp[b_{\mathrm{M}}\overline{V}] + K_{\mathrm{X}}\exp[b_{\mathrm{X}}\overline{V}]} \tag{4–13}$$

In contrast to the surface coverage given in equation (4–7) for linear kinetics, equation (4–13) shows that the steady-state surface coverage is dependent on the surface overpotential under the assumption of Tafel kinetics.

Following the method developed by Epelboin *et al.*,[44] the Faradaic impedance Z_{F} at a given potential is given by

$$\frac{1}{Z_{\mathrm{F}}} = \frac{1}{R_{\mathrm{t}}} + \frac{A}{j\omega + B} \tag{4–14}$$

where the charge-transfer resistance R_{t} is defined by

$$\frac{1}{R_{\mathrm{t}}} = \frac{1}{R_{\mathrm{t,M}}} + \frac{1}{R_{t,\mathrm{X}}} = b_{\mathrm{M}}|\bar{i}_{\mathrm{M}}| + b_{\mathrm{X}}|\bar{i}_{\mathrm{X}}| \tag{4–15}$$

and parameters A and B are potential dependent variables given by

$$A = \frac{\partial \bar{i}_F}{\partial \overline{\gamma}} \frac{\partial}{\partial \overline{V}} \left(\frac{\mathrm{d}\gamma}{\mathrm{d}t}\right) = \frac{(R_{t,\mathrm{M}}^{-1} - R_{t,\mathrm{X}}^{-1})[K_{\mathrm{X}} \exp(b_{\mathrm{X}}\overline{V}) - K_{\mathrm{M}} \exp(b_{\mathrm{M}}\overline{V})]}{\Gamma F} \tag{4–16}$$

and

$$B = -\frac{\partial}{\partial \overline{\gamma}} \left(\frac{\mathrm{d}\gamma}{\mathrm{d}t}\right) = \frac{K_{\mathrm{X}} \exp(b_{\mathrm{X}}\overline{V}) + K_{\mathrm{M}} \exp(b_{\mathrm{M}}\overline{V})}{\Gamma F} \tag{4–17}$$

While B is always positive, the sign of A varies with the potential across the electrode-electrolyte interface, and the feature of the impedance plane changes according to the sign of A.

As shown in Figure 4-1 for the Faradaic impedance Z_{F} in parallel with the double layer capacitance C_0 at electrode surface, and in series with the Ohmic resistance R_{e} in electrolyte, the overall impedance has different features at low frequencies with different signs of A. At high frequencies, the Faradaic impedance is observed through the charge-transfer resistance R_{t}, which is the first term of equation (4–14), and the impedance shows a high-frequency capacitive loop corresponding to R_{t} in parallel with C_0 ($R_{\mathrm{t}}||C_0$). At low frequencies, the Faradaic impedance is observed through the second term of equation (4–14). The low-frequency loop exhibits inductive behavior when A is positive, and capacitive behavior when A is negative. When A is equal to zero, the two terms of the numerator in equation (4–16) cancel, *i.e.,* $\partial \bar{i}_{\mathrm{F}}/\partial \overline{\gamma} = 0$. In this case, the reaction current density is not dependent on the surface coverage, and, therefore, the impedance plot shows a single capacitive loop corresponding to $R_{\mathrm{t}}||C_0$ with no low-frequency loop.

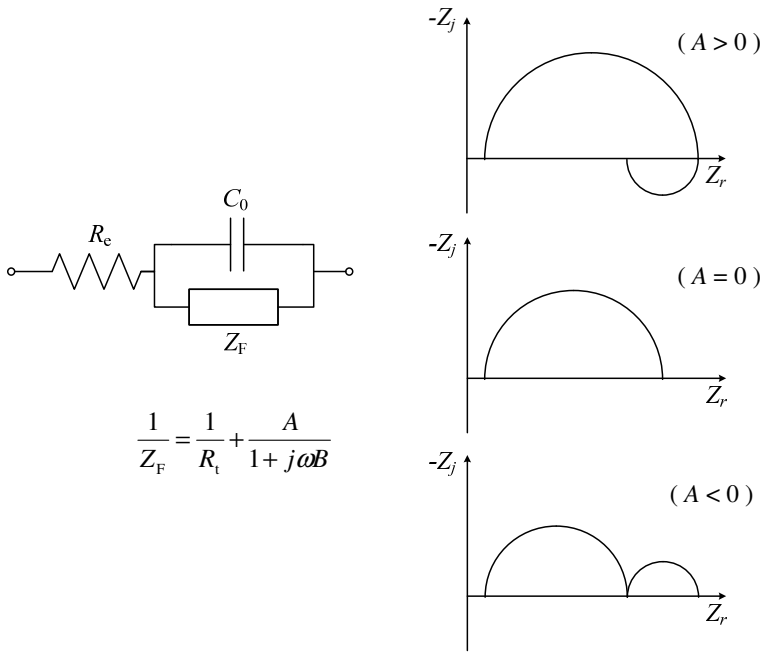

Figure 4-1. Impedance plots in response to different signs of A.

4.1.3 Potential Distribution

The potential distribution implied by Figure 2-7 results from the geometry of a disk electrode with radius r_0 embedded in an insulating plane. The counterelectrode was assumed to be placed infinitely far from the disk electrode. The potential in the solution can be solved by using Laplace's equation in cylindrical coordinates, *i.e.,*

$$\nabla^2 \Phi = 0 \tag{4–18}$$

The system is assumed to have cylindrical symmetry such that the potential in solution is dependent only on the radial position (r) along the electrode surface and the normal distance (y). In response to an alternating current with a particular angular frequency ω ($\omega = 2\pi f$), the potential can be separated into steady and time-dependent parts as

$$\Phi = \overline{\Phi} + Re\{\widetilde{\Phi} e^{j\omega t}\} \tag{4–19}$$

where $\overline{\Phi}$ is the steady-state solution for potential and $\widetilde{\Phi}$ is the complex oscillating component, which is a function of position only. Therefore, Laplace's equation becomes

$$\frac{1}{r}\frac{\partial}{\partial r}(r\frac{\partial\widetilde{\Phi}}{\partial r})+\frac{\partial^2\widetilde{\Phi}}{\partial y^2}=0 \tag{4–20}$$

The boundary conditions at insulators and far from the electrode surface are given by

$$\left.\frac{\partial\widetilde{\Phi}}{\partial y}\right|_{y=0}=0 \qquad \text{at } r>r_0 \tag{4–21}$$

and

$$\widetilde{\Phi}=0 \qquad \text{as } r^2+y^2\to\infty \tag{4–22}$$

The current density at the electrode surface can be expressed as

$$i=C_0\frac{\partial V}{\partial t}+i_{\mathrm{M}}+i_{\mathrm{X}}=-\kappa\left.\frac{\partial\Phi}{\partial y}\right|_{y=0} \tag{4–23}$$

where C_0 is the interfacial capacitance and κ is the electrolyte conductivity.

The current at the electrode surface can be written by use of the reaction kinetics developed in equations (4–11) and (4–12), and expressed in frequency domain by

$$Kj\widetilde{V}+J_1\widetilde{V}+J_2\widetilde{V}=-r_0\left.\frac{\partial\widetilde{\Phi}}{\partial y}\right|_{y=0} \tag{4–24}$$

where $\widetilde{V}$ is the oscillation of surface overpotential defined by

$$\widetilde{V}=\widetilde{\Phi}_{\mathrm{m}}-\widetilde{\Phi}_0 \tag{4–25}$$

where $\widetilde{\Phi}_{\mathrm{m}}$ is the imposed perturbation in electrode potential and $\widetilde{\Phi}_0$ is the corresponding oscillation in the solution potential adjacent to electrode surface, and K is the dimensionless frequency defined by

$$K=\frac{\omega C_0 r_0}{\kappa} \tag{4–26}$$

The parameters J_1 and J_2 are dimensionless functions dependent on angular frequency and radial position on the electrode surface, *i.e.,*

$$J_1(r,\omega) = J_{\mathrm{M}}(r) - \frac{\frac{|\bar{i}_{\mathrm{M}}(r)|}{1-\overline{\gamma}(r)}[J_{\mathrm{M}}(r) - J_{\mathrm{X}}(r)]}{\Gamma F j\omega + \frac{|\bar{i}_{\mathrm{M}}(r)|}{1-\overline{\gamma}(r)} + \frac{|\bar{i}_{\mathrm{X}}(r)|}{\overline{\gamma}(r)}} \tag{4–27}$$

and

$$J_2(r,\omega) = J_{\mathrm{X}}(r) - \frac{\frac{|\bar{i}_{\mathrm{X}}(r)|}{\overline{\gamma}(r)}[J_{\mathrm{M}}(r) - J_{\mathrm{X}}(r)]}{\Gamma F j\omega + \frac{|\bar{i}_{\mathrm{M}}(r)|}{1-\overline{\gamma}(r)} + \frac{|\bar{i}_{\mathrm{X}}(r)|}{\overline{\gamma}(r)}} \tag{4–28}$$

The parameters J_{M} and J_{X} are defined to be the dimensionless current densities for reactions (4–9) and (4–10), respectively, and are functions of radial position on the electrode surface, as given by

$$J_{\mathrm{M}}(r) = \frac{b_{\mathrm{M}}|\bar{i}_{\mathrm{M}}(r)|r_0}{\kappa} \tag{4–29}$$

and

$$J_{\mathrm{X}}(r) = \frac{b_{\mathrm{X}}|\bar{i}_{\mathrm{X}}(r)|r_0}{\kappa} \tag{4–30}$$

respectively. The sum of J_{M} and J_{X} represents the dimensionless current density which flows through the charge-transfer steps

$$J(r) = J_{\mathrm{M}}(r) + J_{\mathrm{X}}(r) = \frac{r_0}{\kappa}[K_{\mathrm{M}} b_{\mathrm{M}}(1-\overline{\gamma})\exp(b_{\mathrm{M}}\overline{V}) + K_{\mathrm{X}} b_{\mathrm{X}}\overline{\gamma}\exp(b_{\mathrm{X}}\overline{V})] \tag{4–31}$$

The relationship between the parameter J and the charge-transfer and Ohmic resistances can be established using the high-frequency limit for the Ohmic resistance to a disk electrode obtained by Newman[5]

$$R_e = \frac{\pi r_0}{4\kappa} \tag{4–32}$$

where R_{e} has units of Ω cm^2. The parameter J can therefore be expressed in terms of the Ohmic resistance R_{e} and charge-transfer resistance R_{t} as[12]

$$J = \frac{4}{\pi}\frac{R_{\mathrm{e}}}{R_{\mathrm{t}}} \tag{4–33}$$

Table 4-1. The values of kinetic parameters used for the simulations.

Symbol	Meaning	Value	Units
b_{M}	$\alpha_{\mathrm{M}}F/RT$	40	V^{-1}
b_{X}	$\alpha_{\mathrm{X}}F/RT$	10	V^{-1}
K_{M}	Effective reaction constant for reaction (4–9)	77.2	A/cm^2
K_{X}	Effective reaction constant for reaction (4–10)	0.19	A/cm^2
$\overline{\Phi}_{\mathrm{m}}$	Steady-state electrode potential		
	For $\langle A\rangle > 0$ (0.011 S/cm^{2}s)	-0.15	V
	For $\langle A\rangle = 0$ (-6.6×10^{-4} S/cm^{2}s)	-0.10	V
	For $\langle A\rangle < 0$ (-0.83 S/cm^{2}s)	0.10	V
$\widetilde{\Phi}_{\mathrm{m}}$	Perturbation of electrode potential	0.01	V

Large values of J are seen when the Ohmic resistance is much larger than the charge-transfer resistance, and small values of J are seen when the charge-transfer resistance dominates. The definition of parameter J in equation (4–33) is the reciprocal of the Wagner number,[50] which is a dimensionless quantity that measures the uniformity of the current distribution in an electrolytic cell.

Simulations were performed to investigate the electrochemical impedance behavior for different potentiostatic situations when the surface-average value of $\langle A\rangle$ is positive, negative, and zero. The values of kinetic parameters used for the simulations are given in Table 4-1. The values in Table 4-1 for b_{M} and b_{X} are close to the values of 38.4 V^{-1} and 7 V^{-1} reported by Keddam *et al.*[51] for the dissolution of iron in acidic media. The calculated result for each simulation corresponds to a particular value of J, representing different contributions from the Ohmic and the charge-transfer resistances. The equations were solved by using the finite-element package *COMSOL Multiphysics*® with the conductive media DC module in a 2D axial symmetric coordinate system. A quarter-circle was constructed with an axis of symmetry at $r = 0$ and the electrode positioned at $y = 0$. The domain size shown in Figure 4-2 was 2,000 times larger than the disk electrode dimension in order to meet the assumption that the counterelectrode was located infinitely far from the electrode surface.

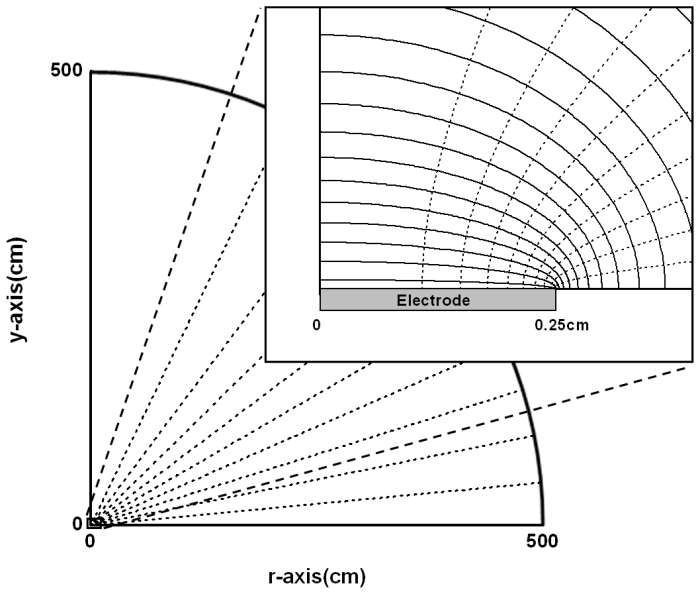

Figure 4-2. The domain used for the finite-element simulations. The solid lines represent steady-state iso-potential planes, and dashed lines represent steady-state trajectories for flow of current.

4.2 Calculated Impedance Results

As indicated by equation (4–13), the steady-state fraction of surface coverage varies with the interfacial potential ($\overline{V} = \overline{\Phi}_{\mathrm{m}} - \overline{\Phi}_0$). While $\overline{\Phi}_{\mathrm{m}}$ is assumed to be uniform on a conductive electrode, the potential outside the diffuse double layer $\overline{\Phi}_0$ is a function of radial position. Thus, $\overline{\Phi}_{\mathrm{m}} - \overline{\Phi}_0$ and $\overline{\gamma}$ are functions of radial position. The distribution of the normalized steady-state fractional surface coverage is presented in Figures 4-3A and 4-3B for positive and negative average values of $\langle A \rangle$, respectively. The value of average surface coverage $\langle \overline{\gamma} \rangle$ is 0.069 for curve 1, and 0.98 for curve 9. The parameter A is itself a function of radial position due to its dependence on interfacial potential. The range of the value of A from electrode center to electrode periphery is 0.0109 to 0.00509 S/cm^{2}s for curve 4, 0.0106 to -0.0665 S/cm^{2}s for curve 5, and -0.109 to -7.60 S/cm^{2}s for curve 6. The variation for local value A along the electrode surface is larger as the applied potential is increased.

The relationship between the surface-averaged values of $\langle A \rangle$ reported in Figures 4-3A and 4-3B and the applied steady-state electrode potential is presented in Figure

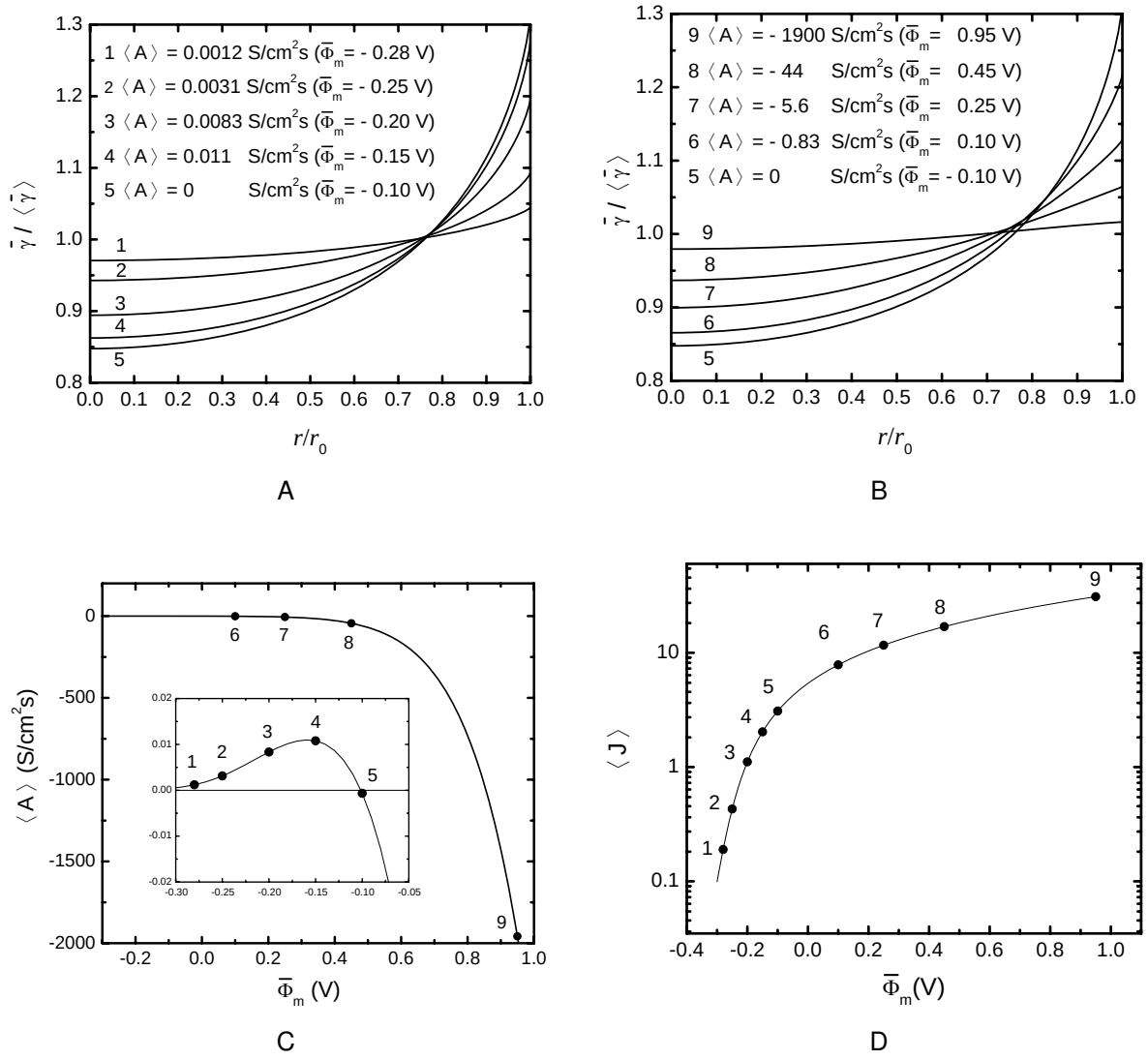

Figure 4-3. Radial distribution of the normalized steady-state fractional surface coverage on a disk electrode: A) for positive surface-averaged values of $\langle A \rangle$; B) for negative surface-averaged values of $\langle A \rangle$; C) the relationship between the surface-averaged values of $\langle A \rangle$ reported in parts (A) and (B) and the applied steady-state electrode potential; and D) the corresponding surface-averaged values of $\langle J \rangle$ to the applied steady-state electrode potential.

4-3C. The coverage by intermediate is most nonuniform at $\overline{\Phi}_{\mathrm{m}} =$ -0.1 V, where the corresponding average value of $\langle A \rangle$ is equal to zero. It becomes more uniform at larger or smaller values of $\overline{\Phi}_{\mathrm{m}}$. The corresponding surface-averaged value of $\langle J \rangle$ to the applied potential at steady state was calculated from equation (4–31) and is given in Figure 4-3D. As $\overline{\Phi}_{\mathrm{m}}$ increases, the value of $\langle J \rangle$ increases and the sign of $\langle A \rangle$ changes from positive to negative. The sign of $\langle A \rangle$ determines the shape of low-frequency features of the impedance plot. In order to understand the impedance behavior under different potentiostatic conditions, three cases for $\langle A \rangle > 0$, $\langle A \rangle = 0$, and $\langle A \rangle < 0$ (points 4, 5, and 6 in Figure 4-3C) are discussed.

The maximum variability of surface coverage was shown in Figures 4-3A and 4-3B to occur for $\langle A \rangle = 0$. Interestingly, the potential yielding the maximum variability of surface coverage does not coincide with the potential yielding the most nonuniform distribution of current or potential. The adsorption isotherm given in Figure 4-4A shows an inflection at $\langle A \rangle = 0$, representing the stronger dependence of the surface coverage on the interfacial potential; whereas, at $\langle A \rangle = -0.83$ S/cm^{2}s, the isotherm crosses the largest potential interval, indicating the most nonuniform potential distribution on the electrode surface. The distribution of current can also be observed in Figure 4-4B, which shows a more nonuniform distribution of current when the applied potential is increased. For $\langle A \rangle = -0.83$ S/cm^{2}s, the parameter J has the largest value, meaning, as shown in equation (4–33), that the Ohmic resistance is much larger than the charge-transfer resistance. Hence the current distribution is more nonuniform.[21]

The discussion presented below follows the influence of kinetic parameters on the global, local interfacial, local Ohmic, and local impedances.

4.2.1 Global Impedance

The global impedance represents an averaged response of the electrode. The calculated results of global impedance for the cases with $\langle A \rangle > 0$ (0.011 S/cm^{2}s), $\langle A \rangle = 0$, and $\langle A \rangle < 0$ (-0.83 S/cm^{2}s) are presented in Nyquist format in Figures 4-5A,

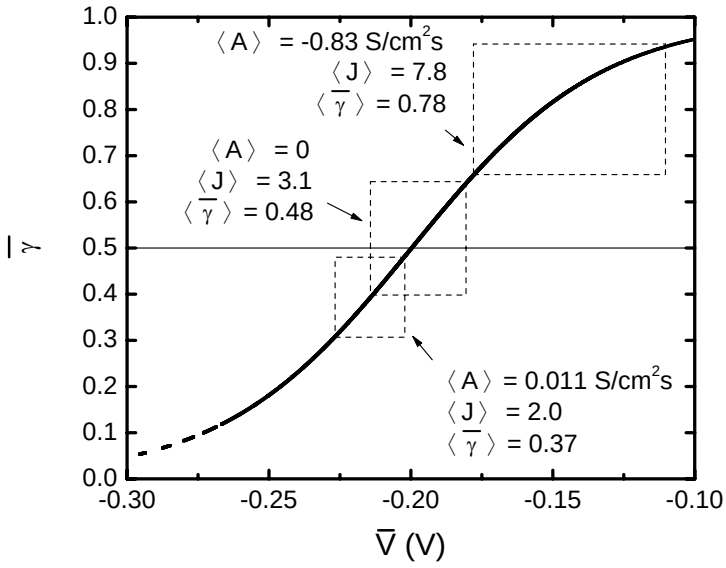

A

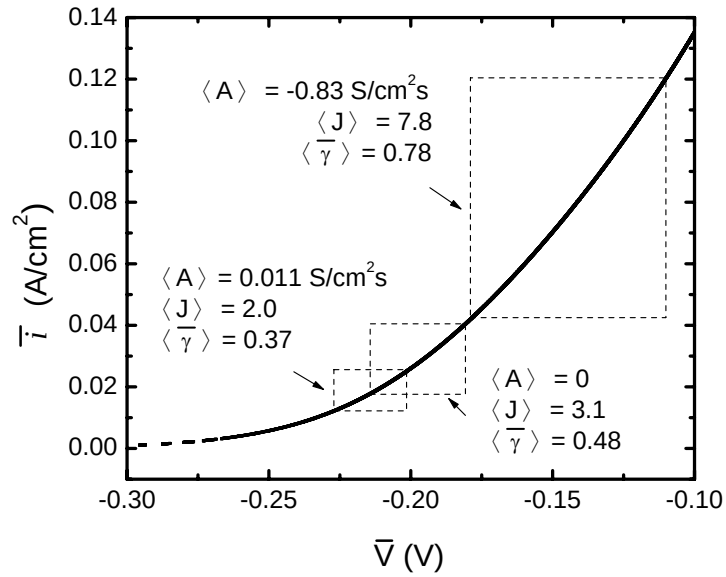

B

Figure 4-4. The variation of A) steady-state surface coverage density, and B) steady-state current density with the interfacial potential. Dashed squares are used to identify the range of current and surface coverage corresponding to the simulations performed at $\overline{\Phi}_{\mathrm{m}} = -0.15$V ($\langle A \rangle = 0.011$ S/cm^{2}s), $\overline{\Phi}_{\mathrm{m}} = -0.1$V ($\langle A \rangle = 0$ S/cm^{2}s), and $\overline{\Phi}_{\mathrm{m}} = 0.1$V ($\langle A \rangle = -0.83$ S/cm^{2}s). The position $r = 0$ corresponds to the lower-left corner of each box.

4-5B, and 4-5C, respectively. The solid lines in Figure 4-5 represent the simulation results by solving the Laplace's equation coupling the boundary conditions that account for the time-constant dispersion associated with the electrode geometry. The dashed curves represent the global impedances calculated by use of a mathematical expression

$$Z = R_{\mathrm{e}} + \frac{1}{1/Z_{\mathrm{F}} + j\omega C_0} \tag{4–34}$$

associated with the Ohmic resistance in solution and a combination of Faradaic reaction and electric double layer at electrode. The Ohmic resistance developed by Newman[5] is given in equation (4–32). The Faradaic impedance is calculated from equation (4–14) in terms of the surface-average parameters given from equation (4–15) to (4–17) and therefore did not account for the influence of electrode geometry. The geometry of the disk electrode is shown to distort the global impedance response. The geometry-induced distortion of impedance response and corresponding depressions of semicircles at high and low frequencies are more obvious in Figure 4-5C where $\langle A \rangle < 0$.

The charge-transfer resistance R_{t} for the coupled reactions can be evaluated from the diameter of the high-frequency loop of the global impedance, and the low-frequency loop yields the resistance R_{γ} associated with the concentration of adsorbed species. A comparison between the effective kinetic parameters $R_{\mathrm{t,eff}}$ and $R_{\gamma,\mathrm{eff}}$, which account for electrode geometry, to the respective values that assume an uniform electrode is presented in Figure 4-6 as a function of $\langle J \rangle$. The relationship between $\langle J \rangle$ and the electrode potential $\overline{\Phi}_{\mathrm{m}}$ is given in Figure 4-3D. The ratios $R_{\mathrm{t,eff}}/R_{\mathrm{t}}$ and $R_{\gamma,\mathrm{eff}}/R_{\gamma}$ approach unity as $\langle J \rangle \to 0$. The value of $R_{\mathrm{t,eff}}/R_{\mathrm{t}}$ increases when $\langle J \rangle$ increases, which is in agreement with the result presented by Huang *et al.*[12] that the influence of time-constant dispersion is greater when $\langle J \rangle$ is large. The value of $R_{\gamma,\mathrm{eff}}/R_{\gamma}$ is largest for $\langle J \rangle$ close to 3.09 where $\langle A \rangle = 0$. The surface coverage by the reaction intermediate has the greatest nonuniformity at $\langle A \rangle = 0$, as shown in Figure 4-3A and 4-3B, and hence a significant error in $R_{\gamma,\mathrm{eff}}$ is seen when $\langle A \rangle$ approaches zero.

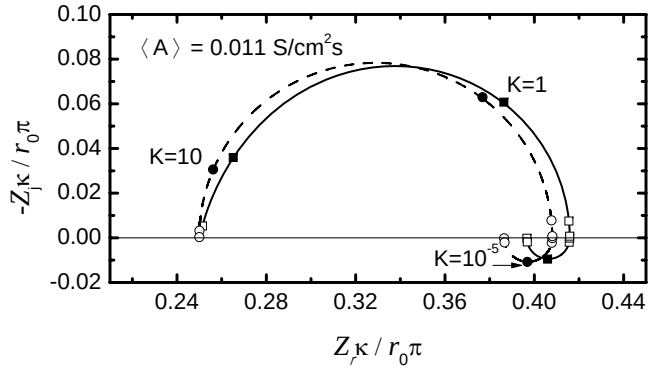

A

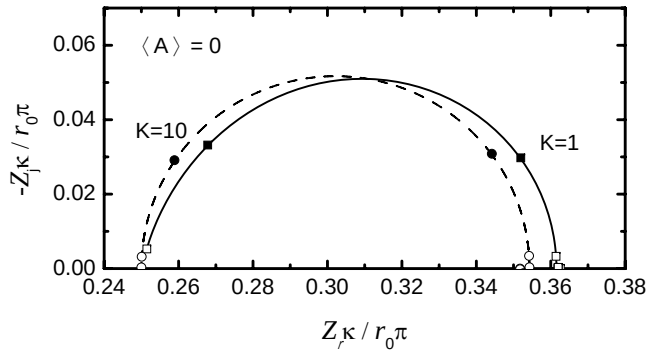

B

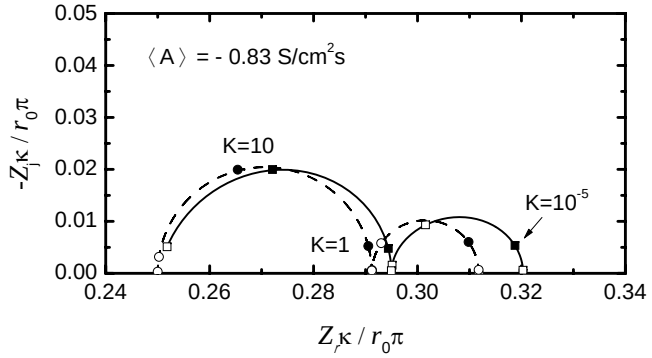

C

Figure 4-5. Calculated Nyquist representation of the global impedance response for a disk electrode considering the influence of electrode geometry (solid lines) and in the absence of geometry effect (dashed lines): A) $\langle A \rangle > 0$ (0.011 S/cm^{2}s); B) $\langle A \rangle = 0$; and C) $\langle A \rangle < 0$ (-0.83 S/cm^{2}s).

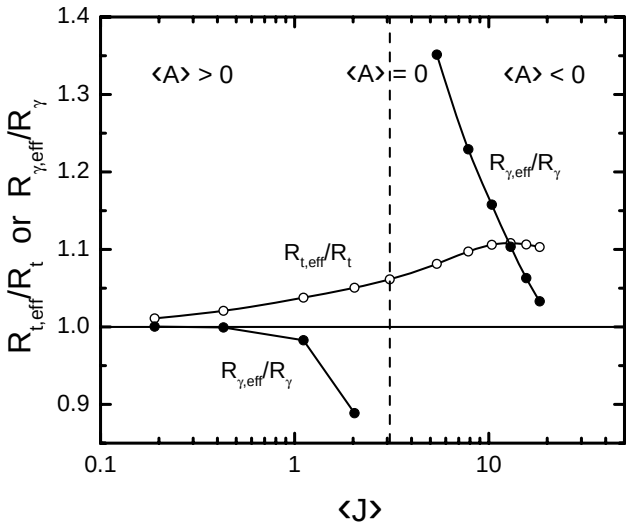

Figure 4-6. The value of $R_{\mathrm{t,eff}}/R_{\mathrm{t}}$ and $R_{\gamma,\mathrm{eff}}/R_{\gamma}$ evaluated from the global impedance as a function of $\langle J \rangle$.

The results for global impedance can be understood through the examination of the local impedance distributions. In the following sections, the calculated results for local, local interfacial and local Ohmic impedance are presented and compared for three different potentiostatic conditions: $\overline{\Phi}_{\mathrm{m}} = -0.15$ V ($\langle A \rangle = 0.011$ S/cm^{2}s), $\overline{\Phi}_{\mathrm{m}} = -0.1$ V ($\langle A \rangle = 0$ S/cm^{2}s), and $\overline{\Phi}_{\mathrm{m}} = 0.1$ V ($\langle A \rangle = -0.83$ S/cm^{2}s).

4.2.2 Local Interfacial Impedance

Nyquist plots for the calculated local interfacial impedance are presented in Figures 4-7A, 4-7B, and 4-7C for $\langle A \rangle > 0$, $\langle A \rangle = 0$, and $\langle A \rangle > 0$, respectively, with normalized radial position r/r_0 as a parameter. The impedance diagrams are superposed at high frequencies, showing that current flows mainly through the double-layer capacitance which was assumed to be uniform at the electrode surface. The shape of the low-frequency Faradaic loop is dependent on the sign of parameter $\langle A \rangle$. The local interfacial impedance has a low-frequency inductive loop at all positions on the electrode when $\langle A \rangle > 0$, and shows low-frequency capacitive features when $\langle A \rangle < 0$. For $\langle A \rangle = 0$, although only a single capacitive loop is observed in the global impedance (Figure

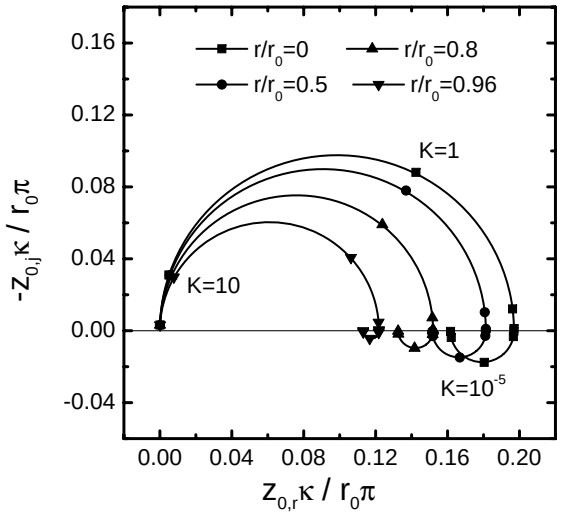

A

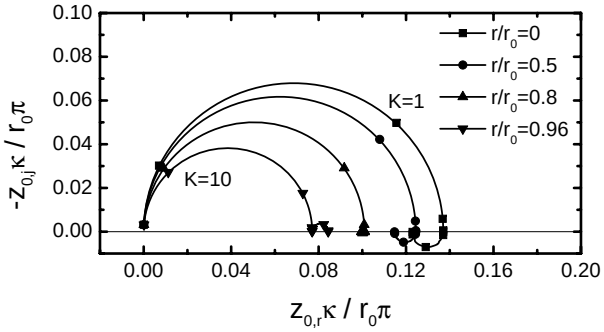

B

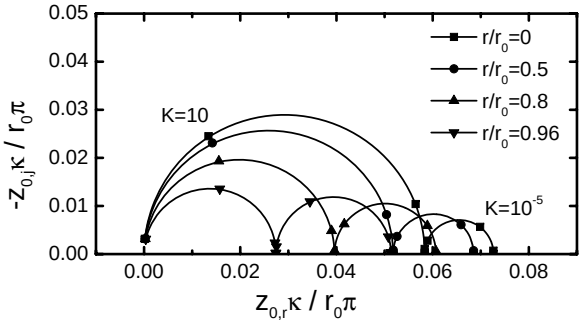

C

Figure 4-7. Calculated Nyquist representation of the local interfacial impedance response of a disk electrode with normalized radial position r/r_0 as a parameter: A) $\langle A \rangle > 0$ (0.011 S/cm^{2}s); B) $\langle A \rangle = 0$; and c) $\langle A \rangle < 0$ (-0.83 S/cm^{2}s).

4-5B), two time constants are seen in the local interfacial impedance. At the periphery of the electrode, a low-frequency capacitive loop is seen, representing a local positive value of A. Near the electrode center, a low-frequency inductive loop is observed, indicating the local negative value of A. The different low-frequency features seen at different radial positions demonstrates that the global impedance is an average representation of the electrode surface.

For the three potentiostatic conditions, the values of the local interfacial impedance are larger at the electrode center and smaller at the periphery, indicating a greater accessibility near the edges of the electrode. The applied electrode potential is the largest in the case $\langle A \rangle < 0$, driving larger current densities through the electrode-electrolyte interface, thus the interfacial impedance has the smallest value when $\langle A \rangle$ is negative.

4.2.3 Local Ohmic Impedance

The calculated local Ohmic impedances for $\langle A \rangle > 0$, $\langle A \rangle = 0$, and $\langle A \rangle < 0$ in Nyquist format are shown in Figures 4-8A, 4-8B, and 4-8C, respectively, with normalized radial position as a parameter. As discussed by Huang *et al.* ,[10–12] the resistance in the electrolyte is not a pure resistance, but acts as an impedance with complex features. The high-frequency loops at $K > 10^{-2}$ are in agreement with the previous studies for a blocking electrode and a disk electrode subject to a single Faradaic reaction, in which the geometry-induced current and potential distributions are observed.[12] In the present case, however, low-frequency loops can also be observed. The size of these low-frequency loops increases with applied potential, *i.e.,* for $\langle A \rangle < 0$.

The dependence of the local Ohmic impedance with frequency is shown more clearly in the representation of the real and imaginary components as given in Figure 4-9. For the real component, the values at high-frequency limit are independent of $\langle A \rangle$; whereas, at the low-frequency limit, the difference of real values between the electrode center and the periphery is larger for $\langle A \rangle < 0$. The nonzero values in the imaginary

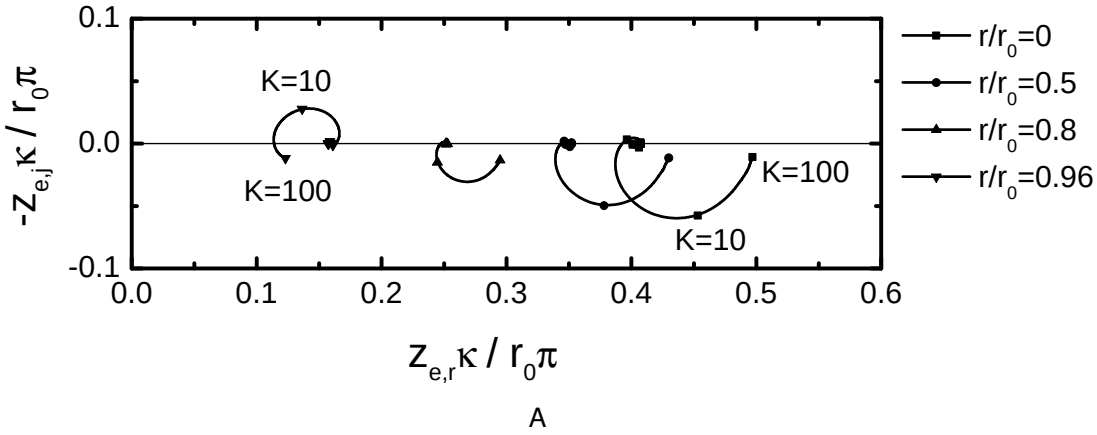

A

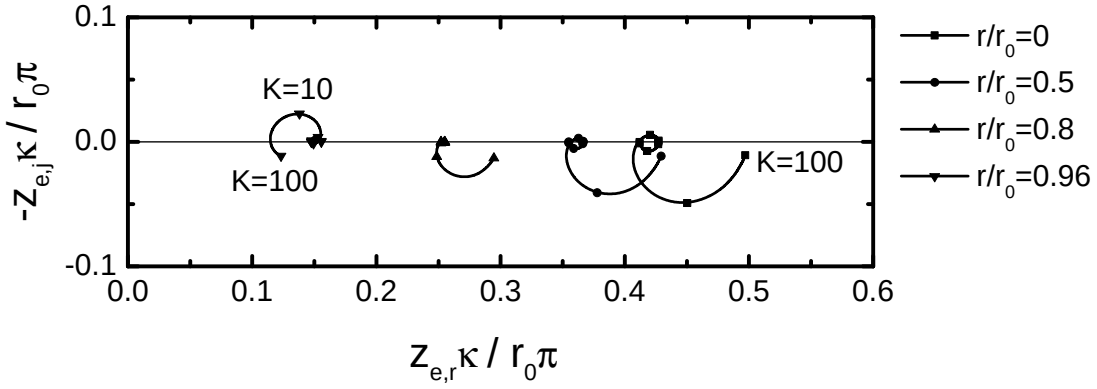

B

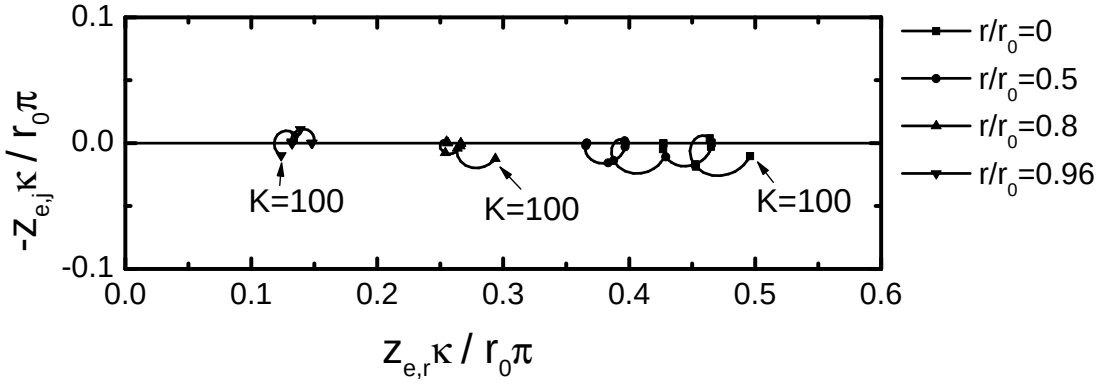

C

Figure 4-8. Calculated Nyquist representation of the local Ohmic impedance response of a disk electrode with normalized radial position r/r_0 as a parameter: A) $\langle A \rangle > 0$ (0.011 S/cm^{2}s); B) $\langle A \rangle = 0$; and C) $\langle A \rangle < 0$ (-0.83 S/cm^{2}s).

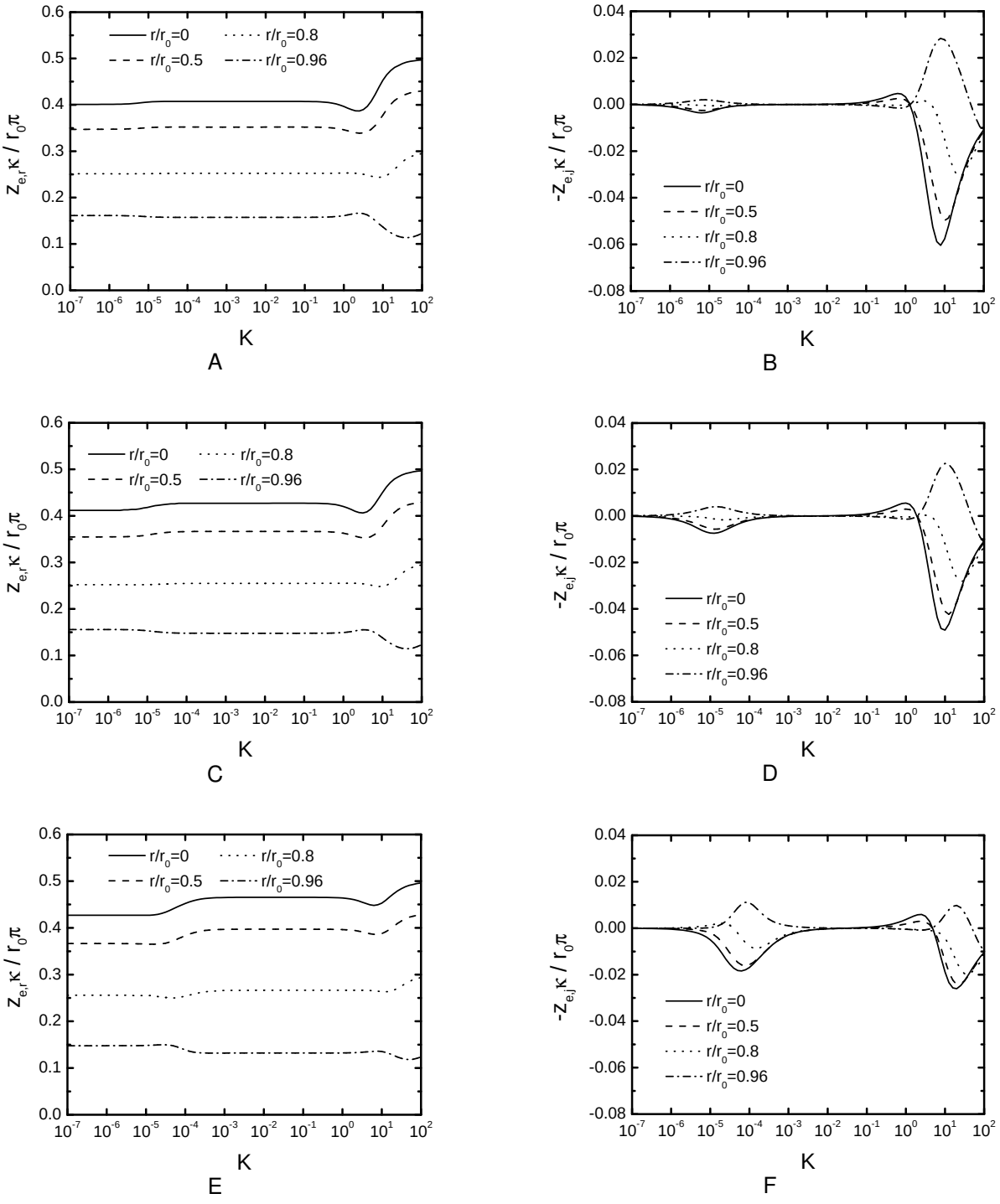

Figure 4-9. Calculated real and imaginary parts of the local Ohmic impedance response of a disk electrode as a function of dimensionless frequency K: A) real part for $\langle A \rangle = 0.011$ S/cm^{2}s; B) imaginary part for $\langle A \rangle = 0.011$ S/cm^{2}s; C) real part for $\langle A \rangle = 0$; D) imaginary part for $\langle A \rangle = 0$; E) real part for $\langle A \rangle = -0.83$ S/cm^{2}s; and F) imaginary part for $\langle A \rangle = -0.83$ S/cm^{2}s.

component of the impedance at $10^{-7} < K < 10^{-2}$ indicate the complex behavior at low frequencies which does not appear in the system of a single Faradic reaction without adsorbed reaction intermediates. Complex features are more significant at low frequencies and less significant at high frequencies when the applied potential to the electrode increases, but the ranges of dimensionless frequency where the complex Ohmic impedance are observed ($10^{-7} < K < 10^{-2}$ and $10^{-2} < K < 10^{2}$) are the same for all values of $\langle A \rangle$.

According to the expression for the dimensionless frequency K in equation (8–17), the frequency that applies in the impedance measurement is given by

$$f = \frac{1}{2\pi} \frac{K\kappa}{r_0 C_0} \tag{4–35}$$

For an electrochemical system with conductivity $\kappa = 0.01$ S/cm (corresponding to a 0.1 M NaCl solution) and a double-layer capacitance $C_0 = 10$ μF/cm^2 at a disk electrode with radius $r_0 = 0.1$ cm, the frequency range corresponding to the calculated dimensionless values $10^{-7} < K < 10^{-2}$ is 0.16 mHz $< f < 16$ Hz, which is well within the range of typical experimental measurements.

4.2.4 Local Impedance

The calculated local impedance is shown in Nyquist format in Figure 4-10 with radial position as a parameter. The local impedance shows distortion from the ideal semicircle appearing in the local interfacial impedance. A high-frequency inductive loop is observed at all radial positions, and, in addition, capacitive or inductive loops are observed at low frequencies. As it represents a summation of the local interfacial and local Ohmic impedances, the high-frequency inductive behavior in the local impedance plot must be seen as well in the local Ohmic impedance. The features at lower frequencies are strongly dependent on the radial position.

The changes in sign of the imaginary part of the the local impedance are evident in Figure 4-11, where the absolute value of the imaginary part of the local impedance

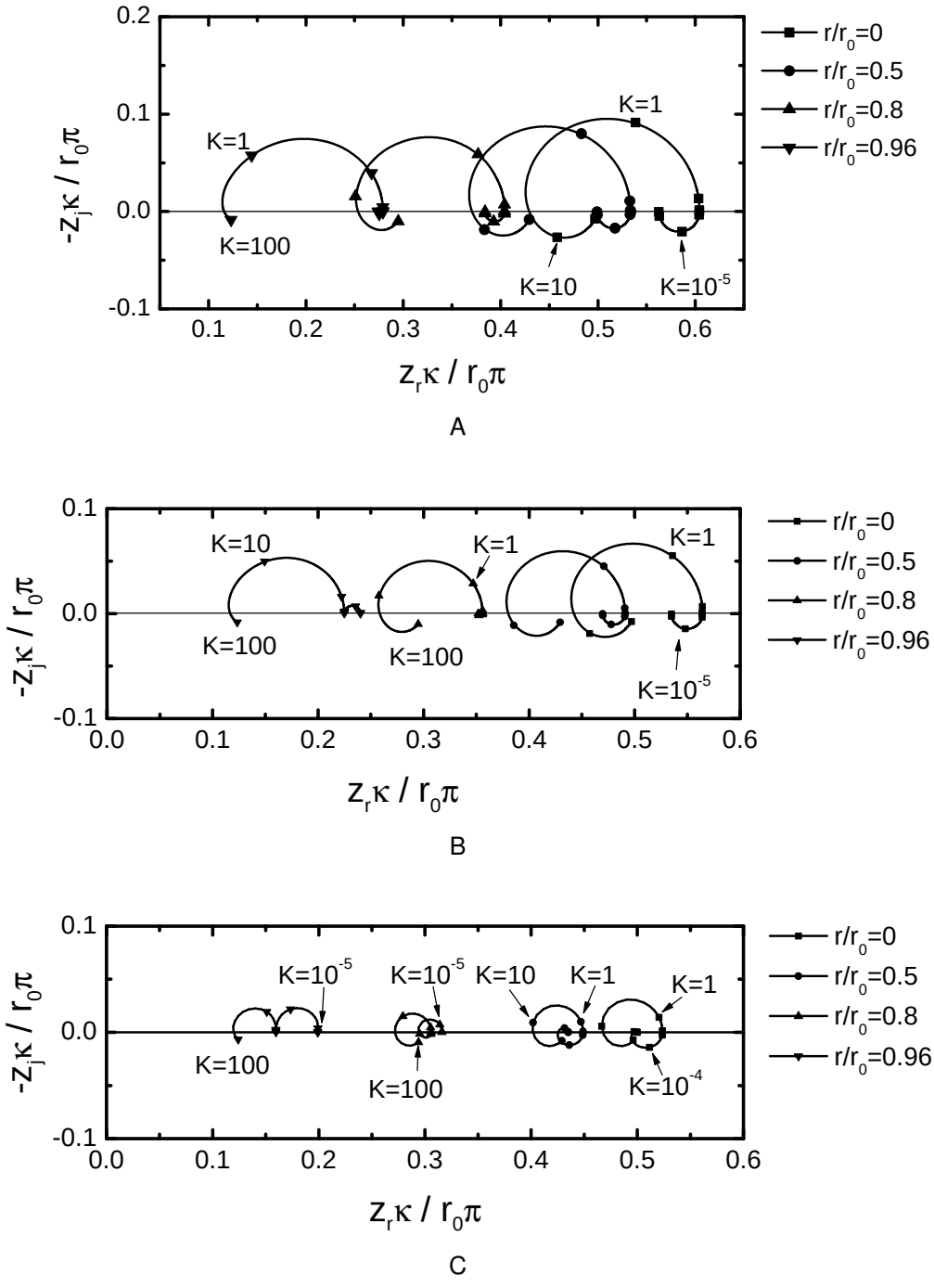

Figure 4-10. Calculated Nyquist representation of the local impedance response of a disk electrode with normalized radial position r/r_0 as a parameter: A) $\langle A \rangle > 0$ (0.011 S/cm^{2}s); B) $\langle A \rangle = 0$; and C) $\langle A \rangle < 0$ (-0.83 S/cm^{2}s).

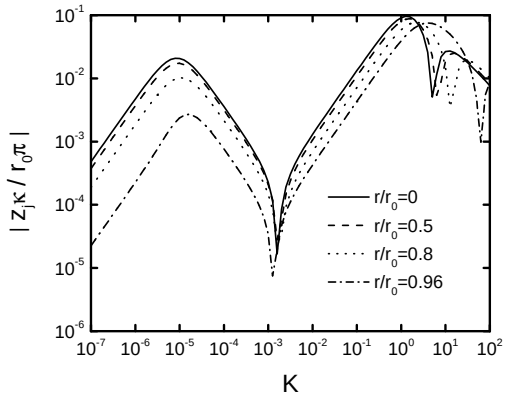

A

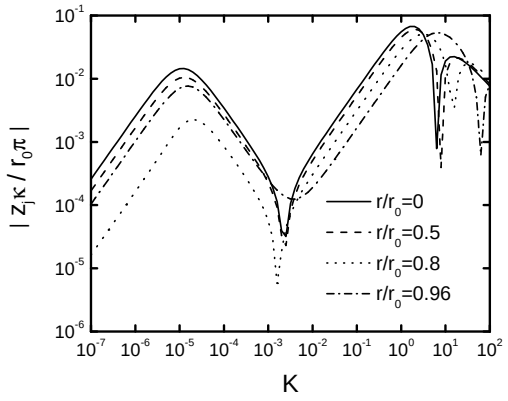

B

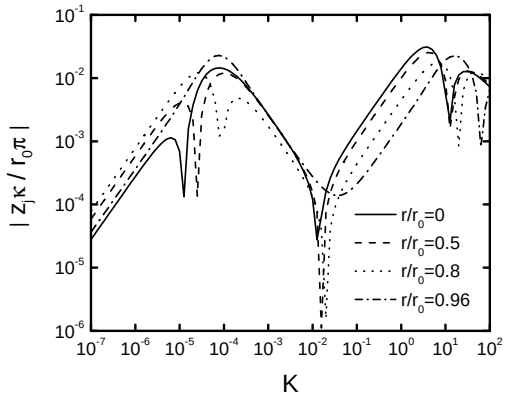

C

Figure 4-11. Calculated representation of the imaginary component of the local impedance response on a disk electrode as a function of dimensionless frequency K: A) $\langle A \rangle > 0$ (0.011 S/cm^{2}s); B) $\langle A \rangle = 0$; and C) $\langle A \rangle < 0$ (-0.83 S/cm^{2}s).

is presented as a function of the dimensionless frequency K. Changes in sign are evident in the frequency range $1 < K < 100$, which accounts for the appearance of the high-frequency inductive loop in the Nyquist plot. This result is consistent with the results obtained by Huang *et al.*[12] for a single Faradaic reaction on a disk electrode. A second change in sign is observed at frequencies near $10^{-2} < K < 10^{-3}$, which can be attributed to the role of the adsorbed intermediate. For the case $\langle A \rangle < 0$, yet another crossover is observed at even lower frequencies ($10^{-4} < K < 10^{-6}$). This effect is seen because the complex behavior of the local Ohmic impedance is more significant when a higher electrode potential is applied, driving more current.

4.3 Validation of Calculations

The potential distribution was solved numerically by use of the finite-element method. The calculation was verified by refining the mesh until the solution reached a stable value. The number of elements generated at the electrode boundary was 200, and the total number of elements in the domain was about 32,000. For dimensionless frequencies $K < 100$, the differences between solution potential adjacent to the electrode with different mesh densities were less than 0.001 percent. The calculated current flux for different mesh densities had differences less than 0.5 percent, and the calculated local impedances had differences less than 0.6 percent.

The numerical method was also applied to solve the system with a single Faradaic reaction in order to compare to the results obtained by Huang *et al.* ,[12] who used a collocation method. At $K < 100$, the differences between calculated local impedance obtained from the two numerical methods were less than 0.5 percent.

The role of electrode geometry in creating the low-frequency dispersion reported here was also verified by examining the impedance response of a recessed electrode. Frateur *et al.*[14] have demonstrated that a uniform primary distribution can be achieved by use of a recessed electrode with the depth twice the electrode radius($P = p/r_0 = 2$). The impedance response presented in Figure 4-12 was obtained for a recessed

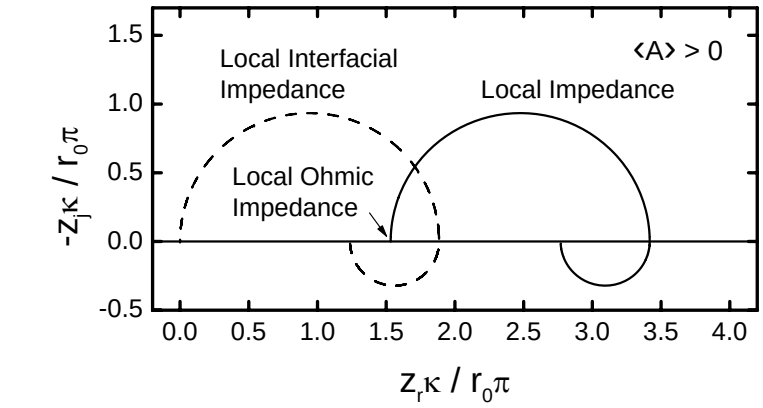

A

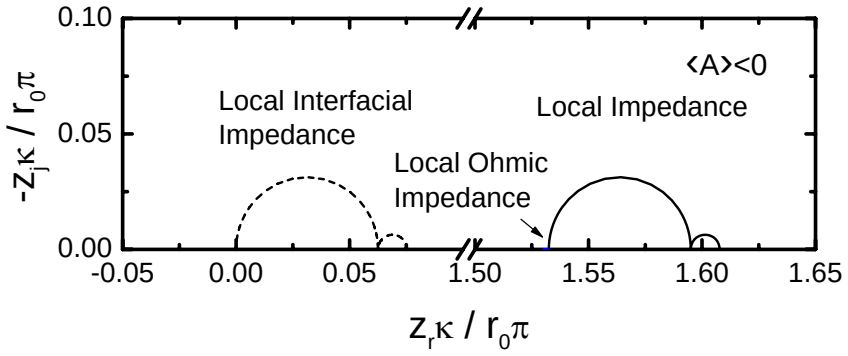

B

Figure 4-12. The impedance response for a recessed electrode: A) $\langle A \rangle > 0$; and B) $\langle A \rangle < 0$.

electrode with $P = 4$. The local impedance response at different radial positions shows no dispersion along the electrode surface. In addition, ideal features were observed in the global impedance plots. The elimination of the geometry effect by use of a recessed electrode demonstrates that the complex behavior for the local Ohmic impedance at both low and high frequencies can not be attributed to calculation artifacts.

4.4 Evaluation of CPE Exponent

Geometry-induced current and potential distributions were shown to have influence on the impedance response only at dimensionless frequency $K > 1$ for a blocking electrode[6,10] and a disk electrode subject to a single Faradaic reaction.[11,12] The results of the present work showed that, for a more complicated system with reactions associated with an adsorbed intermediate, the impedance response is affected by the geometry of the disk electrode at low frequencies as well as at high frequencies.

The concept that the non-ideal impedance caused by geometry-induced current and potential distributions could be expressed in terms of CPE behavior at high frequencies has been discussed by Huang *et al.*[11,12] The parameter α in the CPE expression was obtained in their work from the slope of the magnitude of the imaginary part of the global impedance plotted as a function of frequency in logarithmic scales. This approach worked well for the high-frequency behavior. In the present study, however, the slope for the low-frequency inductive or capacitive loops could not be clearly resolved because the range of frequency was too short. The impedance data within this frequency range was influenced by the high-frequency loop which obscured the slope.

Another approach for graphical quantification for CPE behavior can be developed by exploring how the shape of a single impedance loop deviates from that of a perfect semicircle. The maximum magnitude of the imaginary part of impedance ΔZ_j and the difference between high and low-frequency asymptotes for the of real part of the impedance ΔZ_r shown in Figure 4-13 for a single loop correspond to the radius and the diameter for a semicircle, respectively. The absolute ratio of ΔZ_j and ΔZ_r is related to

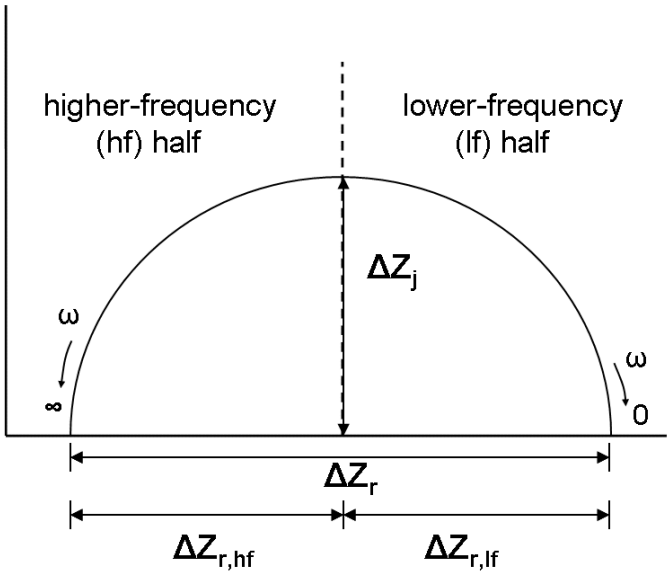

Figure 4-13. A graphical representation of a single impedance loop separated into a higher-frequency (hf) half and a lower-frequency (lf) half.

the CPE parameter α by

$$\left|\frac{\Delta Z_j}{\Delta Z_r}\right| = \frac{1}{2}\tan(\frac{\alpha\pi}{4}) \tag{4–36}$$

If $\alpha = 1$, $|\Delta Z_j/\Delta Z_r| = 0.5$, which represents a perfect semicircle in the impedance plane. If an electrode exhibits a local CPE behavior, the value of $|\Delta Z_j/\Delta Z_r|$ is less than 0.5 and a depressed semicircle in the impedance plot is observed. The distortion of the impedance response can be found by dividing the impedance loop into a higher-frequency half and a lower-frequency half as shown in Figure 4-13. The dependence of $|\Delta Z_j/\Delta Z_{r,\mathrm{hf}}|$ and $|\Delta Z_j/\Delta Z_{r,\mathrm{lf}}|$ to the parameter α can be found from equation (4–36) to be

$$\left|\frac{\Delta Z_j}{\Delta Z_{r,\mathrm{hf}}}\right| \quad \text{or} \quad \left|\frac{\Delta Z_j}{\Delta Z_{r,\mathrm{lf}}}\right| = \tan(\frac{\alpha\pi}{4}) \tag{4–37}$$

If the values of the two ratios are different, the impedance loop is not symmetric and does not correspond to a true CPE for which α must be constant.

The shape of the global impedance loops can be observed in Figure 4-5. The calculated values of α from equations (4–36) and (4–37) for the impedance loops are presented in Table 4-2. For the three potentiostatic conditions, $\overline{\Phi}_{\mathrm{m}} = -0.15$ V

Table 4-2. Values of CPE exponent α calculated using equations (4–36) and (4–37) for the high-frequency and low-frequency impedance loops in Figure 4-5.

	Higher-frequency half	Lower-frequency half	Average
$\langle A \rangle > 0$ (0.011 S/cm^{2}s)			
High-frequency loop	0.928	0.995	0.960
Low-frequency loop	0.998	0.997	0.997
$\langle A \rangle = 0$ S/cm^{2}s			
High-frequency loop	0.919	0.991	0.954
$\langle A \rangle < 0$ (-0.83 S/cm^{2}s)			
High-frequency loop	0.905	0.975	0.939
Low-frequency loop	0.881	0.926	0.903

($\langle A \rangle = 0.011$ S/cm^{2}s), $\overline{\Phi}_{\mathrm{m}} = -0.1$ V ($\langle A \rangle = 0$ S/cm^{2}s), and $\overline{\Phi}_{\mathrm{m}} = 0.1$ V ($\langle A \rangle = -0.83$ S/cm^{2}s), all high-frequency loops show depressed semicircles and the corresponding α values are smaller than unity. In contrast to the results given by Huang *et al.*[12] for a single Faradaic reaction, the lower-frequency half shows CPE behavior instead of an ideal impedance response because the characteristic frequency of the high-frequency loop shifts to a higher value as the applied electrode potential increases and, thus, the CPE features induced by the electrode geometry can be seen in the lower-frequency half.

For the present study, the low-frequency loops for $\langle A \rangle \neq 0$ are also depressed. For $\langle A \rangle = 0$ there is no low-frequency loop observed. The deviation of α from unity becomes larger when A is negative, representing the more nonuniform current and potential distributions as $\overline{V}$ increases. The time-constant dispersion associated with the geometry of the disk electrode results in a CPE behavior at low frequency due to the relationship between the radial distribution of adsorbed intermediate and the radial distribution of interfacial potential. As described by Huang *et al.*,[12] CPE behavior is seen as well at high frequencies due to the radial distribution of interfacial potential.

The α values calculated from the global impedance response of a recessed electrode were equal to unity for both high-frequency and low-frequency loops. This

ideal behavior shows that the potential and current were uniform for the recessed electrode geometry.

The evidence of a frequency or time-constant dispersion has relevance to the use of microelectrodes to study the kinetics of fast electrochemical reactions. For simple reactions, it is sufficient to design the electrode such that the characteristic frequency that yields $K = 1$ is sufficiently larger than the characteristic frequency for the reaction. This can be achieved by making the electrode smaller. For reactions involving adsorbed intermediates, however, frequency or time-constant dispersion will be observed at low frequencies as well, thus complicating the interpretation of the experimental results.

CHAPTER 5
ELECTRODE REACTION WITH ADSORBED INTERMEDIATES: EXPERIMENTAL

The geometry-induced current and potential distributions were investigated in a Faradaic system involving an adsorbed intermediate. The dispersion of impedance response was predicted to be observed not only at high frequencies, but also at low frequencies in which the characteristic frequency for the adsorption reaction was involved. An experimental verification of the theoretical results is provided in this chapter using the iron dissolution as an example.

5.1 Dissolution of Iron

As most of the electrochemical systems do not follow the simple case of linear kinetics, the impedance model presented here is assumed to be in the Tafel regime. The system of interest is the corrosion of a pure iron electrode in 0.5 M sulfuric acid. Bockris and coworkers[52] proposed a reaction model in which two consecutive steps are coupled by an adsorbed intermediate. The anodic dissolution of iron can be described in simplified form as

$$\mathrm{Fe} \xrightarrow{K_1} \mathrm{Fe}^{+}_{\mathrm{ads}} + \mathrm{e}^{-} \tag{5–1}$$

and

$$\mathrm{Fe}^{+}_{\mathrm{ads}} \xrightarrow{K_2} \mathrm{Fe}^{2+} + \mathrm{e}^{-} \tag{5–2}$$

The iron first oxidizes and forms a monovalent intermediate adsorbed on the electrode surface. This reaction is followed by the oxidation of the intermediate. The ferrous ion is soluble and diffuses away from the electrode. For this work, the system was at a potential such that the system remained in the active dissolution domain.

Under the assumption of Tafel kinetics, the reaction rates for reactions (5–1) and (5–2) can be expressed by

$$i_1 = K_1(1-\gamma)\exp[b_1(\Phi_{\mathrm{m}} - \Phi_0)] \tag{5–3}$$

and

$$i_2 = K_2\gamma \exp[b_2(\Phi_\mathrm{m} - \Phi_0)] \tag{5–4}$$

where K_1 and K_2 are the effective rate constants, and b_1 and b_2 are the Tafel slopes for each reaction.

The variation of surface coverage is associated with the two anodic reactions by

$$\frac{\partial\gamma}{\partial t} = \frac{i_1 - i_2}{\Gamma F} \tag{5–5}$$

When the steady state is achieved, the surface coverage at steady state can be calculated from equations (5–3) and (5–4) as

$$\overline{\gamma} = \frac{K_1 \exp[b_1(\overline{\Phi}_\mathrm{m} - \overline{\Phi}_0)]}{K_1 \exp[b_1(\overline{\Phi}_\mathrm{m} - \overline{\Phi}_0)] + K_2 \exp[b_2(\overline{\Phi}_\mathrm{m} - \overline{\Phi}_0)]} \tag{5–6}$$

In contrast to the case presented in equation (4–7) for linear kinetics, equation (5–6) shows that the steady-state surface coverage is dependent on the surface overpotential under the assumption of Tafel kinetics.

The Faradaic impedance associated with the Tafel kinetics is expressed by equation (4–14) with the charge-transfer resistance

$$R_\mathrm{t} = \frac{1}{K_1(1-\overline{\gamma})b_1 \exp[b_1(\overline{\Phi}_\mathrm{m} - \overline{\Phi}_0)] + K_2\gamma b_2 \exp[b_2(\overline{\Phi}_\mathrm{m} - \overline{\Phi}_0)]} \tag{5–7}$$

and the parameters A and B are given by

$$\begin{aligned} A = \{&K_2\gamma b_2 \exp[b_2(\overline{\Phi}_\mathrm{m} - \overline{\Phi}_0)] \\ &- K_1(1-\overline{\gamma})b_1 \exp[b_1(\overline{\Phi}_\mathrm{m} - \overline{\Phi}_0)]\} \frac{K_1 \exp[b_1(\overline{\Phi}_\mathrm{m} - \overline{\Phi}_0)] - K_2 \exp[b_2(\overline{\Phi}_\mathrm{m} - \overline{\Phi}_0)]}{\Gamma F} \end{aligned} \tag{5–8}$$

and

$$B = \frac{K_1 \exp[b_1(\overline{\Phi}_\mathrm{m} - \overline{\Phi}_0)] + K_2 \exp[b_2(\overline{\Phi}_\mathrm{m} - \overline{\Phi}_0)]}{\Gamma F} \tag{5–9}$$

respectively. According to the values of the kinetic parameters, A can be positive or negative, but B is always positive. Substitution of equation (5–6) into equations (5–3)

and (5–4) yields the steady-state polarization curve expressed as

$$\bar{i} = \frac{2K_1 \exp[b_1(\overline{\Phi}_m - \overline{\Phi}_0)]K_2 \exp[b_2(\overline{\Phi}_m - \overline{\Phi}_0)]}{K_1 \exp[b_1(\overline{\Phi}_m - \overline{\Phi}_0)] + K_2 \exp[b_2(\overline{\Phi}_m - \overline{\Phi}_0)]} \tag{5–10}$$

The Faradaic impedance was then calculated from equation (4–14).

In the case of linear kinetics developed Section 4.1.1, it is easy to verify that $A = 0$. The Faradaic impedance is only a charge-transfer resistance which is in agreement with equation (4–14).

The dispersion of local impedances was discussed in Chapter 4 for electrochemical reactions involving one adsorbed intermediate. While the global impedance at a given potentiostatic condition may have a specific low-frequency feature, *e.g.,* capacitive or inductive, the local impedances show a variation of low-frequency features along the electrode surface, which results from the distribution of potential and corresponds to different values of the local parameters A and B. The global impedance could be considered to provide an average representation of the electrode surface, and the low-frequency feature is determined by the surface average values of $\langle A \rangle$ and $\langle B \rangle$. As the polarization condition changes along the current-voltage (I-V) curve, the low-frequency loop in the global impedance diagram could change from inductive to capacitive, and vice versa.

5.2 Experimental Setup

The disk electrode used in the experiment was a 0.5 cm diameter pure iron electrode embedded in an insulating epoxy resin. The electrolyte solution was a 0.5 M H_2SO_4 solution prepared with distilled water.

The experimental measurements of LEIS were performed with a bielectrode that consisted of two platinum wires sealed in a borosilicate bicapillary. The configuration and preparation of the bielectrode were described in earlier papers.[2,14] The use of a four-channel frequency response analyzer allowed the global, local, and local-interfacial impedances to be measured simultaneously. All impedance measurements were

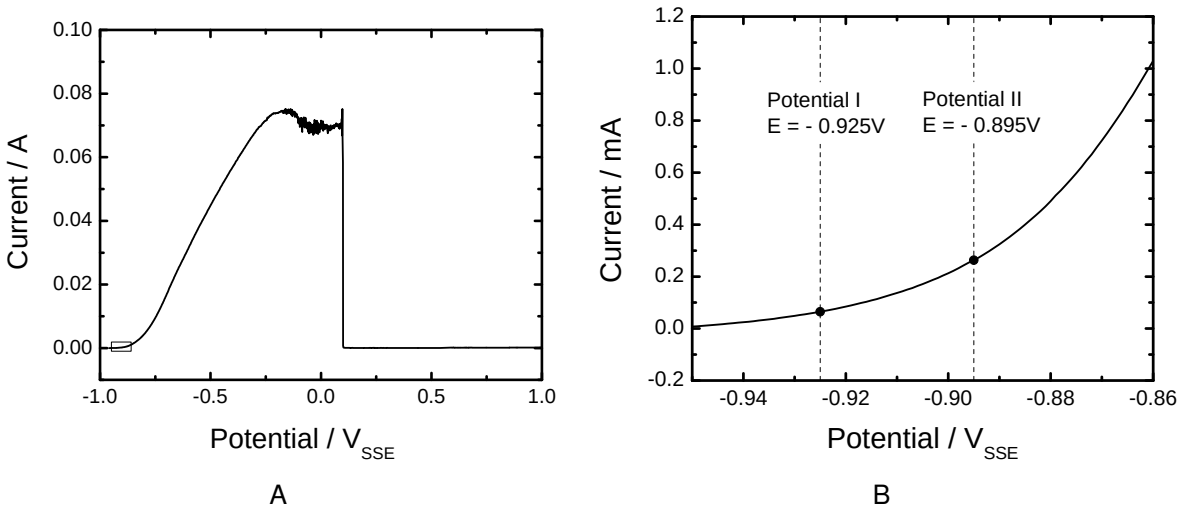

Figure 5-1. The polarization curve for a stationary iron electrode in 0.5 M H_2SO_4: A) a scan including both the active and passivated regions; B) zoomed portion of the box in part (A) showing the potential at which the impedance measurements were performed.

performed at room temperature (about 19°C). The potential applied to the iron electrode was selected to achieve the active dissolution of iron on the polarization curve.

The impedance measurement was performed using a 50 mV peak-to-peak sinusoidal perturbation, a frequency range of 65,000 Hz to 0.1 Hz, and seven points per decade of frequency. The 50 mV perturbation amplitude was selected to maximize the signal-to-noise ratio while maintaining linearity.[53,54] The linear response was confirmed by measuring the impedance using different amplitudes and determining the maximum amplitude that did not change the impedance response. The definitions for all the local impedances were presented by Huang *et al.*[10] theoretically and by Frateur *et al.*[2] in an experimental perspective. The same notation will be used through out the following results and discussion.

5.3 Experimental Results

The current-potential curve obtained on a stationary iron electrode in 0.5 M sulfuric acid solution is presented in Figure 5-1A. The scan rate was 2 mV/sec. The potential was applied to the iron electrode from the open-circuit potential, activating the iron

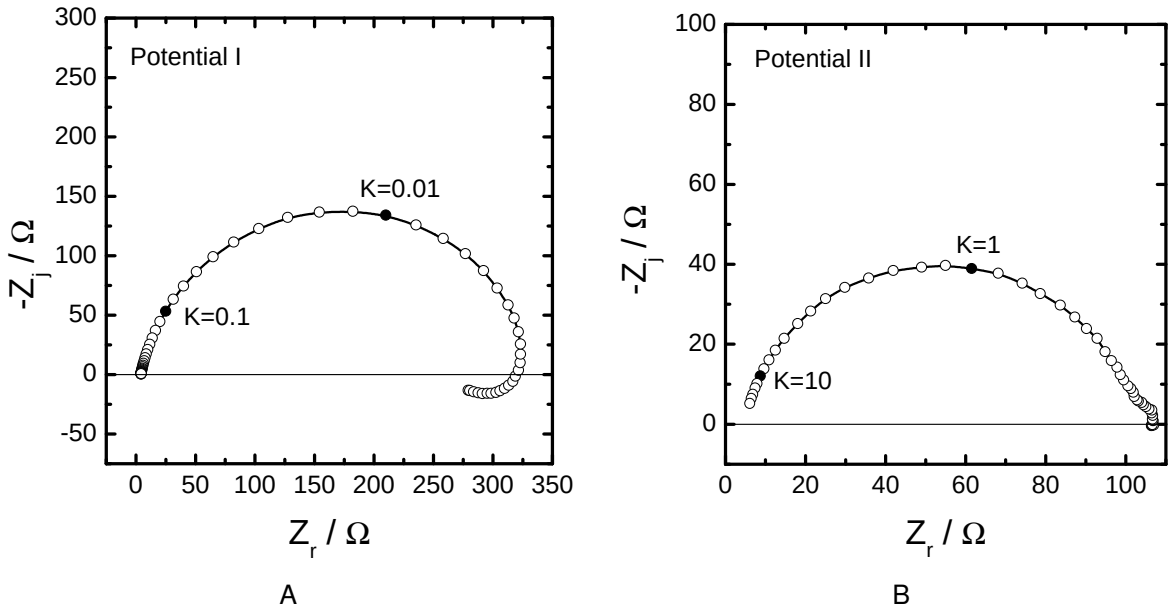

Figure 5-2. Global electrochemical response for a pure iron electrode in 0.5 M H_2SO_4: A) global impedance response measured at potential I as indicated in Figure 5-1B; and B) global impedance response measured at potential II.

electrode, to a higher potential, passivating the electrode surface. The potentials I and II in Figure 5-1B represent the two steady-state conditions for which the impedance measurements were performed. The global impedance responses given in Figure 5-2A and 5-2B show low-frequency loops which are associated with the formation of Fe(I) species adsorbed on the electrode surface, and correspond to different values of surface-average value $\langle A \rangle$. To facilitate the comparison of results, all frequencies were made dimensionless according to

$$K = \frac{\omega C_0 r_0}{\kappa} = 4\omega C_0 r_0^2 R_e \tag{5–11}$$

where r_0 is the electrode radius, C_0 is the double-layer capacitance, which was assumed to be uniform, κ is the electrolyte conductivity, and R_e is the electrolyte resistance. The parameters C_0 and R_e were determined from the global impedance measurements. The electrolyte resistance R_e was evaluated from the limiting value of the real part of the impedance in the high-frequency range; whereas, C_0 can be easily determined from

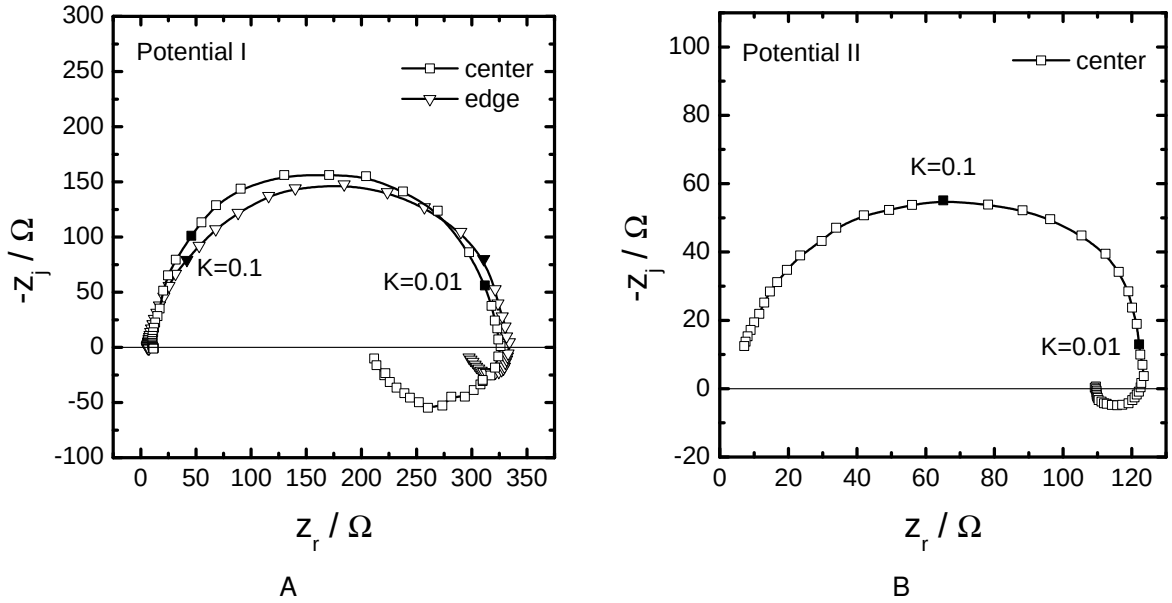

Figure 5-3. Experimental local impedance for a pure iron electrode in 0.5 M H_2SO_4 measured at A) potential I; and B) potential II in Figure 5-1B.

the characteristic frequency of the first RC time constant, which represents the high-frequency capacitive loop corresponding to R_t in parallel with C_0. When the electrode potential increases, the feature of the impedance diagram at low frequencies changes from an inductive to a capacitive behavior, implying that $\langle A \rangle$ changes sign.

The experimental local impedance diagrams obtained with a bielectrode located at different positions on the disk electrode are depicted in Figure 5-3. When measurements were performed at the polarization point I, the variations of the local impedance show different reactivity as a function of the probe location over the iron electrode. Such a behavior is attributed to the geometry-induced current and potential distributions.[10–12] In Figure 5-3A, the low-frequency inductive loop is larger at center of the electrode and smaller at the periphery, which is in agreement with a previous study[3] and indicates a greater accessibility and more reactive domain near the edges of the electrode. In Figure 5-3B, only the local impedance at the center of the disk is presented. The measurement is difficult to perform at a more anodic potential (*i.e.,* at potential II or for larger

potentials) because of an increase in the reaction rate leading to an increase in the rate of iron dissolution, especially at electrode edges. There may also be some accumulation of corrosion product species. At low frequencies, the local electrochemical impedance shows an inductive feature which is different from the capacitive behavior shown in the global impedance plot in Figure 5-2B, representing a locally positive value of A at the electrode center.

The contribution of the local Ohmic impedance can be calculated from the difference of the local and local-interfacial impedance measurements. For the steady-state condition I, the local Ohmic impedance is presented in Figure 5-4A with the radial position of the probe as a parameter. As already observed for blocking electrodes or for simple electron transfer reactions,[10–12] this contribution acts as an impedance with complex features and is strongly dependent on the radial position along the electrode radius. However, when an adsorbed intermediate is involved, complex behaviors are observed at low frequencies as well as at high frequencies. Expanded low-frequency regions are presented in Figures 5-4B and 5-4C for the local Ohmic impedance at the center and edge of the electrode, respectively. As discussed in Chapter 4, such a geometry effect is a typical feature at low frequencies for electrochemical system involving an adsorbed intermediate. From the representation of the imaginary parts of local Ohmic impedance as a function of the dimensionless frequency in Figure 5-5, nonzero values are observed at low frequencies, but these variations remain smaller than those observed at high frequencies.

As the electrode potential is biased to a more anodic potential, low-frequency complex features in the local Ohmic impedance become more significant as shown in Figure 5-6, which is in agreement with the previous study.[3] The characteristic frequency at low frequencies is associated with the potential dependence of the surface coverage by the adsorbed intermediate. The characteristic frequency depends on the effective rate constants and may not be the same for a different reaction system.

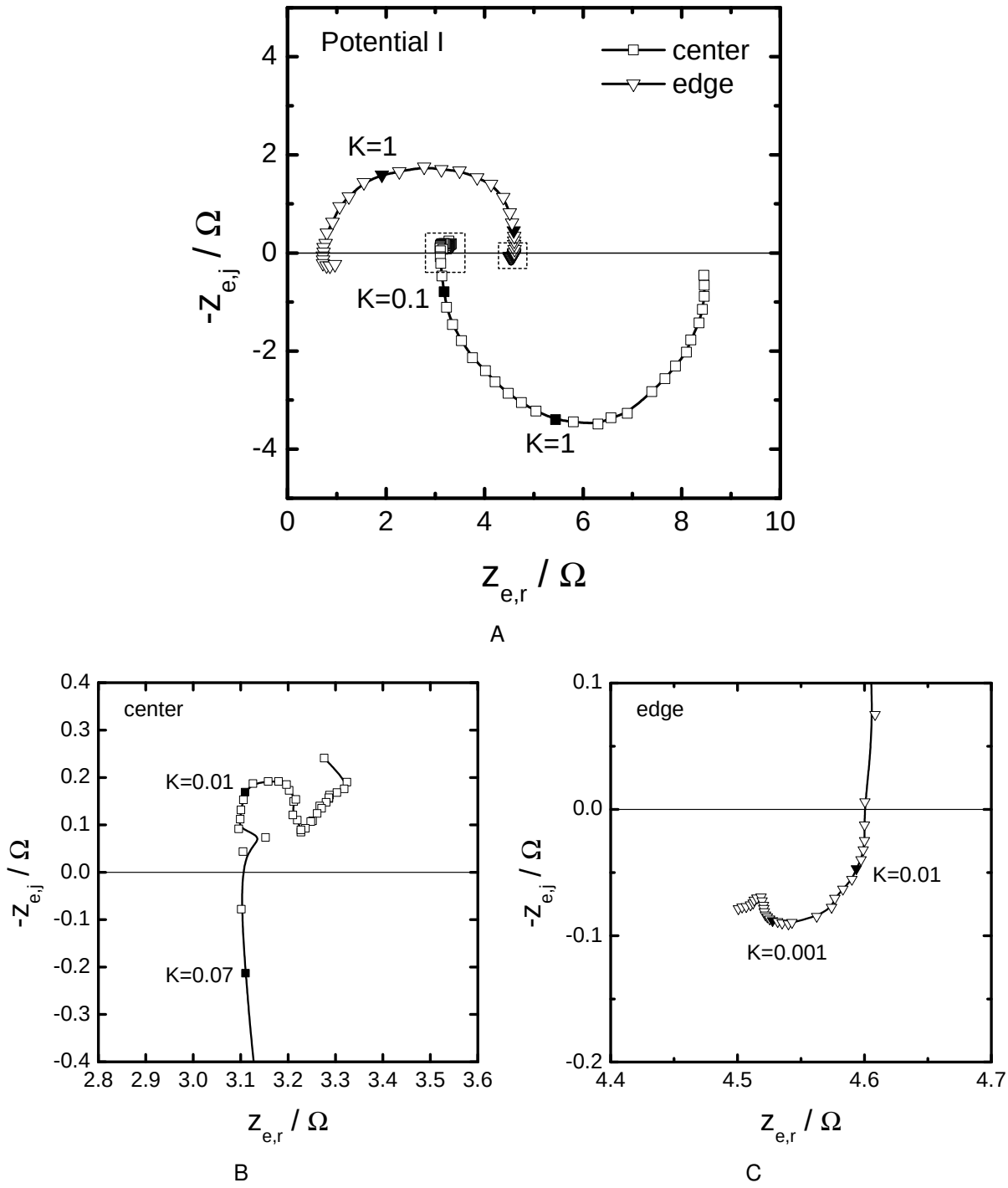

Figure 5-4. Local Ohmic impedance for a pure iron electrode in 0.5 M H_2SO_4 at potential I in Figure 5-1B. A) Local Ohmic impedance at the center and the edge of the electrode; B) the enlargement for the low-frequency end of the local Ohmic impedance at electrode center; and C) a similar enlargement for the electrode edge.

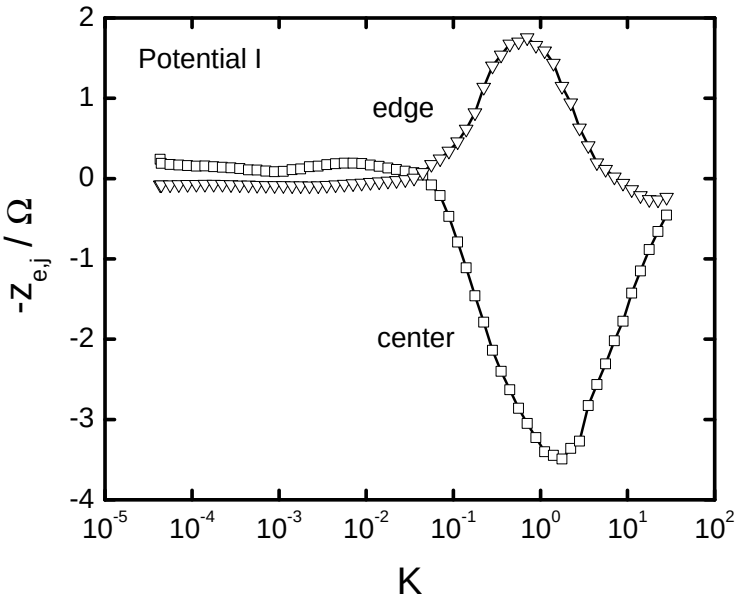

Figure 5-5. The imaginary part of the local Ohmic impedance as a function of the dimensionless frequency for a pure iron electrode in 0.5 M H_2SO_4 measured at potential I in Figure 5-1B.

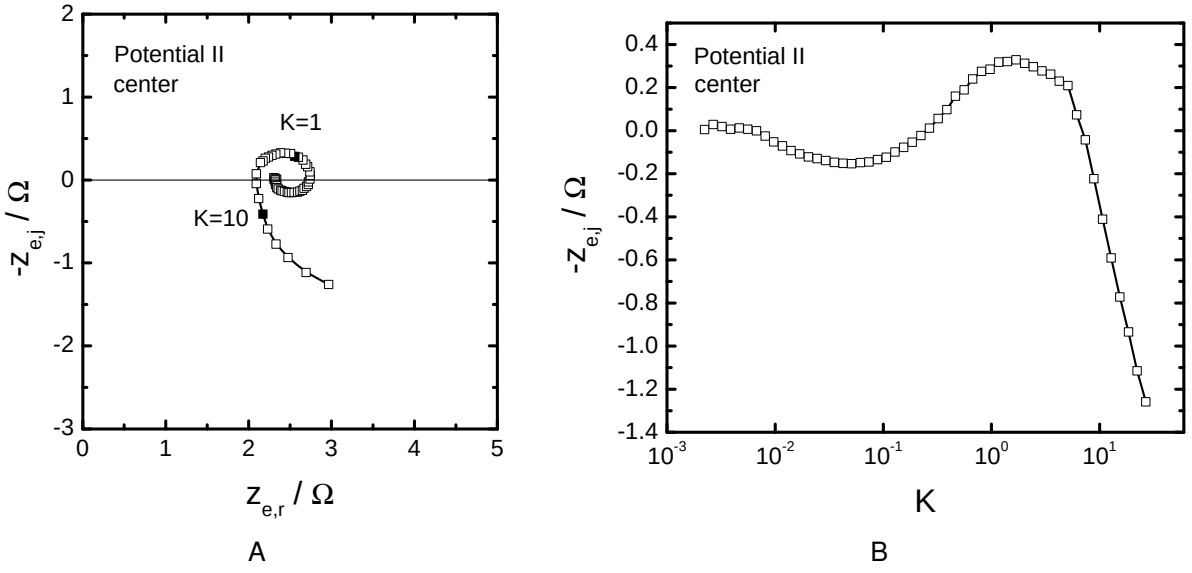

Figure 5-6. Local Ohmic impedance for a pure iron electrode in 0.5 M H_2SO_4 at potential II in Figure 5-1B. A) Nyquist plot for the local Ohmic impedances at center of the electrode; and B) imaginary part of the local Ohmic impedance as a function of dimensionless frequency.

Table 5-1. Parameters used in the simulations of iron dissolution in sulfuric acid solution.

Symbol	Meaning	Value	Units
b_1	$\alpha_1 F/RT$	38.2	V^{-1}
b_2	$\alpha_2 F/RT$	8.05	V^{-1}
K_1	effective rate constant for reaction (5–1)	3×10^{13}	A/cm^2
K_2	effective rate constant for reaction (5–2)	30	A/cm^2
C_0	double-layer capacitance	55	μF/cm^2
κ	electrolyte conductivity	0.2	S/cm
Γ	maximum surface coverage by intermediate	1×10^{-8}	mole/cm^2

5.4 Simulation Results

The mathematical development for the calculation of impedance was described by in Chapter 4. At the electrode surface, the potential perturbation was coupled by the current associated with the charging of the electrical double layer and the Faradic reactions. The potential in the bulk solution satisfies Laplace's equation and was solved in cylindrical coordinates.

The experimental polarization curve was first fitted by equation (5–10) allowing the determination of the kinetic parameters K_1, K_2, b_1, and b_2. The LEIS results were strongly dependent on these parameters. Then, the kinetic variables were varied to obtain simulations in agreement with both the polarization curve and the global impedances at the two steady-state conditions. The values of kinetic variables and other parameters used in the simulations are given in Table 5-1. It should be mentioned that the sole purpose of the comparison of experiment and simulations is to verify the prediction made in Chapter 4 that the Ohmic impedance for systems involving adsorbed intermediates may have complex characters at both low and high frequencies. As will be described in the Discussion section, this work was not intended to determine the kinetic constants for the reaction system. Thus, calculated results presented in this section can be used to show a qualitative comparison with the experimental data. The experimental curves can potentially be fitted by other sets of kinetic parameters. The parameters presented in Table 5-1 are in agreement with those presented by

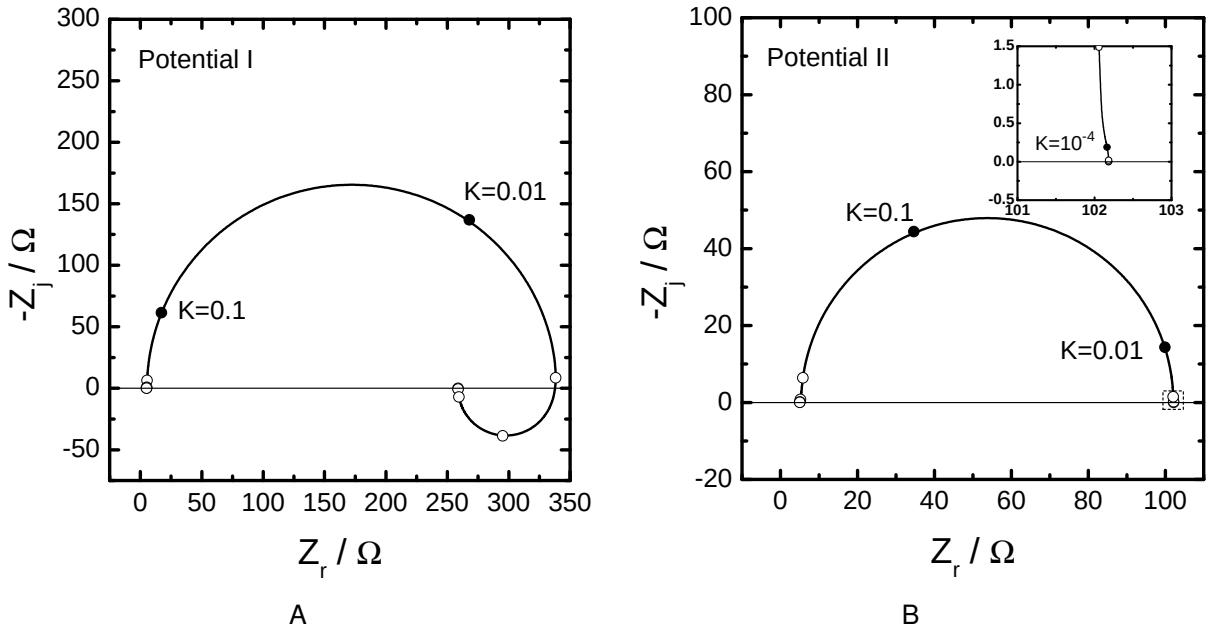

Figure 5-7. The calculated global impedance corresponding to A) polarization point I and B) point II in Figure 5-1B. These results are to be compared to the experimental results presented in Figure 5-2A and 5-2B.

Epelboin and Keddam.[48] The values of α_1 and α_2 obtained from the values of b_1 and b_2, respectively, differ from 0.5, consistent with non-elementary step reactions.[21]

The simulation results for the global impedances corresponding to potential I and II in the experimental polarization curve are presented in Figure 5-7A and 5-7B, respectively, and should be compared to experimental EIS diagrams presented in Figures 5-2A and 5-2B. The impedance values for the simulation curves are in agreement with the experimental results, with the exception that the characteristic frequency has a smaller value for steady-state condition II. This can be attributed to the uncertainties in the estimation of the kinetic parameters. The calculated global impedance has a low-frequency inductive loop at potential I, corresponding to a positive value of $\langle A \rangle$. The low-frequency feature at potential II is not very obvious, but a slight capacitive behavior can still be observed in the enlarged region at the low frequency limit, corresponding to a small negative value of $\langle A \rangle$.

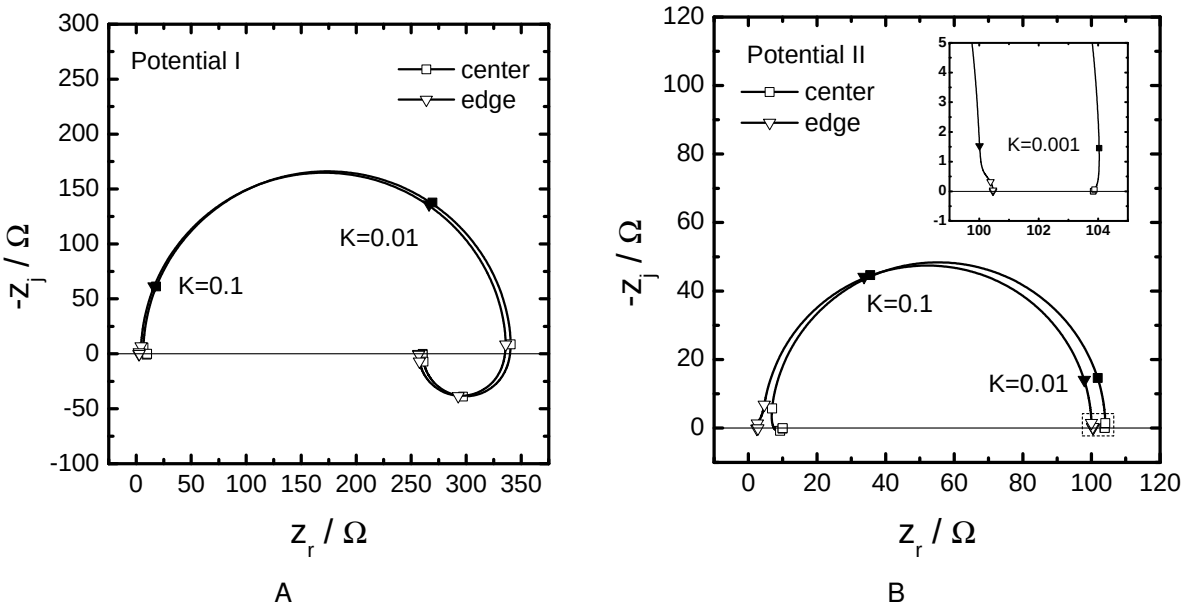

Figure 5-8. The calculated local impedance corresponding to A) polarization point I and B) point II in Figure 5-1B. These results are to be compared to the experimental results presented in Figure 5-3.

The calculated local impedance values are shown in Figure 5-8 for two different steady-state conditions. In Figure 5-8A, the local impedance calculated at potential I shows little differences between electrode center and electrode edge, in contrast to the experimental results in Figure 5-3A, especially the inductive loops at low frequencies. The reason for the larger differences in the experimental data could result from the dissolution of iron electrode during the impedance measurements at low frequencies. The iron electrode is recessed more at the edge of the electrode, and, therefore, the impedance data were measured at different heights. The discrepancy of the local impedance among different positions is larger at a higher potentiostatic condition, which is also in good agreement with the above explanation. At potential II, the calculated impedance at the center of the electrode has a inductive loop at low frequencies as shown in the enlarged region, which is in agreement with the experimental result in Figure 5-3B. It corresponds to a local positive value of A at the electrode center. The calculated impedance at the electrode edge has a capacitive feature, which

corresponds to a local negative value of A. Such a behavior is in accordance with the results presented in Chapter 4 that predicted a local variation of A with the electrode radius.

The calculated local Ohmic impedances for steady-state condition I are presented in Figure 5-9. As compared to Figure 5-4, the local Ohmic impedances at the center and the edge of the electrode have similar behaviors. Complex features are evident at low frequencies in both experimental (Figures 5-4B and 5-4C) and simulation results (Figures 5-9B and 5-9C). However, from the dependence of the imaginary part of the local Ohmic impedance on frequency shown in Figure 5-10, the complex values at low frequencies are very small as compared to that at high frequencies and are therefore barely evident.

The variation of the imaginary part of the local Ohmic impedance with frequency at potential II are given in Figure 5-11. For dimensionless frequencies $10^{-5} < K < 10^{-2}$, small values of the imaginary part are observed. This result demonstrates that the distributions of current and potential are evident at lower frequencies in which the local Ohmic impedances exhibit complex behaviors as the applied potential is increased. For a better qualitative analysis, the experimental results measured at higher potential (potential II) are compared with the calculation presented in Chapter 4 for the case of $\langle A \rangle = 0$. The calculated local Ohmic impedance at the electrode center in Figure 5-12A is presented in dimensionless format and has similar behavior as compared to that in Figure 5-6A. In Figure 5-12B, the nonzero values for the imaginary component of the local Ohmic impedance at low frequencies are more significant and can no longer be neglected.

5.5 Discussion

There were two reasons that only a qualitative comparison could be made between experimental and calculated results. The calculated impedance response corresponds to values at the electrode surface; whereas the experimental measurements necessarily

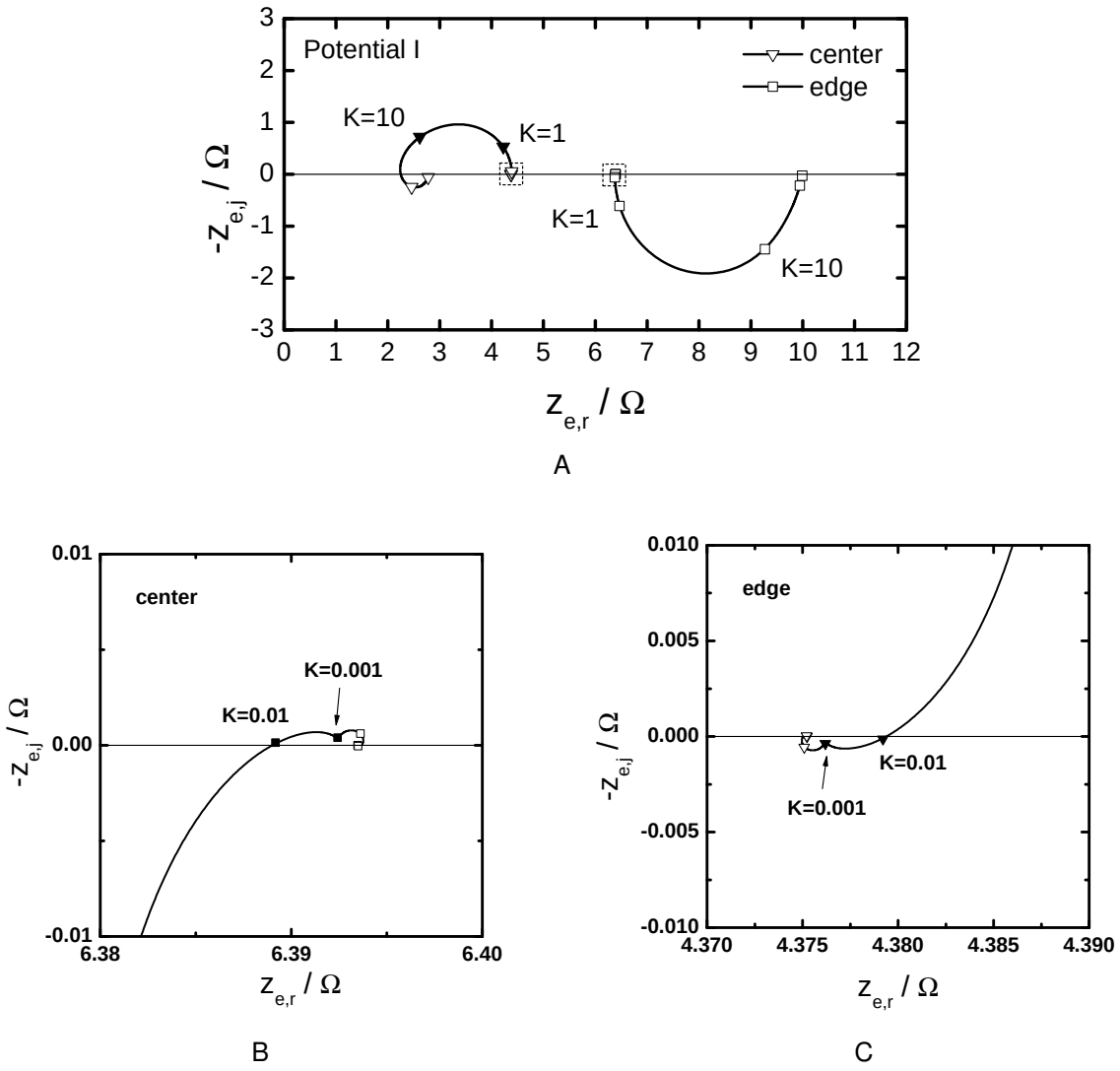

Figure 5-9. The local Ohmic impedance calculated at potential I in Figure 5-1B. A) Local Ohmic impedance at the center and the edge of the electrode; B) the enlargement for the low-frequency end of the local Ohmic impedance at the electrode center; and C) the electrode edge. These results are to be compared to the experimental results presented in Figure 5-4.

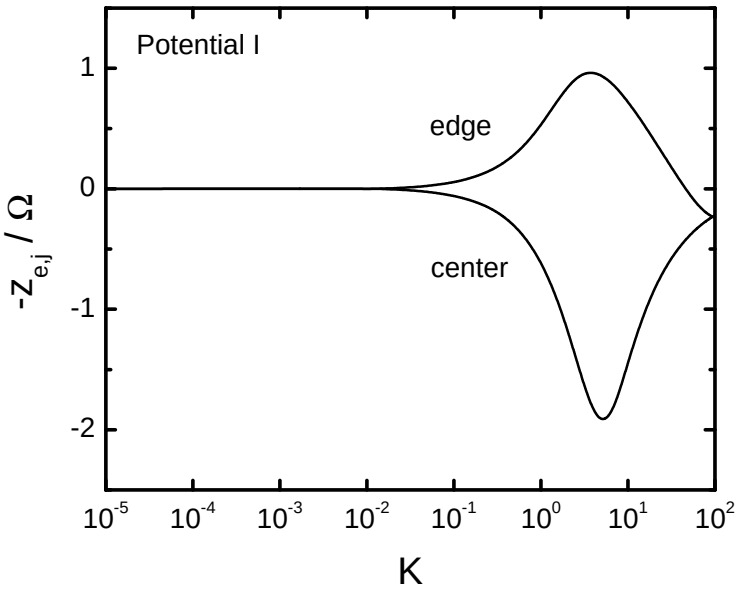

Figure 5-10. The imaginary part of the local Ohmic impedance as a function of the dimensionless frequency calculated at potential I in Figure 5-1B. This plot is to be compared to the experimental result presented in Figure 5-5.

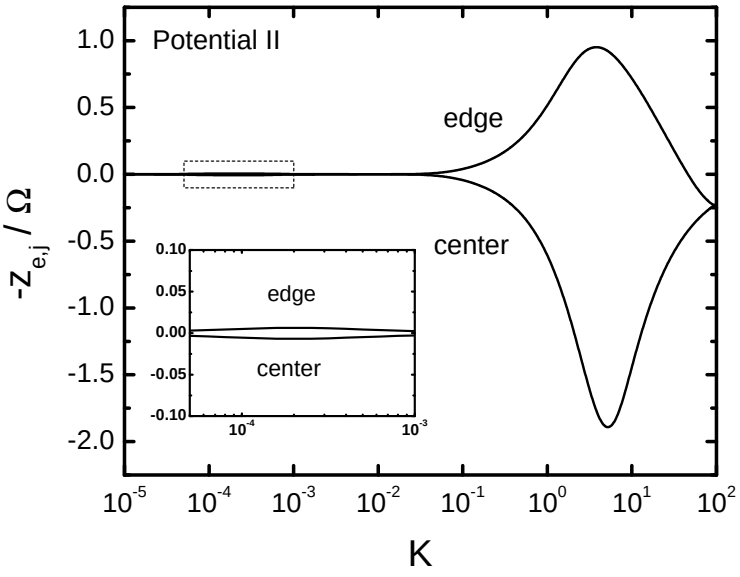

Figure 5-11. The imaginary part of the local Ohmic impedance as a function of the dimensionless frequency calculated at potential II in Figure 5-1B. This plot is to be compared to the experimental result presented in Figure 6-1B.

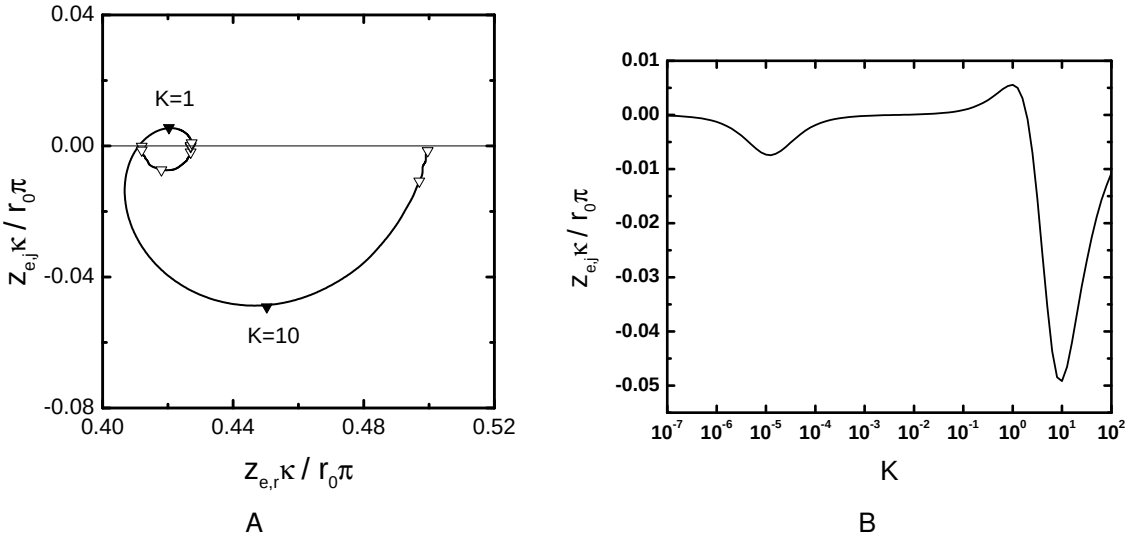

Figure 5-12. Calculated local Ohmic impedance for the case $\langle A \rangle = 0$ presented by Wu *et al.*[3] A) Nyquist plot for the local Ohmic impedances at the center of the electrode; and B) imaginary part of the local Ohmic impedance as a function of the dimensionless frequency. These results are to be compared to the experimental results presented in Figure 5-6.

are made a small distance above the electrode surface. In addition, the rapid dissolution of the iron electrode caused the distance between the probe and the electrode to change with time. During the course of a cyclic voltammetry measurement, for example, the electrode receded by 2 mm. Impedance measurements at frequencies lower than 0.1 Hz, *i.e.,* $K < 4 \times 10^{-5}$, could not be made because the time required led to significant electrode recession. In the simulation, the electrode surface is assumed to be smooth, with a position that is independent of time, and with an active area unaffected by deposition of corrosion products. Therefore the simulation cannot give a quantitative comparison to the measured results.

Nevertheless, the qualitative comparison between the experimental and the calculated impedance response provides significant supports for the simulation results. The experimental local Ohmic impedance exhibits complex values at low frequencies. These complex behaviors are more evident at a higher potential, in agreement with the theoretical calculations. Moreover, the radial dependence of the low-frequency response

demonstrates that the geometry-induced current and potential distributions influence the impedance response at low frequencies when adsorbed intermediates are involved in the reactions. The calculations are in better agreement with the experimental results at steady-state condition I. At steady-state condition II, the applied potential is more anodic, and the configuration of the iron electrode changed during the course of the experiment. However, these results show a distribution of local impedance caused by the nonuniform distributions of current and potential in agreement with the prediction presented in Chapter 4.

CHAPTER 6
INFLUENCE OF MASS TRANSFER ON STEADY-STATE CURRENT AND POTENTIAL DISTRIBUTIONS

In this chapter, we are to explore the current and potential distributions associated with the nonuniform mass transfer and the electrode geometry. The theoretical development incorporating the potential distribution with the mass transfer and electrode kinetics is provided. The coupled solutions for the potential and concentration at steady state are discussed in two redox systems: reduction of ferricyanide and oxidation of ferrocyanide, and electrochemical deposition and dissolution of silver.

6.1 Mathematical Development

Instead of using Newman's[1] approach of dividing the problem into separate but coupled domains consisting of a inner diffusion region near the electrode surface and an outer region with uniform concentration, the flux of each species is now considered in a integral domain governed by the convective diffusion equation. A mathematical development for the steady-state potential and concentration distributions on a RDE is presented in this section.

6.1.1 Mass Transport in Dilute Solutions

The mass transport of species in a dilute solution can be described by three types of motion: convection if the species is moving with the fluid of bulk velocity $\mathbf{v}$, diffusion if there is a concentration gradient ∇c_i, and migration for species of charge z_i subjected to an electric field $-\nabla\Phi$. The flux of a species i can be expressed by

$$\mathbf{N}_i = -z_i u_i F c_i \nabla\Phi - D_i \nabla c_i + c_i \mathbf{v} \tag{6–1}$$

where u_i is the mobility of species i and is related to the diffusion coefficient D_i by

$$u_i = \frac{D_i}{RT} \tag{6–2}$$

in a dilute solution. The electric current is related to the flux of the charged species by

$$\mathbf{i} = F \sum_i z_i \mathbf{N}_i \tag{6–3}$$

The mass of each species is conserved and can be expressed by the mass balance equation following

$$\frac{\partial c_i}{\partial t} = -\nabla \cdot \mathbf{N}_i + R_i \tag{6–4}$$

where R_i represents the source or sink of material due to homogeneous reactions in the bulk solution. Assuming that there is no homogeneous reaction in the electrolytic system and the diffusion coefficient of each species is constant, substitution of equation (6–1) into equation (6–4) yields the mass balance equation for each ionic species as

$$\mathbf{v} \cdot \nabla c_i = z_i u_i F \nabla \cdot (c_i \nabla \Phi) + D_i \nabla^2 c_i \tag{6–5}$$

The above equation applies at steady state and uses the relation for incompressible fluid, *i.e.,* $\nabla \cdot \mathbf{v} = 0$. For an aqueous system with n species, there are n mass balance expressions in the form of equation (6–5). The electrical potential Φ can be obtained by adding the conservation of charge

$$\nabla \cdot \mathbf{i} = \nabla \cdot \left[F \sum_i z_i \left(-z_i u_i F c_i \nabla \Phi - D_i \nabla c_i \right) \right] = 0 \tag{6–6}$$

as the additional equation.

The concentration of each species and the solution potential are governed by the mass and charge conservation equations. Before applying the boundary conditions to get the coupled solution for concentration and potential, the fluid velocity in the mass conservation equation (6–5) needs to be defined.

6.1.2 Fluid Flow on a Rotating Disk Electrode

The fluid mechanics for flow on a RDE is well-understood.[29,21,55] The rotation of disk with an angular velocity Ω drags the fluid at its surface with the same velocity. Because of the centrifugal force, the fluid near the disk surface is driven outward from

the center to the disk periphery, resulting a velocity distribution in the radial direction. The fluid at electrode surface is refilled by the flow that brings fluid from the distance to the disk, resulting a velocity distribution in the axial direction.

Von Kármán[55] and Cochran[29] solved the equations of continuity and motion for a steady motion of incompressible fluid, and derived the velocity profile by using cylindrical coordinates. The solution was obtained by using separation of variables with a dimensionless distance from the disk

$$\zeta = y\sqrt{\frac{\Omega}{\nu}} \tag{6–7}$$

and the dimensionless velocities in radial and axial directions

$$\upsilon_r = r\Omega F(\zeta) \tag{6–8}$$

and

$$\upsilon_y = \sqrt{\nu\Omega}H(\zeta) \tag{6–9}$$

where ν is the solution viscosity. For small distances above the disk surface, the dimensionless radial velocity F and axial velocity H are expressed in power series of ζ as

$$F = a\zeta - \frac{1}{2}\zeta^2 - \frac{1}{3}\zeta^3 + ... \tag{6–10}$$

and

$$H = -a\zeta^2 + \frac{1}{3}\zeta^3 + \frac{b}{6}\zeta^4 + ... \tag{6–11}$$

with coefficients $a = 0.51023$ and $b = -0.616$. For larger distances from the disk, the dimensionless velocity are expressed in powers of $e^{-c\zeta}$ as

$$F = Ae^{-c\zeta} - \frac{A^2 + B^2}{2c^2}e^{-2c\zeta} + \frac{A(A^2 + B^2)}{4c^4}e^{-3\zeta} + ... \tag{6–12}$$

and

$$H = -c + \frac{2A}{c}e^{-c\zeta} + \frac{A^2 + B^2}{2c^2}e^{-2c\zeta} + ... \tag{6–13}$$

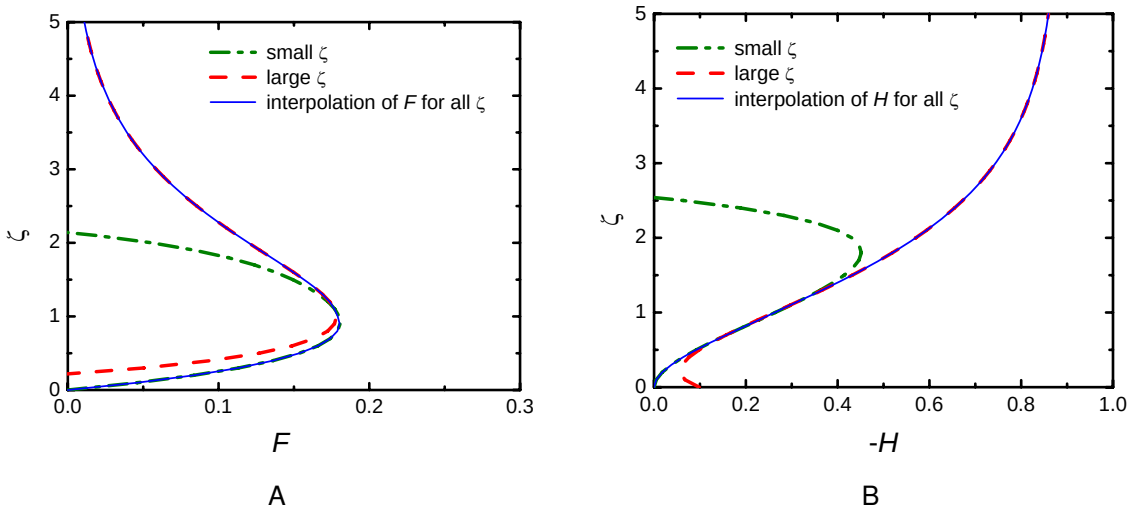

Figure 6-1. Velocity profiles on a rotating disk electrode: A) radial and B) axial components of the dimensionless velocity.

with coefficients $c = 0.88447$, $A = 0.934$, and $B = 1.208$.

To solve the mass and charge conservation equations, a velocity profile is required to describe the fluid flow in the whole domain, *i.e.,*

$$v = (1 - f)v_{\zeta \to 0} + f v_{\zeta \to \infty} \tag{6–14}$$

where f is an interpolation function that is used to weigh the velocity expansions in the inner and outer regions of diffusion layer following

$$f = \frac{1}{1 + e^{-\alpha(\zeta - \zeta_0)}} \tag{6–15}$$

where α and ζ_0 are constant. This interpolation function is similar to the Fermi-Dirac function applied in quantum mechanics for describing the distribution of fermions. In the present calculation, we used $\alpha = 25$ and $\zeta_0 = 1$ to estimate the fluid velocity profile.

Figure 6-1 shows the radial and axial components of the dimensionless velocity as a function of dimensionless distance from the electrode surface. The velocity expression applying the interpolation function satisfies the velocities for small and large values of ζ,

and shows a smooth transition in the medium distance from the disk surface. Therefore, the use of the velocity profile in equation (6–14) on a RDE is justified.

6.1.3 Flux and Current at Electrode Boundary

At electrode boundary, the flux of each species is determined by the potential and concentration gradients at electrode surface by

$$N_i = -z_i u_i F c_i \frac{\partial \Phi}{\partial y}\bigg|_{y=0} - D_i \frac{\partial c_i}{\partial y}\bigg|_{y=0} \tag{6–16}$$

The flux is also related to the current density of an electrode reaction by

$$N_i = -\frac{s_i}{nF} i \tag{6–17}$$

where s_i is the stoichiometric coefficient of species i, and n is the number of electrons transferred in that electrode reaction. For an electrochemical reaction influenced by the transport of reactants, the reaction rate is dependent on the concentrations of the reactants in addition to the potential at electrode surface. For a general redox reaction

$$\mathrm{R} \rightleftharpoons \mathrm{O} + n\mathrm{e}^- \tag{6–18}$$

the reaction rate is given by

$$i = k_\mathrm{a} c_{\mathrm{R},0} \exp\left(\frac{(1-\beta)nF}{RT} V\right) - k_\mathrm{c} c_{\mathrm{O},0} \exp\left(\frac{-\beta nF}{RT} V\right) \tag{6–19}$$

where k_a and k_c are the rate constants for the anodic and cathodic reactions, respectively, $c_{\mathrm{R},0}$ and $c_{\mathrm{O},0}$ are the concentrations for the reductant R and the oxidant O, respectively, measured at the inner limit of diffusion layer, and V is the interfacial potential defined by the difference between the electrode potential Φ_m and the solution potential adjacent to the electrode Φ_0. The symmetry factor β, or transfer coefficient, represents the fraction of energy or potential that is used to promote the cathodic reaction. The rate expression in equation (6–19) assumes that both the anodic and cathodic reactions are first-order.

When the net current for the reaction is zero, the system is at equilibrium. The equilibrium potential can be obtained by rearranging equation (6–19) and is expressed by

$$V_0 = \frac{RT}{nF}\left[\ln\left(\frac{k_\mathrm{c}}{k_\mathrm{a}}\right) - \ln\left(\frac{c_{\mathrm{O},0}}{c_{\mathrm{R},0}}\right)\right] \tag{6–20}$$

The departure of V from its equilibrium value V_0 is defined as the surface overpotential, *i.e.,*

$$\eta_s = V - V_0 \tag{6–21}$$

Substitution of the surface overpotential into equation (6–19) yields the Butler-Volmer equation as

$$i = i_0\left\{\exp\left[\frac{(1-\beta)nF}{RT}\eta_s\right] - \exp\left[\frac{-\beta nF}{RT}\eta_s\right]\right\} \tag{6–22}$$

where the exchange current density

$$i_0 = k_\mathrm{a}^{\beta} k_\mathrm{c}^{1-\beta} c_{\mathrm{R},0}^{\beta} c_{\mathrm{O},0}^{1-\beta} \tag{6–23}$$

is a function of ionic concentrations at the electrode surface, and, therefore, is a function of potential.

Another expression for the Butler-Volmer equation can be obtained by using the total overpotential η in the rate equation

$$i = i_0^{\infty}\left\{\frac{c_{\mathrm{R},0}}{c_{\mathrm{R},\infty}}\exp\left[\frac{(1-\beta)nF}{RT}\eta\right] - \frac{c_{\mathrm{O},0}}{c_{\mathrm{O},\infty}}\exp\left[\frac{-\beta nF}{RT}\eta\right]\right\} \tag{6–24}$$

where $c_{\mathrm{R},\infty}$ and $c_{\mathrm{O},\infty}$ are the bulk concentrations for the reactants R and O, respectively. The total overpotential is the summation of the surface overpotential and the concentration overpotential,

$$\eta = \eta_s + \eta_c \tag{6–25}$$

where the concentration overpotential is defined by

$$\eta_c = \frac{RT}{nF}\left[\ln\left(\frac{c_{\mathrm{R},\infty}}{c_{\mathrm{R},0}}\right) - \ln\left(\frac{c_{\mathrm{O},\infty}}{c_{\mathrm{O},0}}\right)\right] \tag{6–26}$$

The exchange current density in reaction (6–24)

$$i_0^{\infty} = k_{\mathrm{a}}^{\beta} k_{\mathrm{c}}^{1-\beta} c_{\mathrm{R},\infty}^{\beta} c_{\mathrm{O},\infty}^{1-\beta} \tag{6–27}$$

is now dependent on the composition of the bulk solution and is not a function of electrode potential. With the use of appropriate expressions for the surface flux and current density at electrode, the concentrations of each species and the potential in the solution can be obtained by solving the conservation equations (6–5) and (6–6).

6.2 Numerical Simulation

Simulations were applied to two electrochemical systems including the ferro/ferricyanide redox couple

$$\mathrm{Fe(CN)_6^{4-}} \rightleftharpoons \mathrm{Fe(CN)_6^{3-}} + \mathrm{e^-} \tag{6–28}$$

and the silver redox reaction

$$\mathrm{Ag} \rightleftharpoons \mathrm{Ag^+} + \mathrm{e^-} \tag{6–29}$$

The reduction of ferricyanide and oxidation of ferrocyanide have fast kinetics and are often used to study mass transfer in electrolytic systems.[36,37,56] The solution under study was consisted of $K_3Fe(CN)_6$ and $K_4Fe(CN)_6$ of equal concentration 0.01 M, and supporting electrolyte KCl of concentration 1 M. The rate constants were chosen to make the equilibrium potential be 0.23 V and the exchange current density be 0.3 A/cm^2.[38,57] For the silver redox reaction, the diffusion of silver ion was assumed to have negligible effect on the anodic dissolution reaction. The solution was considered to be 0.1 M $AgNO_3$ in the presence of different concentrations of supporting electrolyte KNO_3. The rate constants were chosen to make the equilibrium potential be 0.799 V,[21] and the exchange current density be 1 A/cm^2.[58,59] The solution compositions and kinetic parameters used in both systems are listed in Table 6-1.

The equations were solved by using the finite-element package *COMSOL Multiphysics*® with the Nernst-Planck module in a 2D axial symmetric coordinate system. A quarter-circle was constructed with an axis of symmetry at $r = 0$ and the electrode of

Table 6-1. Parameters used for calculating the steady-state current and potential distributions on a RDE at room temperature.

Redox of ferricyanide/ferrocyanide			Electrodeposition of silver		
$c_{K_3Fe(CN)_6,\infty}$	0.01×10^{-3}	mol/cm^3	$c_{AgNO_3,\infty}$	0.01×10^{-3}	mol/cm^3
$c_{K_4Fe(CN)_6,\infty}$	0.01×10^{-3}	mol/cm^3	$c_{KNO_3,\infty}$	1×10^{-3}	mol/cm^3
$c_{KCl,\infty}$	1×10^{-3}	mol/cm^3		0.1×10^{-3}	mol/cm^3
$D_{Fe(CN)_6^{-3}}$	0.896×10^{-5}	cm^2/s		0.01×10^{-3}	mol/cm^3
$D_{Fe(CN)_6^{-4}}$	0.739×10^{-5}	cm^2/s	D_{Ag^+}	1.648×10^{-5}	mol/cm^3
D_{Cl^-}	2.032×10^{-5}	cm^2/s	$D_{NO_3^-}$	1.902×10^{-5}	mol/cm^3
D_{K^+}	1.957×10^{-5}	cm^2/s	D_{K^+}	1.957×10^{-5}	mol/cm^3
ν	0.951×10^{-2}	cm^2/s	ν	1×10^{-2}	cm^2/s
β	0.5		β	0.5	
k_a	340	A-cm/mol	k_a	1.75×10^{-7}	A/cm^2
k_c	2.64×10^{6}	A-cm/mol	k_c	5.72×10^{10}	A-cm/mol

radius 0.25 cm was positioned at $y = 0$. The domain size was 2,000 times larger than the disk radius in order to meet the assumption that the counter electrode was located infinitely far from the electrode surface.

The meshed domain used to calculate the coupled solution for potential and concentrations are shown in Figure 6-2. A coarse mesh was used in the most of the domain distant from the electrode to reduce physical memory usage and calculation time. A finer mesh was applied in the region that is 20 times larger than the disk radius to capture the variation of potential in the vicinity of electrode. Since the concentration of ionic species varies only in a small distance above the electrode surface, a much finer mesh was constructed in the region that is ten times larger than the characteristic thickness of the diffusion layer

$$\delta = \left(\frac{3D_i}{a\nu}\right)^{1/3}\left(\frac{\nu}{\Omega}\right)^{1/2} \tag{6–30}$$

to capture the concentration variation in the thin region. For a typical electrolytic system with ionic diffusivity $D_i = 1\times10^{-5}$ cm^2/s and viscosity $\nu = 1\times10^{-2}$ cm^2/s, and for the disk rotation speed of 120 rpm, the diffusion layer thickness has a value of 0.005 cm. The number of element at the electrode-insulator boundary (0.25 $\pm$ 0.001 cm) is 100.

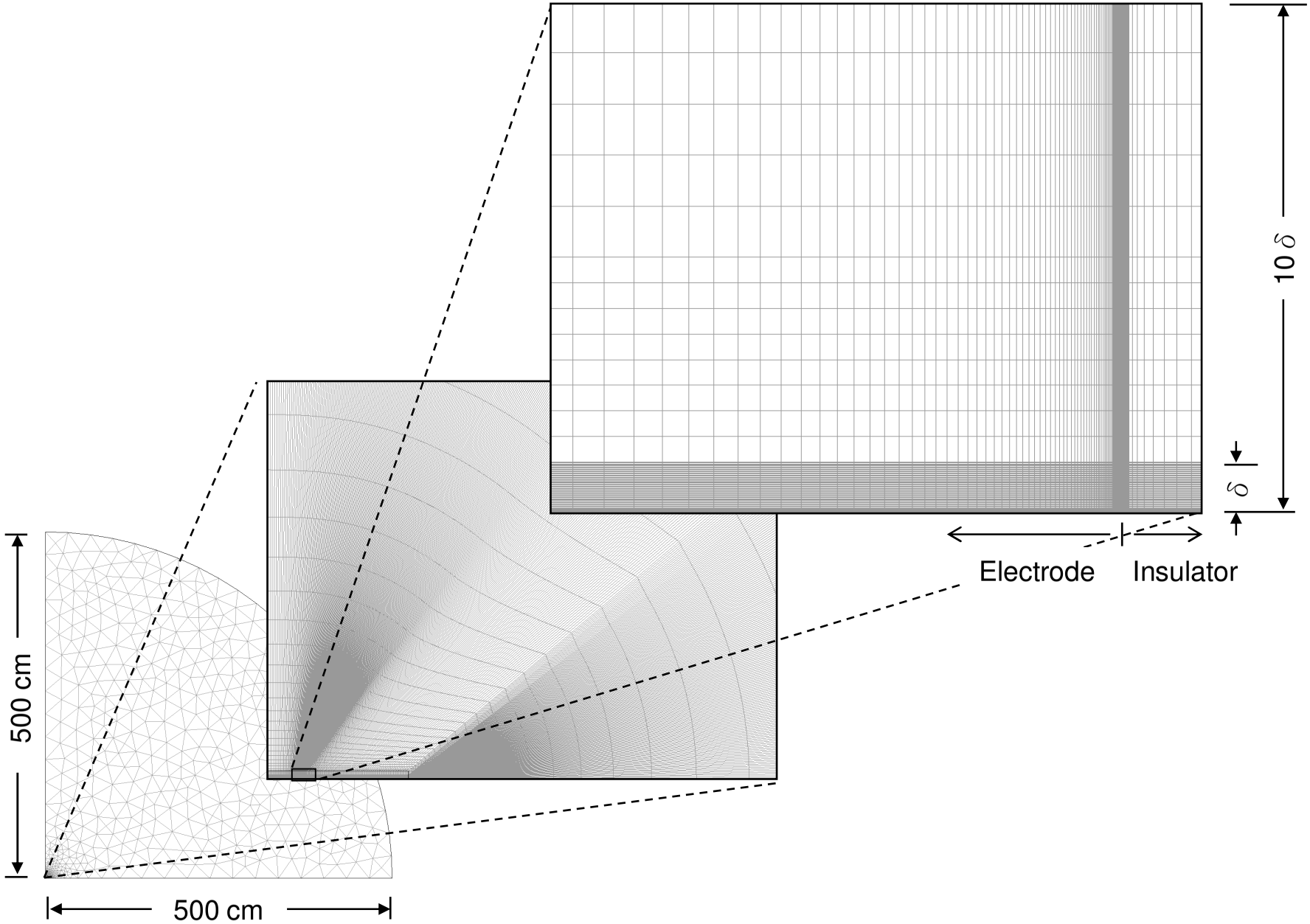

Figure 6-2. Meshed model used to calculate the potential and concentration distributions in the whole domain and near the electrode-insulator interface.

6.3 Simulation Results

The coupled steady-state solution for potential and concentration in the system containing ferro/ferricyanide redox couple and the silver redox reaction are presented in this section. The influence of nonuniform mass transfer on the potential and current distributions are discussed for different fractions of limiting current and at different rotation speeds.

6.3.1 Potential and Concentration Profiles near Electrode Surface

The motion of ionic species in an electrolytic solution is determined by the electrode reaction and the contributions of diffusion, migration, and convection to the mass flux. The 2D surface plots of the potential and concentration distributions in systems of reduction of ferricyanide and deposition of silver ion are shown in Figures 6-3A and 6-3B, respectively. The contour lines indicate the potential distributions and the surface colors represent the concentration variations of ferricyanide (Figure 6-3A) and silver (Figure 6-3B). In both figures, the concentrations vary only in a thin region above the electrode surface showing the presence of a concentration diffusion layer. The equipotential lines are smooth in the bulk solution and show a transition near the diffusion layer boundary. The transition is more significant in the system of reduction of ferricyanide due to the larger charge numbers associated with ferricyanide and ferrocyanide.

The potential and concentration profiles normal to the electrode surface for reduction of ferricyanide and deposition of silver are given in Figures 6-4 and 6-5, respectively. The potential gradient for the system of reduction of ferricyanide shows a clear change at the position where the concentration of each species approaches the bulk value. At electrode center, the net current in the radial direction is zero. The flux of supporting species is also zero at electrode surface. The flux of potassium ion at

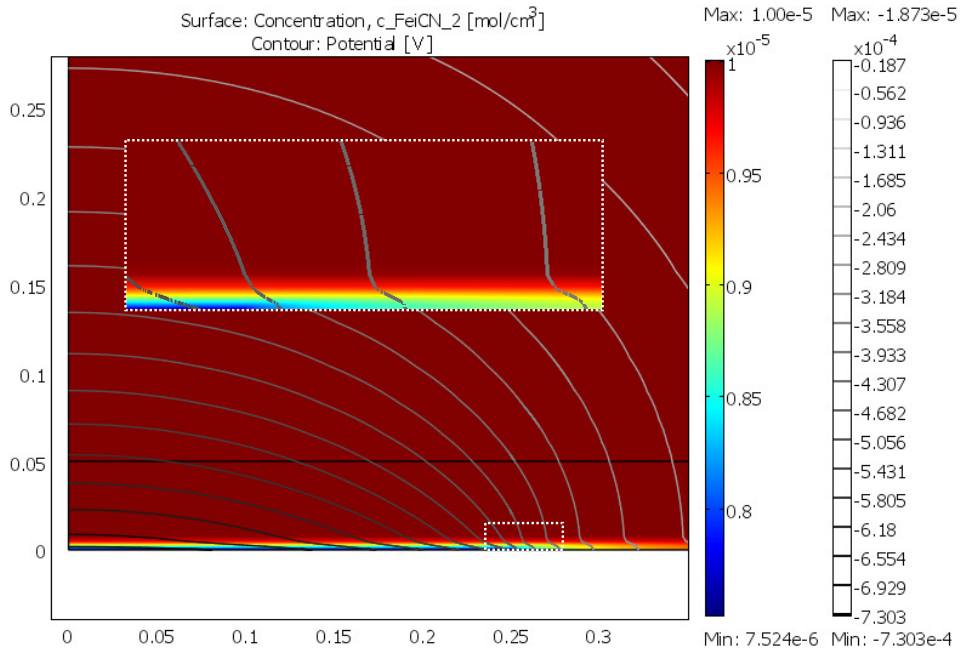

A

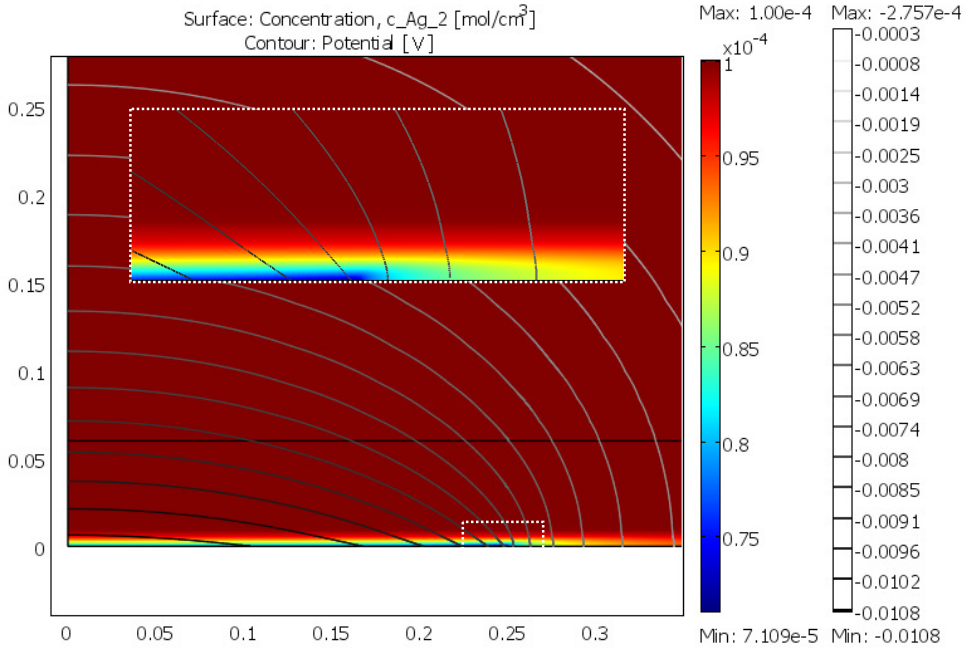

B

Figure 6-3. Steady-state potential and concentration distributions for A) reduction of ferricyanide and B) deposition of silver at one-fourth of limiting current on a rotating disk electrode rotating at 120 rpm. The surface colors represent the concentration variations of A) ferricyanide and B) silver ion. The contour lines represent the potential distributions. The inserts show the potential and concentration profiles near electrode surface.

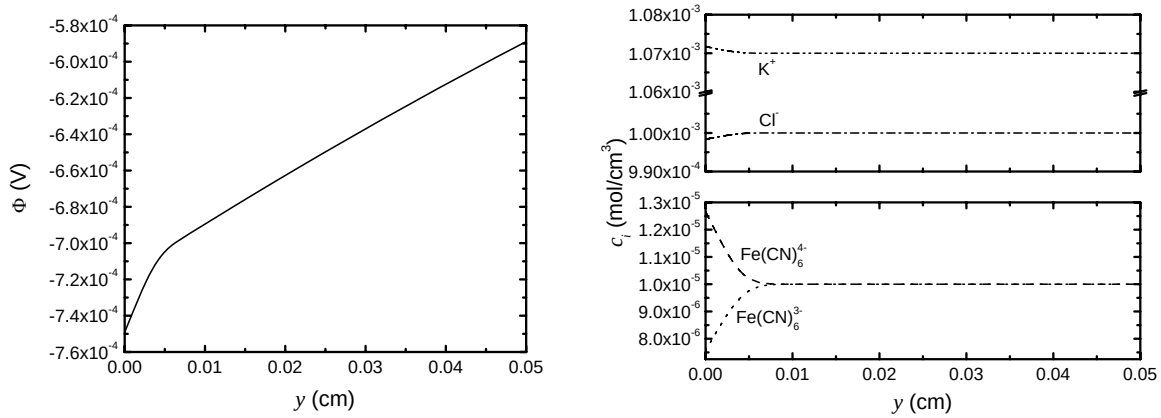

A B

Figure 6-4. Profiles of A) potential and B) concentration at electrode center for reduction of ferricyanide on a rotating disk electrode of rotation speed 120 rpm and at one-fourth of the limiting current.

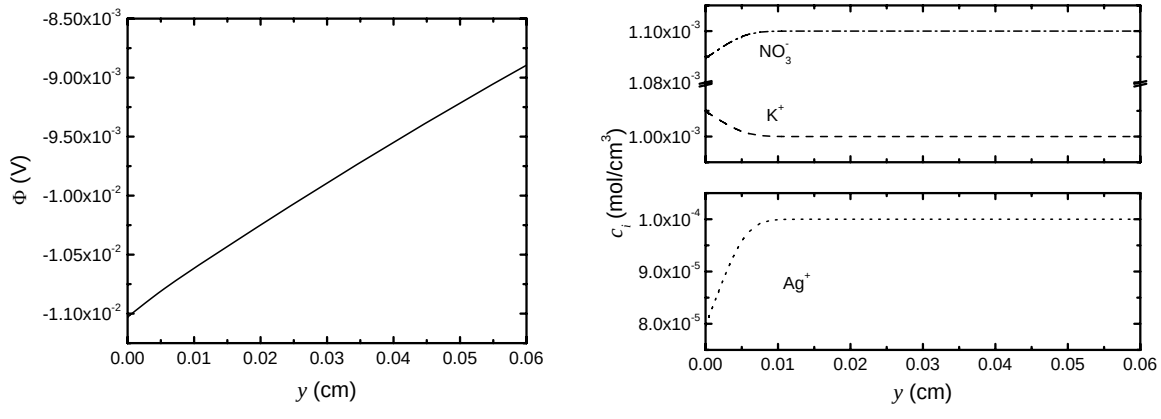

A B

Figure 6-5. Profiles of A) potential and B) concentration at electrode center for deposition of silver on a rotating disk electrode of rotation speed 120 rpm and at one-fourth of the limiting current.

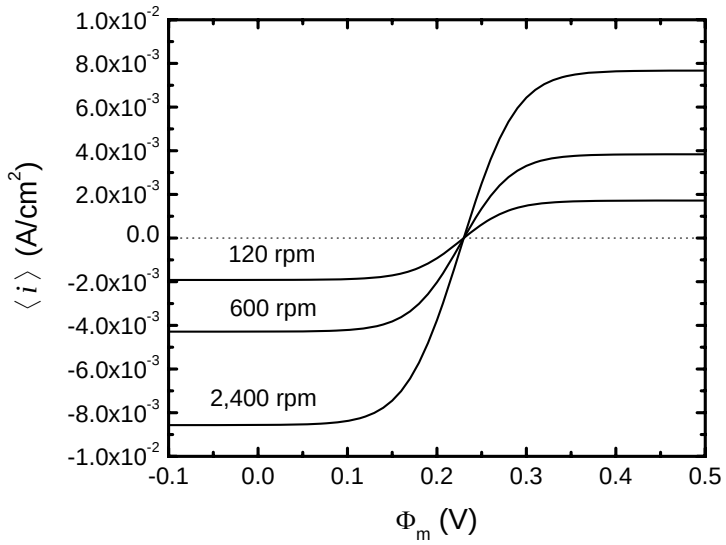

Figure 6-6. Polarization behavior for the reduction of ferricyanide and oxidation of ferrocyanide on a rotating disk electrode.

electrode is given by

$$N_{K^+} = -z_{K^+} u_{K^+} F c_{K^+} \left.\frac{\partial \Phi}{\partial y}\right|_{y=0} - D_{K^+} \left.\frac{\partial c_{K^+}}{\partial y}\right|_{y=0} = 0 \qquad (6\text{–}31)$$

Since the concentration gradient of potassium ion is negative in both systems, the potential gradient at electrode must be positive to balance the diffusion of potassium ion by the migration of itself, and gives a zero flux at electrode surface. The sign of potential gradient can also be determined from the concentration gradients of other supporting species in the electrolyte. The potential gradient in solution is affected by the current density and the concentrations of all ionic species, and therefore the potential gradient has different values within the diffusion layer and in the bulk solution.

6.3.2 Current Distribution on Electrode Surface

The polarization behavior for the reduction of ferricyanide and oxidation of ferrocyanide is shown in Figure 6-6 with rotation speed as as parameter. At higher potentials, the electrode reaction is limited by the mass transfer of reacting species to the electrode surface. The cathodic and anodic limiting currents have different values due to

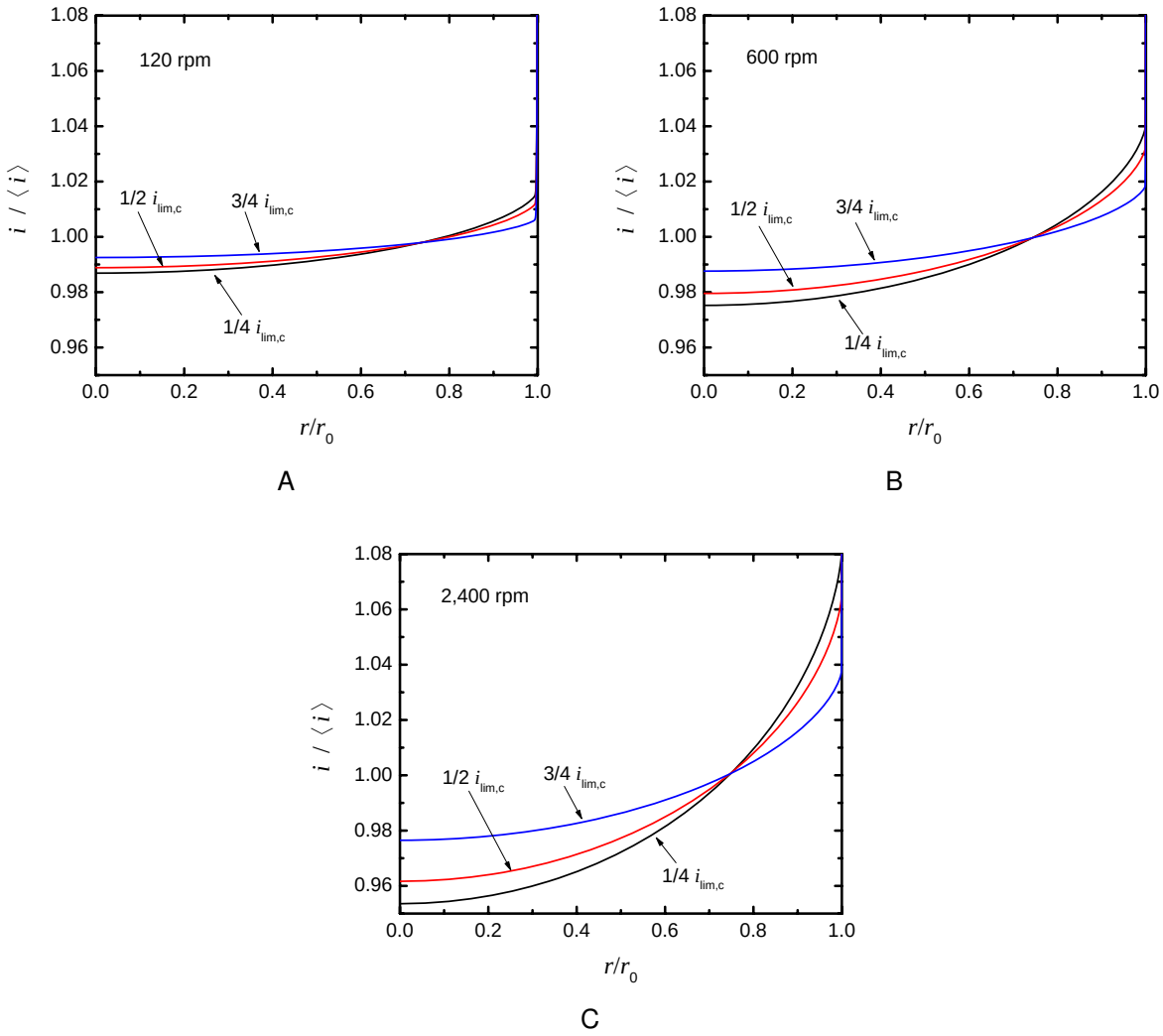

Figure 6-7. Calculated current distributions for the reduction of ferricyanide on a rotating disk electrode rotating at A) 120, B) 600, and C) 2400 rpm.

the fact that the diffusion coefficients for ferricyanide and ferrocyanide are different. The value of limiting current is proportional to the square root of the rotation speed.[28]

The current distributions on electrode surface are calculated at one-fourth, one-half, and three-fourths of the cathodic limiting current as shown in Figure 6-7. The surface current density is normalized by the average current density obtained at each fraction of limiting current. The surface current exhibits nonuniform distributions in spite of the use of excess supporting electrolyte. These results are in agreement with the calculations of Durbha and Orazem.[36] At a larger fraction of limiting current, the surface current density

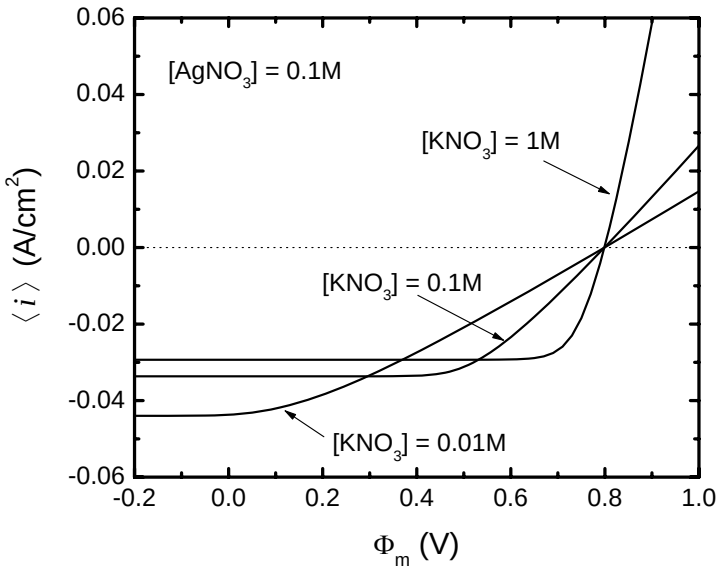

Figure 6-8. Polarization behavior for the dissolution and deposition of silver on a rotating disk electrode of rotation speed 120 rpm. The solution consists of 0.1 M $AgNO_3$ and 1 M, 0.1 M, and 0.01 M of supporting electrolyte KNO_3.

becomes more uniform because the mass transfer resistance is more important than the Ohmic resistance of electrolyte. For the same reason, the overall current distribution is more uniform at higher rotation speed.

The reaction kinetics of reduction of ferricyanide and oxidation of ferrocyanide are highly related to the concentration of cation, *i.e.,* the concentration of supporting electrolyte.[60] To ignore the effect of reaction kinetics, the redox reaction of silver is applied to investigate the role of supporting electrolyte on the current distribution. The polarization curves for the deposition and dissolution of silver in different concentrations of supporting electrolyte are given in Figure 6-8. In the case of metal deposition, the absence of supporting electrolyte increases the Ohmic potential drop in the bulk solution and also strengthen the electric field in the diffusion layer. Therefore, the migration of reacting species in the diffusion layer enhances the limiting current density. In the presence of an excess supporting electrolyte, the limiting current on a rotating disk

electrode is expressed by[61]

$$i_{\mathrm{lim,D}} = -s_i n F D_i \frac{c_{\infty,i}}{\delta} \frac{1}{\Gamma(4/3)} \tag{6–32}$$

which is also called the diffusion limiting current. The effect of migration in an electrolytic system can be estimated by the ratio of the observed limiting current to the diffusion limiting current $i_{\mathrm{lim}}/i_{\mathrm{lim,D}}$. The migration enhances the limiting current when the ratio is greater than one, and reduces the limiting current when the ratio is smaller than one. The migration of reactant makes no contribution when the ratio is unity. For the system under study, the ratio of $i_{\mathrm{lim}}/i_{\mathrm{lim,D}}$ has a value of 1.48 when the solution contains 0.1 M $AgNO_3$ and 0.01 M KNO_3, meaning that the migration of silver ion in the diffusion layer enhances the limiting current by a factor of 1.48.

Figure 6-9 shows the current distributions on the disk surface in different concentrations of supporting electrolyte. The reduced Ohmic potential drop in the presence of excess supporting electrolyte makes the distribution of current more uniform. The current density increases with the increasing overpotential towards the edge of the disk. When the overpotential is sufficiently large and the concentration of reactant is sufficiently small at electrode edge, the electrode reaction is limited by the mass transfer of reactant. Therefore, the current density starts to decrease at electrode edge as seen in Figure 6-9C for the case of larger fraction of limiting current.

In the system of fast electrode kinetics, the current and potential distributions on a rotating disk electrode are affected by the nonuniform mass transfer and the electrode geometry. The effect of mass transfer can be reduced with higher rotation speed or eliminated by performing the reaction at the mass-transfer-limited current. However, the distributions of current and potential can never be uniform even with the use of excess supporting electrolyte. The reason is because a nonuniform Ohmic potential drop is present in the bulk solution associated with the electrode geometry. The opposing effects of the Ohmic resistance and the mass-transfer resistance can be observed

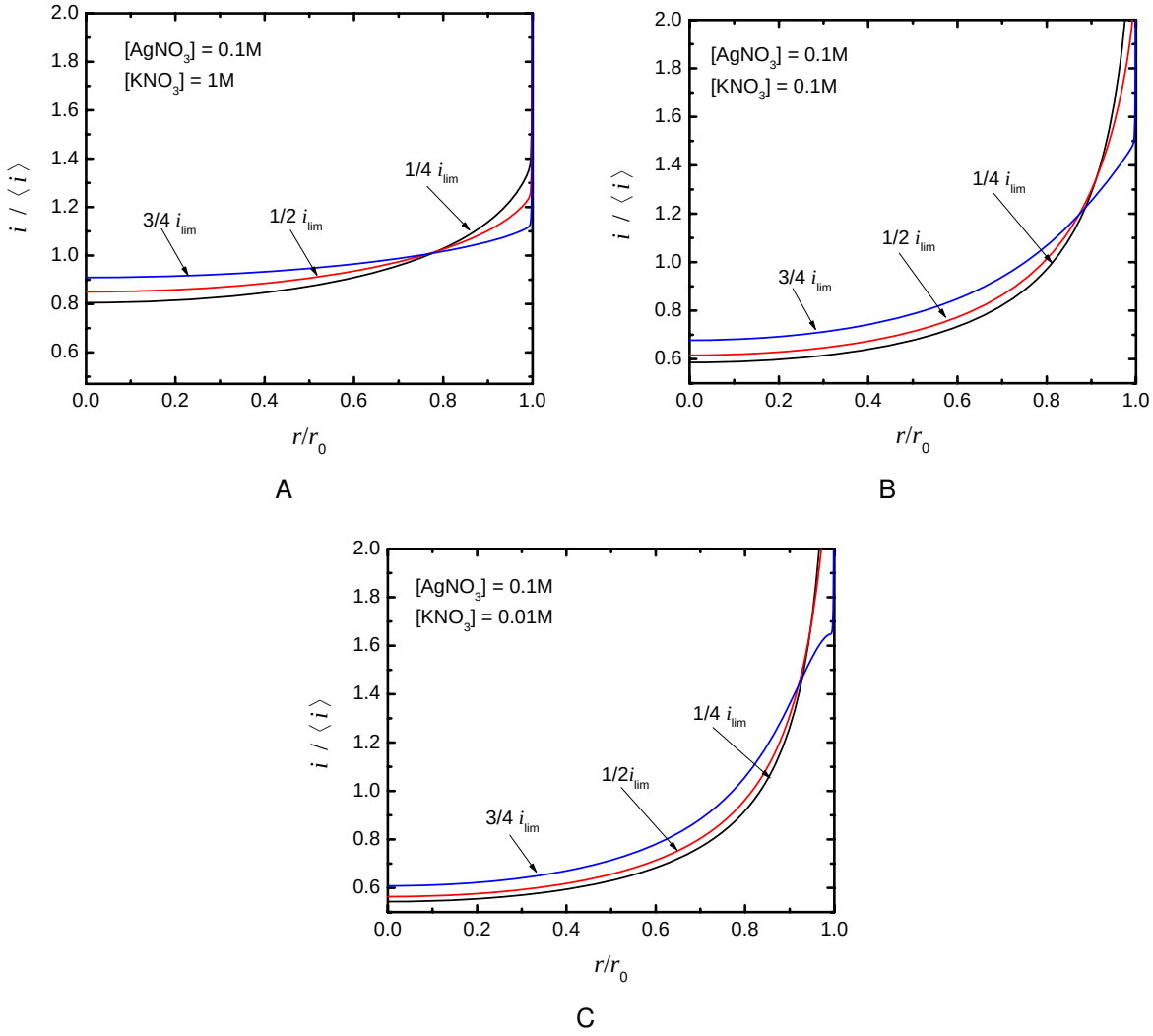

Figure 6-9. Calculated current distributions for silver deposition on a rotating disk electrode rotating at 120 rpm. The solution contains 0.1 M $AgNO_3$ and A) 1 M, B) 0.1 M, and C) 0.01 M KNO_3.

when both values are large in solutions of small conductivities and approaching the mass-transfer-limited conditions.

CHAPTER 7
MODEL OF ELECTRICAL DOUBLE LAYER

The nature of the electrode-electrolyte interface involves the distribution of electrons, ions, and molecules. A charged electrode holds excess ions in the adjacent solution, and a diffuse layer of charge is formed. The electric behavior of the interface is therefore very different from that of the bulk solution, and is related to the excess or deficient concentration of species and the potential drop in the thin interfacial region. The term “electrical double layer” came from the image of the interface as consisting of two layers of charge, one at the electrode surface and the other in the adjacent electrolyte. The real structure of interface is surely more complicated when taking into account the orientation of dipoles and the specific adsorption of ionic species.

Numerous models[62,63] have been applied to describe the thermal behavior of the charged ions in the electrical double layer. In the present study, we use the Gouy-Chapman-Stern model to describe the electrical behavior in the diffuse double layer. The change of surface charge density resulting from the variations of potential and concentrations at the interface are discussed in this chapter. These properties of the interface will be used to modify the electrode process associated with the double-layer charging and the Faradaic charging currents, which are important in studying the impedance response of systems with mass transfer.

7.1 The Gouy-Chapman-Stern Theory

The classical Gouy-Chapman theory shows an exponential decay of potential in a diffuse region of charge extending from the electrode surface. Stern’s modification to the Gouy-Chapman model assumes a compact layer between the electrode and the diffuse layer. The outer limit of the compact layer is also referred to as the outer Helmholtz plane (OHP) which is the locus of centers of mobile species in their position of closet approach to the electrode surface. When there is specific adsorption on electrode surface, the locus of centers of adsorbed species is taken to be the inner Helmholtz

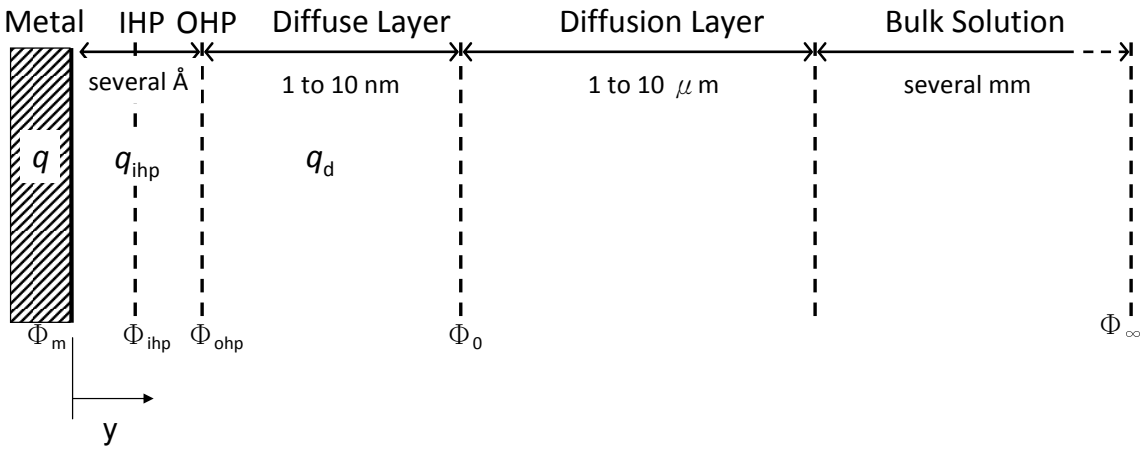

Figure 7-1. The structure of electrical double layer. The sketch is not to scale.

plane (IHP). The structure of the electrical double layer is illustrated in Figure 7-1. The thickness of the double layer is very thin. Hence the double layer is often considered to be a part of the electrode-electrolyte interface. The interfacial region as a whole obeys electrical neutrality, *i.e.,* the excess surface charge density at electrode must be balanced by the surface charges at the IHP and in the diffuse part of the double layer such that

$$q_{\mathrm{m}} + q_{\mathrm{ihp}} + q_{\mathrm{d}} = 0 \tag{7–1}$$

The surface charge density is related to the surface excess concentration of charged species by

$$q_{\mathrm{m}} = -\left(q_{\mathrm{ihp}} + q_{\mathrm{d}}\right) = -F\sum_i z_i \Gamma_i \tag{7–2}$$

The mean electrostatic potentials at the metal surface, the IHP, and the OHP are denoted by Φ_{m}, Φ_{ihp}, and Φ_{ohp}, respectively. The surface concentrations $c_{i,0}$ and potential Φ_0 used in the rate expressions are usually evaluated at the outer limit of the diffuse layer, or the inner limit of the diffusion layer.

Beyond the OHP, the total charge in the diffuse part of the double layer is not electrically neutral. The ionic concentrations in the diffuse layer are assumed to have a

Boltzmann distribution

$$c_i = c_{i,\infty} \exp\left(-\frac{z_i F \Phi}{RT}\right) \tag{7–3}$$

and the Poisson equation gives the correlation between the concentrations and potential by

$$\frac{\mathrm{d}^2\Phi}{\mathrm{d}y^2} = -\frac{F}{\epsilon_\mathrm{d}\epsilon_0}\sum_i z_i c_i = -\frac{F}{\epsilon_\mathrm{d}\epsilon_0}\sum_i z_i c_{i,\infty} \exp\left(-\frac{z_i F \Phi}{RT}\right) \tag{7–4}$$

where y is the distance from the electrode, ϵ_d is the dielectric constant in the diffuse layer, and ϵ_0 is the permittivity of vacuum ($\epsilon_0 = 8.8542 \times 10^{-14}$ F/cm). Integration of the Poisson equation gives the relation of potential gradient to the surface charge density in the diffuse layer as

$$\frac{\mathrm{d}\Phi}{\mathrm{d}y} = \frac{q_\mathrm{d}}{\epsilon_\mathrm{d}\epsilon_0} \qquad \text{at } y = \delta \tag{7–5}$$

where δ is at the inner limit of the diffuse layer. At equilibrium, the potential approaches zero in a large distance from the electrode surface, *i.e.,*

$$\Phi \to 0 \qquad \text{as } y \to \infty \tag{7–6}$$

The Poisson equation can then be solved by applying the boundary conditions, and the charge density in the diffuse layer is found to be

$$q_\mathrm{d} = \mp\left\{2RT\epsilon_\mathrm{d}\epsilon_0 \sum_i c_{i,\infty}\left[\exp\left(\frac{-z_i F \Phi_\mathrm{ohp}}{RT}\right) - 1\right]\right\}^{\frac{1}{2}} \tag{7–7}$$

The upper sign is used if the potential is positive and, conversely, the lower sign is used if the potential is negative. The charge density associated with individual species can be further obtained by an integral over the potential drop in the diffuse region following

$$q_{\mathrm{d},i} = \mp\int_0^{\Phi_\mathrm{ohp}} \frac{z_i F c_{i,\infty}\left[\exp\left(\frac{-z_i F\Phi}{RT}\right) - 1\right]}{\left\{\frac{2RT}{\epsilon_\mathrm{d}\epsilon_0}\sum_k c_{k,\infty}\left[\exp\left(\frac{-z_k F\Phi}{RT}\right) - 1\right]\right\}^{\frac{1}{2}}}\mathrm{d}\Phi \tag{7–8}$$

If there is no specific adsorption of species on the IHP, *i.e.,* $q_{\mathrm{ihp}} = 0$, the individual charge density is related to the surface concentration by

$$q_{\mathrm{d},i} = z_i F \Gamma_i \tag{7–9}$$

The above expressions for charge densities are derived by assuming a true equilibrium of the system in which the ionic concentrations at the outer limit of the diffuse layer are the same as the bulk values, $c_{i,0} = c_{i,\infty}$, and the potential at the outer limit of the diffuse layer is equal to that of a reference electrode placed at a distance; thus, $\Phi_0 = 0$. When the net current flowing to the electrode is not equal to zero, the system is not at equilibrium, *i.e.,* $\Phi_0 \neq 0$. Equations (7–7) and (7–8) become

$$q_{\mathrm{d}} = \mp \left\{ 2RT\epsilon_{\mathrm{d}}\epsilon_0 \sum_i c_{i,0} \left[\exp\left(\frac{-z_i F(\Phi_{\mathrm{ohp}} - \Phi_0)}{RT} \right) - 1 \right] \right\}^{\frac{1}{2}} \tag{7–10}$$

and

$$q_{\mathrm{d},i} = \mp \int_{\Phi_0}^{\Phi_{\mathrm{ohp}}} \frac{z_i F c_{i,0} \left[\exp\left(\frac{-z_i F \Phi}{RT} \right) - 1 \right]}{\left\{ \frac{2RT}{\epsilon_{\mathrm{d}}\epsilon_0} \sum_k c_{k,0} \left[\exp\left(\frac{-z_k F \Phi}{RT} \right) - 1 \right] \right\}^{\frac{1}{2}}} \mathrm{d}\Phi \tag{7–11}$$

respectively. The charge densities in the diffuse layer are now related to the concentrations and potential at the outer limit of the diffuse layer, which can be obtained by solving the mass and charge conservation equations outside the diffuse region of charge.

The evaluation of the surface charge density in equation (7–7) or (7–10) requires additional information in the electrical double layer. Gauss's law relates the surface charge density to the electric field within the OHP by

$$q_{\mathrm{m}} = -q_{\mathrm{d}} = \frac{\epsilon\epsilon_0}{\delta}(\Phi_{\mathrm{m}} - \Phi_{\mathrm{ohp}}) \tag{7–12}$$

where ϵ is the dielectric constant between the metal surface and the OHP. Equation (7–12) can be used as a second equation to solve q_{m} and Φ_{ohp} in the electrical double layer.

7.2 Numerical Approach

The nonlinear equations relating to the charge and potential distributions in the electrical double layer were solved by using the Newton-Raphson method. For nonequilibrium systems, a local equilibrium was assumed in which the concentrations and potential at the outer limit of the diffuse layer were given by the steady-state solutions calculated in Chapter 6. The radially dependent surface concentrations and potential gave a radial distribution of charge over the electrode surface. The surface-averaged value of charge was obtained from the surface-averaged values of concentration and potential. The charge in the diffuse layer associated with individual species was obtained by subsequent numerical integration of equation (7–8) or (7–11), using the MATLAB integration function, the adaptive Gauss-Kronrod quadrature method. The thickness of the compact layer between the metal surface and the OHP was assumed to be 3 Å. The dielectric constant in the compact region within the OHP was approximately 6 according to Bockris[63] for a fully oriented water layer next to the electrode surface. The dielectric constant in the diffuse layer was assumed to be 78, which is the value of water at room temperature.

The calculation of surface charge density in the electrical double layer was applied to systems of ferro/ferricyanide redox couple and electrolytic deposition and dissolution of silver.

7.3 Surface Charge in the Diffuse Part of the Double Layer

The calculated charge density and the charge associated with individual species in the diffuse part of the double layer are shown in Figure 7-2 for the system containing ferro/ferricyanide. The total charge density is equal to zero when the electrode is at the potential of zero charge Φ_{pzc}, which is assumed to be zero in this system. The contribution of charge from each species is affected by the redox reaction taking place at the interface. The concentrations of each species calculated at the outer limit of the diffuse layer are shown in Figure 7-3. When the electrode potential is negative, the

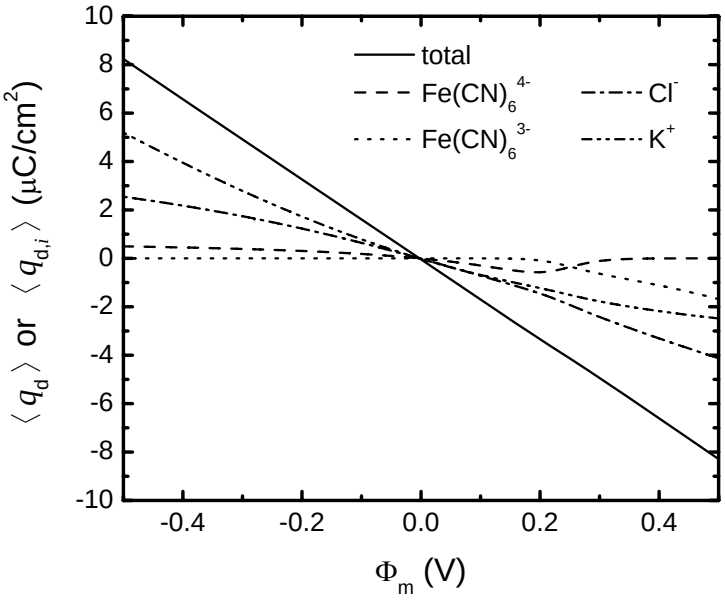

Figure 7-2. Calculated total charge density in the diffuse part of the double layer and the contribution of each ionic species. The electrolytic solution contains 0.01 M $K_3Fe(CN)_6$, 0.01 M $K_4Fe(CN)_6$ and 1 M KCl.

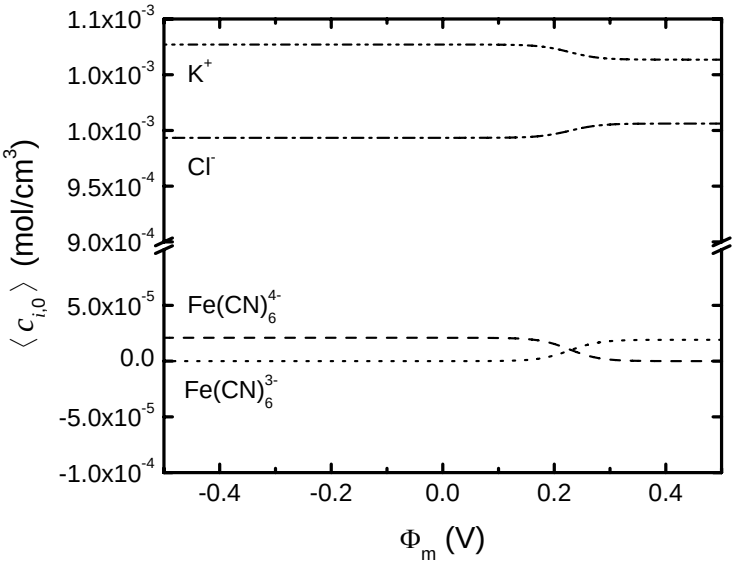

Figure 7-3. Calculated averaged ionic concentrations at the outer limit of the diffuse. The electrolytic solution contains 0.01 M $K_3Fe(CN)_6$, 0.01 M $K_4Fe(CN)_6$ and 1 M KCl.

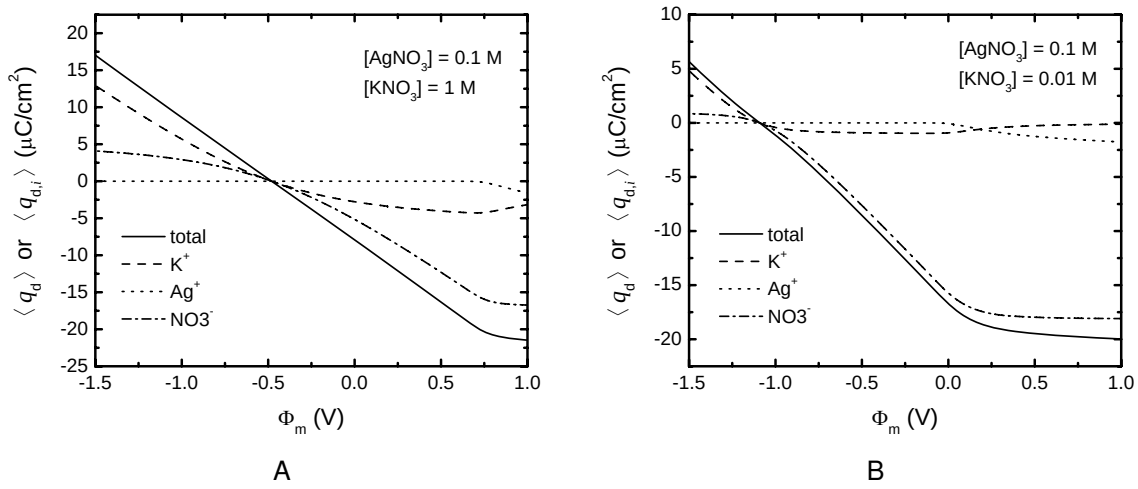

Figure 7-4. Calculated total charge density in the diffuse part of the double layer and the contribution of each ionic species. The electrolytic solution contains 0.1 M $AgNO_3$ and A) 1 M, and B) 0.01 M KNO_3.

reaction is in the cathodic limited case where the concentration of ferricyanide is zero. The charge density associated with ferricyanide is also zero at negative potentials as seen in Figure 7-2. The charge contribution from ferrocyanide is positive, representing a depletion of ferrocyanide species in the diffuse region. When the electrode potential becomes positive, the charge density associated with ferricyanide increases due to the production of ferricyanide from the oxidation of ferrocyanide. The charge density of ferricyanide keeps increasing at even higher potentials when the anodic limited condition is attained because the positive charge on the electrode tends to hold more negative charged species in the diffuse layer. The charge density associated with ferrocyanide also increases when the electrode potential turns positive. However, when approaching the equilibrium potential ($V_0 = 0.23$ V), the concentration of ferrocyanide starts to decrease due to the oxidation reaction, resulting a decrease of charge contribution from the ferrocyanide species.

For the reaction of silver deposition and dissolution, the silver ion is the only reacting species. The calculated charge density in the diffuse layer and the concentrations of each species at the outer limit of the diffuse layer are presented in Figure 7-4 and Fig-

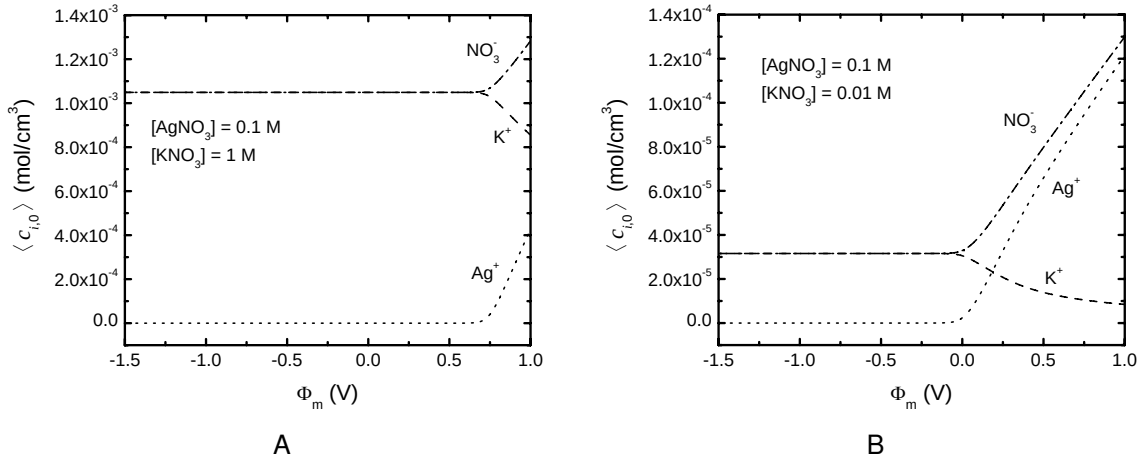

Figure 7-5. Calculated averaged ionic concentrations at the outer limit of the diffuse. The electrolytic solution contains 0.1 M $AgNO_3$ and A) 1 M, and B) 0.01 M KNO_3.

ure 7-5, respectively. The potential of zero charge for the silver electrode is assumed to be $\Phi_{\mathrm{pzc}} =$ -0.44 V.[63] The silver ion starts to have a contribution to the total charge when the deposition of silver is not limited by the mass transfer of silver ion. The negative charge contribution from the silver ion at positive potentials represents the depletion of silver ion in the diffuse layer. The dependence of charge density on electrode potential is associated with the mass transfer of silver ion. As seen in Figure 7-4, the slope for q_{d} changes at the potential corresponding to the increase of silver concentration observed in Figure 7-5.

Under the assumption that there is no specific adsorption, the surface charge on the electrode side is balanced by the charge density in the diffuse part of the double layer to maintain electroneutrality in the interfacial region. Since the surface charge density is dependent on the interfacial potential and concentrations of each species, the variation of the surface charge density is associated with the variation of interfacial potential and the variation of concentration of individual species by

$$\mathrm{d}q_{\mathrm{m}} = \left(\frac{\partial q_{\mathrm{m}}}{\partial V}\right)_{c_{i,0}} \mathrm{d}V + \sum_i \left(\frac{\partial q_{\mathrm{m}}}{\partial c_{i,0}}\right)_{V, c_{j,0, j\neq i}} \mathrm{d}c_{i,0} \qquad (7\text{–}13)$$

The two derivatives, $(\partial q_{\mathrm{m}}/\partial V)_{c_{i,0}}$ and $(\partial q_{\mathrm{m}}/\partial c_{i,0})_{V,c_{j,0,j\neq i}}$, are essential properties of the electrical double layer. Grahame[64] and Delahay[62,65–67] discussed the method to evaluate these properties. In this section, the calculation for the change of surface charge density resulting from the variation of the interfacial potential and the concentration are presented.

7.3.1 Variation of Surface Charge with Potential: Double-Layer Capacitance

The derivative of the surface charge density with respect to the interfacial potential at constant composition is known as the double-layer capacitance

$$C_0 = \left(\frac{\partial q_{\mathrm{m}}}{\partial V}\right)_{c_{i,0}} \tag{7–14}$$

Since the interfacial potential is defined by

$$V = \Phi_{\mathrm{m}} - \Phi_0 = (\Phi_{\mathrm{m}} - \Phi_{\mathrm{ohp}}) + (\Phi_{\mathrm{ohp}} - \Phi_0) \tag{7–15}$$

the derivative of potential with respect to the surface charge density yields

$$\left(\frac{\partial V}{\partial q_{\mathrm{m}}}\right)_{c_{i,0}} = \left(\frac{\partial(\Phi_{\mathrm{m}} - \Phi_{\mathrm{ohp}})}{\partial q_{\mathrm{m}}}\right)_{c_{i,0}} + \left(\frac{\partial(\Phi_{\mathrm{ohp}} - \Phi_0)}{\partial q_{\mathrm{m}}}\right)_{c_{i,0}} \tag{7–16}$$

or

$$\frac{1}{C_0} = \frac{1}{C_{\mathrm{m-ohp}}} + \frac{1}{C_{\mathrm{d}}} \tag{7–17}$$

where $C_{\mathrm{m-ohp}}$ is the capacity of the compact layer next to the electrode surface within OHP, and C_{d} is the capacity of the diffuse part of the double layer. From the integrated form of Gauss's law, $C_{\mathrm{m-ohp}}$ can be calculated by assuming a uniform dielectric constant between the metal and the OHP expressed by

$$C_{\mathrm{m-ohp}} = \frac{\epsilon\epsilon_0}{\delta} \tag{7–18}$$

The analytical expression for the capacity in the diffuse layer is obtained from the derivative of surface charge in equation (7–10) with respect to the potential drop across

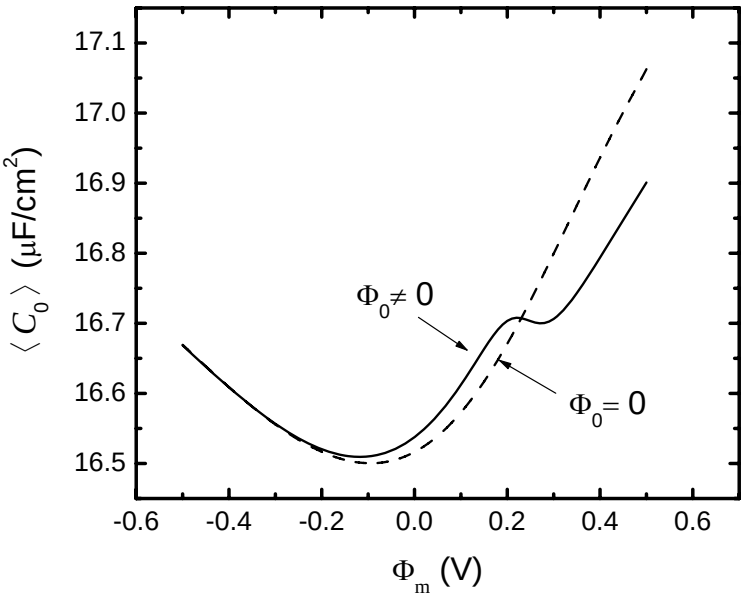

Figure 7-6. Potential dependence of double-layer capacitance for system of ferro/ferricyanide redox couple in the presence of an excess supporting electrolyte.

the diffuse layer

$$C_{\mathrm{d}} = \pm \frac{-F \sum_i z_i c_{i,0} \exp\left(-\frac{z_i F\left(\Phi_{\mathrm{ohp}} - \Phi_0\right)}{RT}\right)}{\left\{\frac{2RT}{\epsilon_{\mathrm{d}}\epsilon_0} \sum_i c_{i,0} \exp\left[-\frac{z_i F}{RT}\left(\Phi_{\mathrm{ohp}} - \Phi_0\right) - 1\right]\right\}^{\frac{1}{2}}} \tag{7–19}$$

With the above definitions, the capacitance of the double layer can be evaluated with the use of appropriate parameters instead of assuming a certain value in the subsequent calculation of impedance response.

The surface-averaged double-layer capacitance for an inert electrode in contact with ferro/ferricyanide redox couple is presented in Figure 7-6. The double-layer capacitance was calculated under two conditions. The first assumed the equilibrium condition ($\Phi_0 = 0$), in which case the concentrations and potential at the outer limit of the double layer were equal to the values far away from the electrode. The second condition ($\Phi_0 \neq 0$) used the the steady-state solutions for the concentrations and potential calculated at the outer limit of the diffuse region of charge. When the system

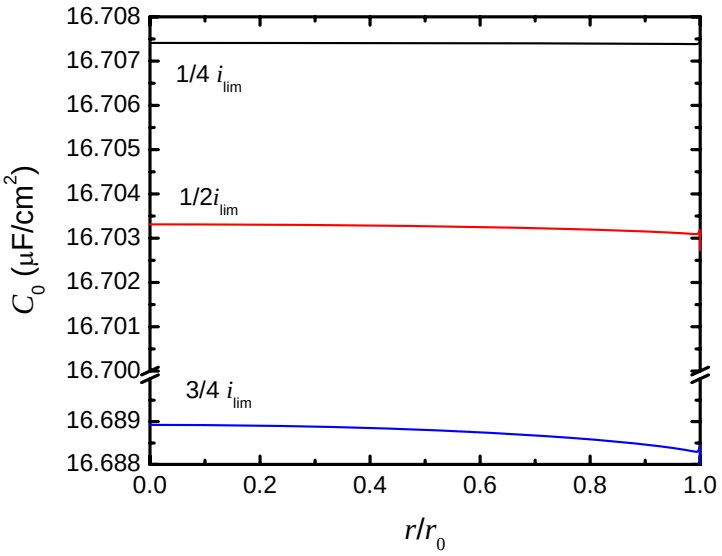

Figure 7-7. Radially dependent double-layer capacitance calculated at different fractions of limiting current for reduction of ferricyanide in the presence of an excess supporting electrolyte.

is at equilibrium, the calculated capacitance at the electrode interface should follow the typical behavior predicted by the Gouy-Chapman model of diffuse layer, that is, a symmetric capacitance over the potential of zero charge ($\Phi_{\mathrm{pzc}} = 0$). Since the electrolytic solution contains asymmetric ionic species, the capacitance-potential curve shifts to a potential negative than Φ_{pzc}. When the composition of electrolyte adjacent to the electrode is different from the bulk solution, the double-layer capacitance shows a hump near the equilibrium potential, which should be related to the relative charge contributions from the reacting species in the diffuse region.

The variations of surface concentrations and potential along electrode surface result in a distribution of surface charge density, and, therefore, a distribution of double-layer capacitance associated with the electrode geometry and kinetics. As shown in Figure 7-7, the variation of double-layer capacitance with radial position is not significant and the capacitance is almost uniform. The presence of supporting electrolyte suppresses the potential gradient and leads to a smaller variation of overpotential over the electrode

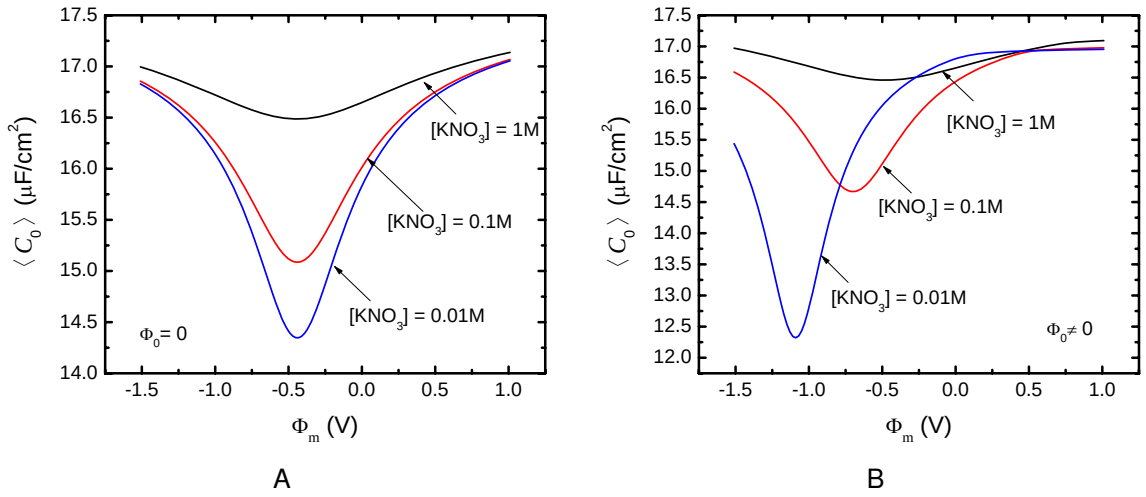

Figure 7-8. Potential dependence of double-layer capacitance for a silver electrode in solution containing 0.1 M $AgNO_3$ and different concentrations of supporting electrolyte when the system is A) at equilibrium and B) not at equilibrium.

surface. Therefore, the assumption of using a uniform double-layer capacitance in systems with excess supporting electrolyte is justified.

To investigate the effect of supporting electrolyte, the reactions of silver deposition and dissolution were considered. For electrolytic solution containing symmetric electrolyte, the capacitance-potential curves are symmetric over Φ_{pzc} when the system is at equilibrium as shown in Figure 7-8A. When the system is not at equilibrium (Figure 7-8B), the minimum value of the double-layer capacitance is observed at a potential more negative to $\Phi_{\mathrm{pzc}} =$ -0.44 V. The double-layer capacitance shows larger dependency on electrode potential when the solution concentration is smaller, indicating the increasing potential gradient in the interfacial region with the decreasing solution conductivity.

Figure 7-9 shows the distributions of double-layer capacitance on a silver electrode in contact with $AgNO_3$ and different concentrations of supporting electrolyte KNO_3. When a small amount of supporting electrolyte is present, the distribution of the double-layer capacitance is more nonuniform. Although the overall variations are still not significant, the absence of supporting electrolyte increases the interfacial potential and leads to a more nonuniform distribution of double-layer capacitance.

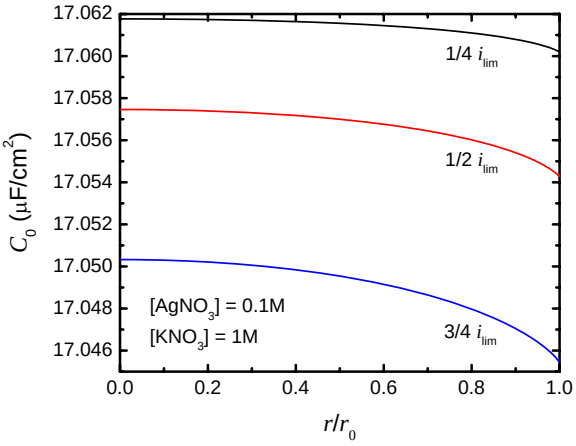

A

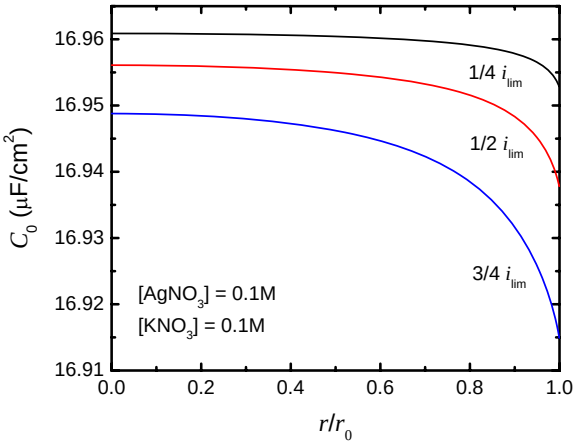

B

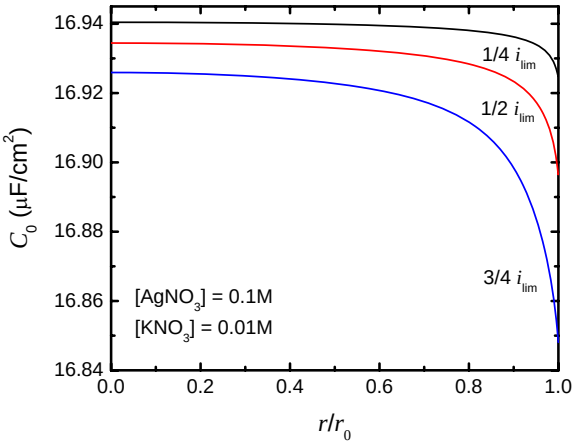

C

Figure 7-9. Radially dependent double-layer capacitance calculated at different fractions of limiting current for silver deposition in solution containing 0.1 M $AgNO_3$ and A) 1 M, B) 0.1 M, and C) 0.01 M KNO_3.

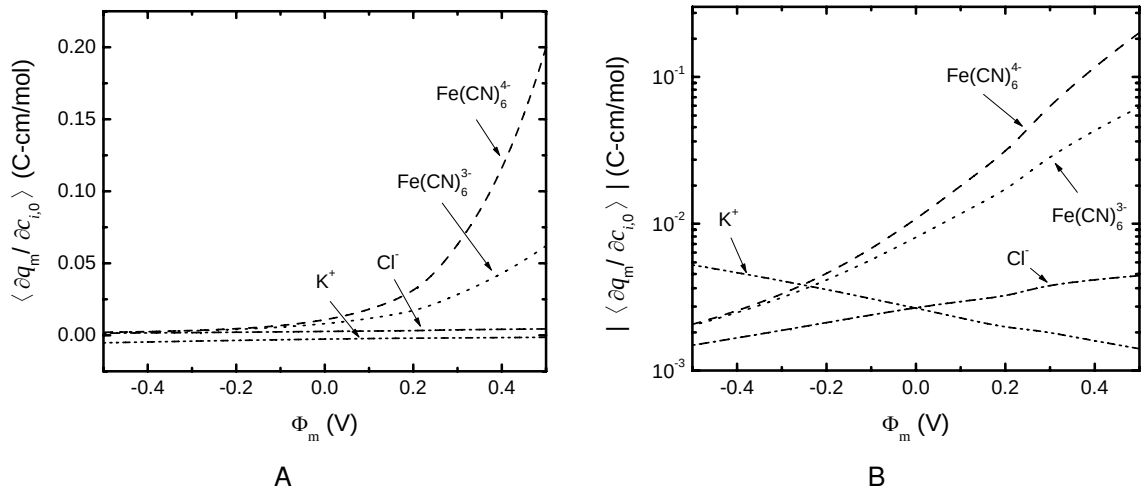

Figure 7-10. Potential dependence of $\partial q_{\mathrm{m}}/\partial c_{i,0}$ in A) linear scale and B) logarithm scale for reduction of ferricyanide and oxidation of ferrocyanide.

7.3.2 Variation of Surface Charge with Concentration

The variation of the surface charge density with the concentration of each species at constant potential shown in (7–13) is expressed by

$$\left(\frac{\partial q_{\mathrm{m}}}{\partial c_{i,0}}\right)_V = \pm \frac{\exp\left(\frac{-z_i F\left(\Phi_{\mathrm{ohp}}-\Phi_0\right)}{RT}\right) - 1}{\left\{\frac{2}{RT\epsilon_{\mathrm{d}}\epsilon_0}\sum_i c_{i,0}\left[\exp\left(\frac{-z_i F\left(\Phi_{\mathrm{ohp}}-\Phi_0\right)}{RT}\right) - 1\right]\right\}^{\frac{1}{2}}} \tag{7–20}$$

The upper sign is used when the potential across the diffuse part of the double layer is larger than the potential of zero charge, *i.e.,* $\Phi_{\mathrm{ohp}} - \Phi_0 > \Phi_{\mathrm{pzc}}$, and, conversely, the lower sign is used when $\Phi_{\mathrm{ohp}} - \Phi_0 < \Phi_{\mathrm{pzc}}$. From equation (7–20), the variation of the surface charge density with ionic concentrations at a fixed potential is only dependent on the charge of each species.

The potential dependence of $\partial q_{\mathrm{m}}/\partial c_{i,0}$ for the system of reduction of ferricyanide and oxidation of ferrocyanide is shown in Figures 7-10. Since the charge associated with ferrocyanide is the largest among all ionic species, the variation of charge on metal surface is highly dependent on the concentration of ferrocyanide. In the system of silver deposition and dissolution, silver ion and potassium ion have the same charge number.

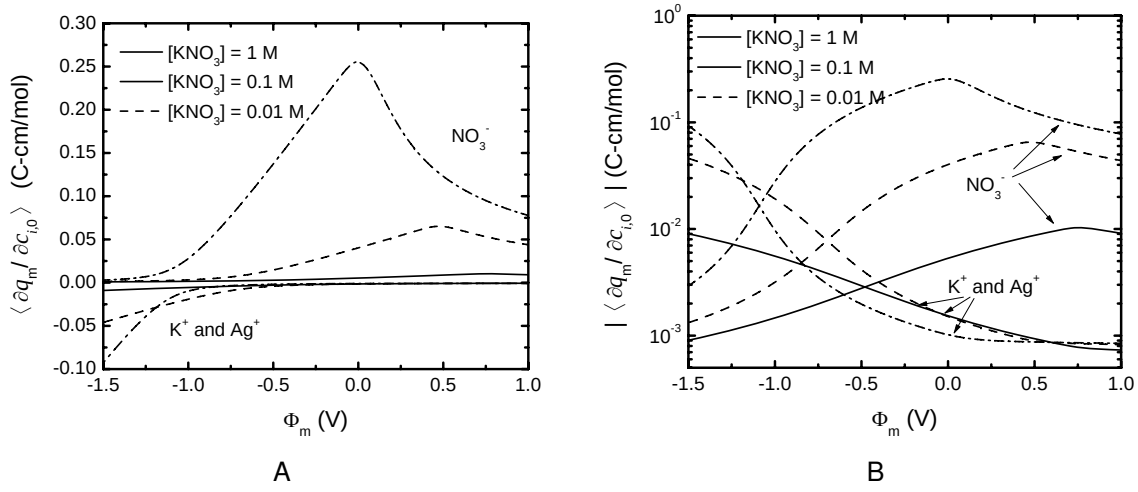

Figure 7-11. Potential dependence of $\partial q_{\mathrm{m}}/\partial c_{i,0}$ in A) linear scale and B) logarithm scale for deposition and dissolution of silver.

Hence the variations of surface charge with the concentrations of these two species are the same as shown in Figure 7-11. The surface charge is highly dependent on the concentration of nitrate, and the value of $\partial q_{\mathrm{m}}/\partial c_{\mathrm{NO_3^-},0}$ increases with decreasing solution concentration. The peak associated with $\partial q_{\mathrm{m}}/\partial c_{\mathrm{NO_3^-},0}$ occurs at electrode potential where the deposition of silver is no longer limited by the mass transfer of silver ion as seen in Figure 7-5.

The radial distributions of $\partial q_{\mathrm{m}}/\partial c_{i,0}$ for reduction of ferricyanide and electrolytic deposition of silver are presented in Figures 7-12 and 7-13, respectively. Similar to the double-layer capacitance, the dependence of $\partial q_{\mathrm{m}}/\partial c_{i,0}$ on radial position is more significant at larger fraction of limiting current and in solution containing small concentration of supporting electrolyte, in which conditions the interfacial potential and the concentration of each species are less uniform.

The charge on the metal surface is shown to have correlation with the potential and the composition of solution adjacent to the electrode surface. The variation of the surface charge density with the concentration of each species, like the double-layer capacitance, is also a property of the electrode-electrolyte interface. The charge

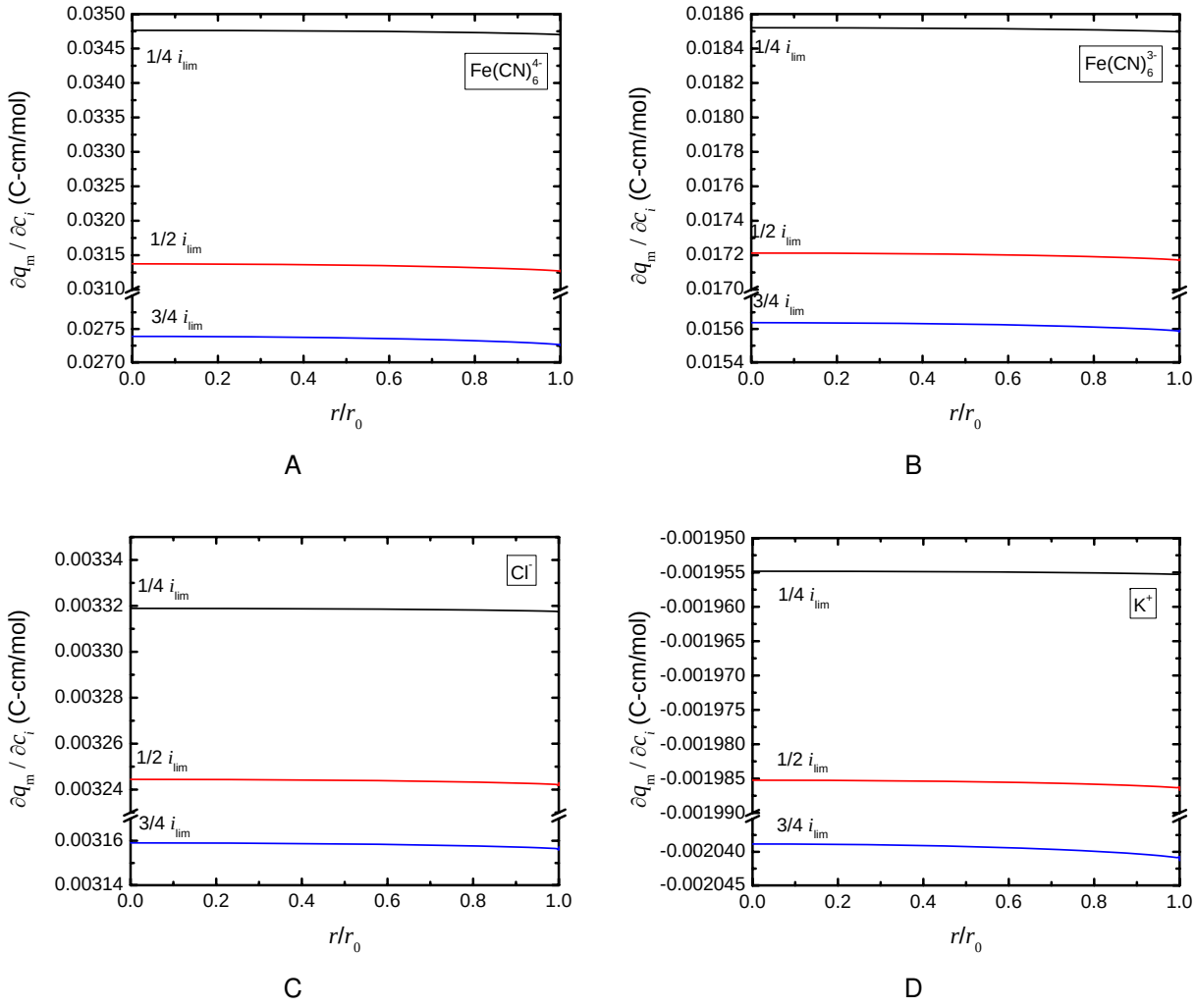

Figure 7-12. Radial distributions of $\partial q_{\mathrm{m}}/\partial c_{i,0}$ for reduction of ferricyanide at different fractions of limiting current for A) ferrocyanide, B) ferricyanide, C) chloride, and D) potassium ions.

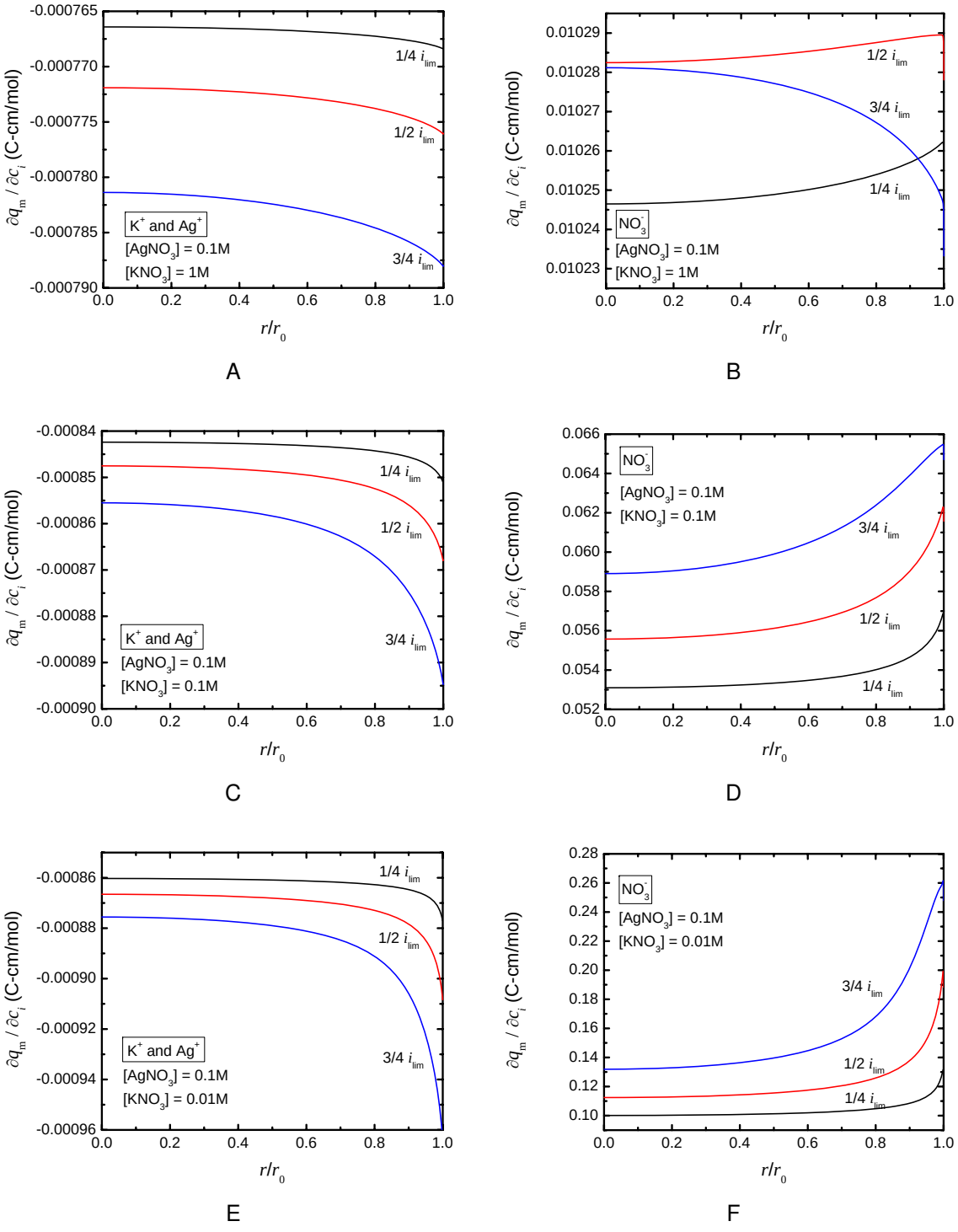

Figure 7-13. Radial distributions of $\partial q_m / \partial c_{i,0}$ for deposition of silver at different fractions of limiting current for A), C), E) potassium and silver ions, and B), D), F) nitrate. The solution contains 0.1 M $AgNO_3$ and A), B) 1 M, C), D) 0.1 M, and E), F) 0.01 M KNO_3.

associated with the mobile species could also be attributed to the double-layer charging and cannot be considered as a negligible quantity. The charing current under transient conditions must account for the contributions of both properties.

7.3.3 Variation of Excess Concentration of Individual Species with Concentration

Another important property of the electrical double layer is the change of excess concentration in the diffuse region of a given species resulting from the variation of its concentration. This property is related to the charge density by

$$\frac{\partial \Gamma_i}{\partial c_{i,0}} = \frac{1}{z_i F} \frac{\partial q_{\mathrm{d},i}}{\partial c_{i,0}} \tag{7–21}$$

which can be used to calculate the contribution of mass flux associated with each species to the charging process. The charge contribution of a given species can be evaluated by numerical integration using equation (7–11). The derivative $\partial q_{\mathrm{d},i}/\partial c_{i,0}$ can further be obtained by numerical differentiation. In the present calculation, the value of $\partial q_{\mathrm{d},i}/\partial c_{i,0}$ was obtained by using five-point central difference.

The potential dependence of $\partial \Gamma_i/\partial c_{i,0}$ of each species for the system of reduction of ferricyanide and oxidation of ferrocyanide is shown in Figure 7-14. The values of all derivatives are zero at the potential of zero charge $\Phi_{\mathrm{pzc}} = 0$. When the electrode is positively charged, the derivative for ferrocyanide has the largest dependency on potential, representing the change of the excess concentration of ferrocyanide in the diffuse region is strongly affected by its concentration at the outer limit of the diffuse region. For the system of silver deposition and dissolution shown in Figure 7-15, the variations of the concentrations of potassium and silver ions have the same effect on their excess concentrations in the diffuse layer. When the system contains a smaller amount of supporting electrolyte, the potential at which the derivative is equal to zero shifts to a value more negative to $\Phi_{\mathrm{pzc}} = -0.44\ V$. The values of derivatives of all species become larger when the system is less conductive, representing a larger variation of the interfacial property with ionic concentrations. The potential at which the

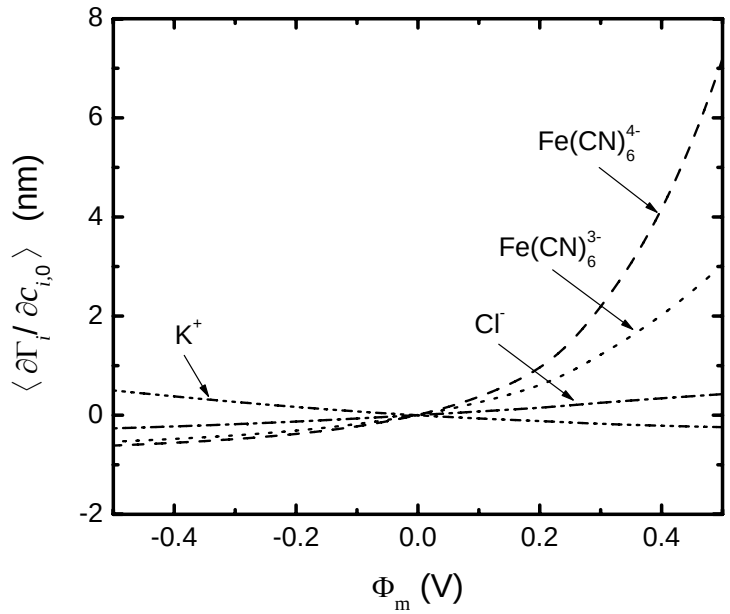

Figure 7-14. Potential dependence of $\partial\Gamma_i/\partial c_{i,0}$ for reduction of ferricyanide and oxidation of ferrocyanide.

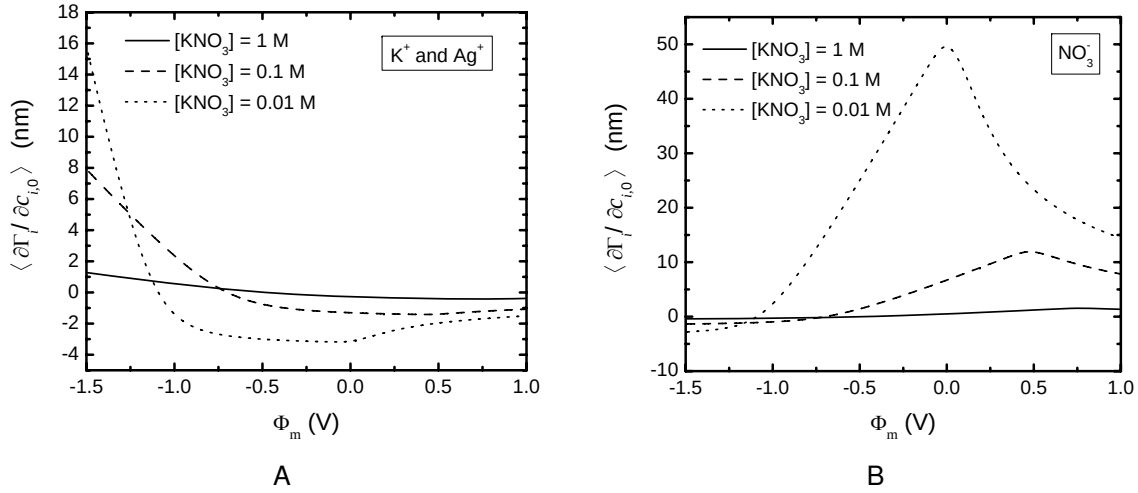

Figure 7-15. Potential dependence of $\partial\Gamma_i/\partial c_{i,0}$ for A) potassium and silver ions, and B) nitrate ion for deposition and dissolution of silver.

peak of the derivative of nitrate is observed is associated with the potential where the deposition of silver is limited by the mass transfer of silver ion.

The distributions of $\partial\Gamma_i/\partial c_{i,0}$ on electrode surface for systems of reduction of ferricyanide and electrolytic deposition of silver are presented in Figures 7-16 and 7-17, respectively. At a larger fraction of limiting current, the radial distributions of $\partial\Gamma_i/\partial c_{i,0}$ for all species are more nonuniform due to the more nonuniform distributions of surface and concentration overpotentials. The decreasing concentration of supporting electrolyte results in more nonuniform distributions of concentrations and potential, and leads to a more nonuniform distribution of the interfacial property.

The interfacial properties discussed in this section are important in describing the thermal behavior of the charged species at the electrode-electrolyte interface. The charging process is related to the changes of potential and concentrations at the interface. The flux of each species, which is associated with the potential and concentration gradients, therefore contributes to the charging process at electrodes. The influence of mass transfer in the charging of the interface is discussed in the following section.

7.4 Coupling of Double-Layer Charging With Mass Transfer

In electrochemical systems, the passage of current through an electrode can be attributed to two processes, Faradaic reactions and double-layer charging. The two processes are usually considered separately for simulations of unsteady-state systems. The flux of reactants and products are given by the rate of the electrode electrochemical reaction. The Faradaic current is usually derived by neglecting the double-layer charging current, which is considered to be an independent process on an ideal polarized electrode. The total current is subsequently obtained by adding the double-layer charging current to the Faradaic current. This assumption was criticized by Delahay[65–67] for the reason that part of the flux of reacting species contributes to the charging of the interface as well as to the Faradaic reaction. Faradic current is not

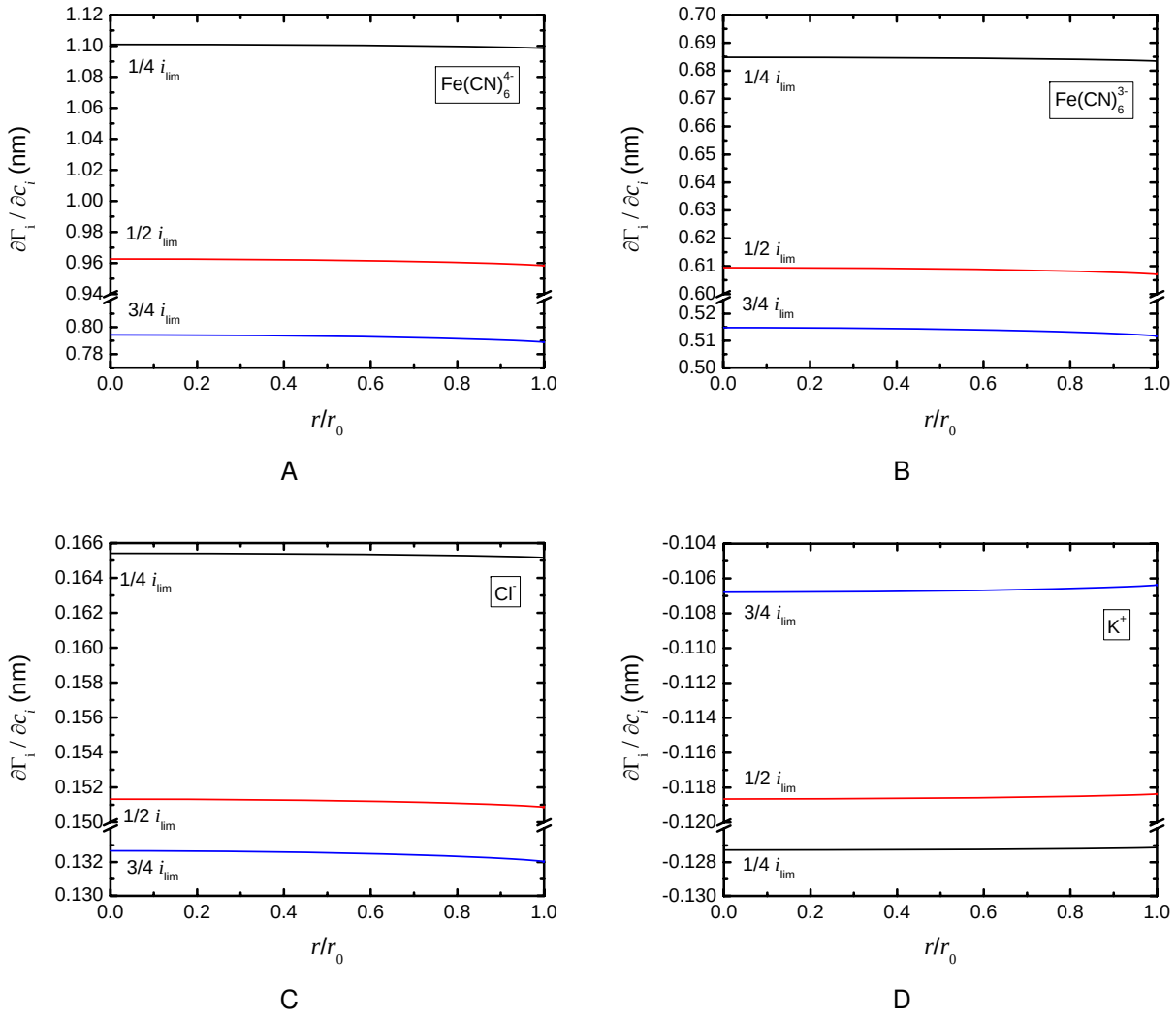

Figure 7-16. Radial distributions of $\partial\Gamma_i/\partial c_{i,0}$ for reduction of ferricyanide at different fractions of limiting current for A) ferrocyanide, B) ferricyanide, C) chloride, and D) potassium ions.

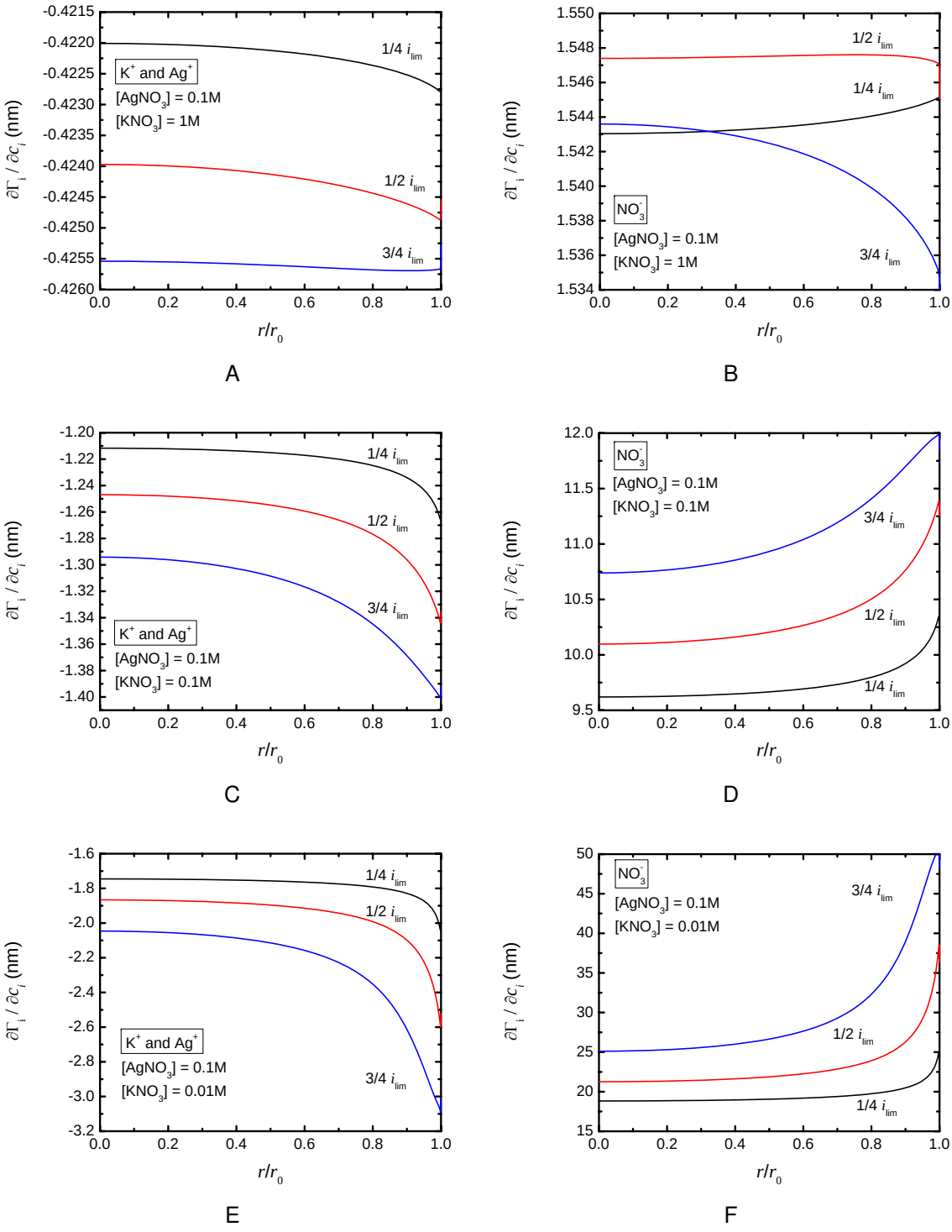

Figure 7-17. Radial distributions of $\partial\Gamma_i/\partial c_{i,0}$ for deposition of silver at different fractions of limiting current for A), C), E) potassium and silver ions, and B), D), F) nitrate. The solution contains 0.1 M $AgNO_3$ and A), B) 1 M, C), D) 0.1 M, and E), F) 0.01 M KNO_3.

a separate measurable quantity. Therefore, the Faradaic current and the double-layer charging current cannot be separated *a priori*.

The measurable total current should include the variation of the excess concentration of each species Γ_i in addition to the contributions of the "usual" double-layer capacitance at the interface. The assessment of Γ_i requires the knowledge of the charge distribution in the diffuse double layer. Grahame[64] and Delahay[62] reviewed the theory and the structure of double layer and its relation to the electrode kinetics.[62] In this dissertation, we use the Gouy-Chapman-Stern model to evaluate the charge density in the diffuse part of the double layer. The double-layer theory was applied to modify the boundary equations for flux and current density.

At the electrode boundary, the surface flux is usually considered to be contributed only from the charge-transfer reactions. The surface flux of each species is related to the Faradaic current by

$$N_{i,0} = -\frac{s_i}{nF} i_{\mathrm{F}} \tag{7–22}$$

This expression is not quite correct because the contribution from the double-layer charging is neglected. Following the derivations by Delahay[65–67] and Nisancioglu,[68,69] the surface flux is corrected with no *a priori* separation (NAPS) of Faradaic and double-layer charging currents by

$$N_{i,0} = -\frac{\partial \Gamma_i}{\partial t} - \frac{s_i}{nF} i_{\mathrm{F}} \tag{7–23}$$

By applying a simple chain rule, the change of surface excess concentration of species i with time can be expressed in terms of the total charge density on metal surface and the concentration of the corresponding species at the outer limit of the diffuse layer by

$$\frac{\partial \Gamma_i}{\partial t} = -\frac{\partial \Gamma_i}{\partial c_{i,0}} \frac{\partial c_{i,0}}{\partial q_{\mathrm{m}}} \frac{\partial q_{\mathrm{m}}}{\partial t} \tag{7–24}$$

The total current flows to the electrode surface is also corrected in the case of NAPS by

$$i = \frac{\partial q_{\mathrm{m}}}{\partial t} + i_{\mathrm{F}} \tag{7–25}$$

Since the surface charge density is a function of potential and concentrations of each species, the time derivative of q_{m} in equations (7–24) and (7–25) can be expressed in terms of the correlating variables following

$$\frac{\partial q_{\mathrm{m}}}{\partial t} = \left(\frac{\partial q_{\mathrm{m}}}{\partial V}\right)_{c_{i,0}} \frac{\partial V}{\partial t} + \sum_{i} \left(\frac{\partial q_{\mathrm{m}}}{\partial c_{i,0}}\right)_{V, c_{j,0, j\neq i}} \frac{\partial c_{i,0}}{\partial t} \tag{7–26}$$

The behavior of the thermodynamic properties were discussed in the previous section. With the use of these properties, the charging process is coupled with mass transfer at electrodes.

The mass flux of each species contributes not only to the Faradaic reactions but also to the charging the double layer. Most impedance models[70–73] neglect the contribution of mass flux to the charging of the interface, and assume a uniform distribution of double-layer capacitance. In the present study, we take into account the contribution of mass transfer to the double-layer charging, and also the radial distribution of charge on electrode surface. The local and global impedance responses associated with the mass-transfer and geometry effects are investigated under the assumption that there is no *a priori* separation of charging and Faradaic currents at electrodes.

CHAPTER 8
INFLUENCE OF MASS TRANSFER ON IMPEDANCE RESPONSE

A two-dimensional impedance model is presented in this chapter to study the effect of nonuniform mass transfer in addition to the electrode geometry on the impedance response. The model also takes into account the contribution of mass transfer to the double-layer charging current. The calculation of the transient response requires the steady-state solutions of concentrations and potential obtained in Chapter 6. The model of electric double layer presented in Chapter 7 is applied to modify the charging process at the electrode-electrolyte interface.

8.1 Mathematical Development of Impedance Model

Electrochemical impedance measures the output signal of current or potential in response to a sinusoidal change of potential or current. For electrochemical reactions dependent on mass transfer, the concentrations of reacting species also exhibit sinusoidal responses corresponding to the input signal. In the frequency domain, the potential and concentrations of each species can be described in terms of steady and time-dependent parts by

$$\Phi = \overline{\Phi} + \mathrm{Re}\{\widetilde{\Phi} e^{j\omega t}\} \tag{8–1}$$

and

$$c_i = \overline{c}_i + \mathrm{Re}\{\widetilde{c}_i e^{j\omega t}\} \tag{8–2}$$

respectively, where the bar notation represents the steady-state component, and the tilde notation represents the oscillating component which is a function of only position. Following the development described in Chapter 6 for nonuniform mass transfer on a RDE, and using the above conventions for potential and concentrations, the mass and charge conservation equations (6–4) and (6–6) become

$$j\omega\widetilde{c}_i + \mathbf{v}\cdot\nabla\widetilde{c}_i = \nabla\cdot\left(D_i\nabla\widetilde{c}_i + z_i u_i F\overline{c}_i\nabla\widetilde{\Phi} + z_i u_i F\widetilde{c}_i\nabla\overline{\Phi}\right) \tag{8–3}$$

and

$$\nabla \cdot \left[F \sum_i z_i \left(-D_i \nabla \widetilde{c}_i - z_i u_i F \overline{c}_i \nabla \widetilde{\Phi} - z_i u_i F \widetilde{c}_i \nabla \overline{\Phi} \right) \right] = 0 \tag{8–4}$$

where the higher order terms such as $\widetilde{c}_i \nabla \widetilde{\Phi}$ are neglected. At the electrode boundary, the flux of each species expressed in equation (6–16) in response to a small perturbation of current or potential becomes

$$\widetilde{N}_i = -D_i \frac{\partial \widetilde{c}_i}{\partial y}\bigg|_{y=0} + z_i u_i F \overline{c}_i \frac{\partial \widetilde{\Phi}}{\partial y}\bigg|_{y=0} + z_i u_i F \widetilde{c}_i \frac{\partial \overline{\Phi}}{\partial y}\bigg|_{y=0} \tag{8–5}$$

The correlation between the flux and the current oscillations at electrode boundary is discussed in two cases where the Faradaic current and the double-layer charging current are considered with *a priori* separation (APS) and without *a priori* separation (NAPS).

8.1.1 No *A Priori* Separation of Faradaic and Charging Currents

In the frequency domain, the surface charge density and the current density, following the same conventions for potential and concentration in equations (8–1) and (8–2), can be expressed by

$$q = \overline{q} + \mathrm{Re}\{\widetilde{q} e^{j\omega t}\} \tag{8–6}$$

and

$$i = \overline{i} + \mathrm{Re}\{\widetilde{i} e^{j\omega t}\} \tag{8–7}$$

respectively. When applying a small perturbation to the system, the current at electrode surface corresponding to equation (7–25) becomes

$$\widetilde{i} = j\omega \widetilde{q}_{\mathrm{m}} + \widetilde{i}_{\mathrm{F}} \tag{8–8}$$

where the oscillations of the surface charge density and the Faradaic current density are approximated by Taylor series expansions about their steady values as

$$\widetilde{q}_{\mathrm{m}} = \left(\frac{\partial \overline{q}_{\mathrm{m}}}{\partial \overline{V}} \right)_{\overline{c}_{i,0}} \widetilde{V} + \sum_i \left(\frac{\partial \overline{q}_{\mathrm{m}}}{\partial \overline{c}_{i,0}} \right)_{\overline{V}, \overline{c}_{j,0, j \neq i}} \widetilde{c}_{i,0} \tag{8–9}$$

and

$$\widetilde{i}_{\mathrm{F}} = \left(\frac{\partial \bar{i}_{\mathrm{F}}}{\partial \overline{V}}\right)_{\bar{c}_{i,0}} \widetilde{V} + \sum_{i} \left(\frac{\partial \bar{i}_{\mathrm{F}}}{\partial \bar{c}_{i,0}}\right)_{\overline{V},\bar{c}_{j,0,j\neq i}} \widetilde{c}_{i,0} \tag{8–10}$$

respectively. The surface flux corresponding to equation (7–23) can also be interpreted in the frequency domain as

$$\widetilde{N}_{i,0} = -\frac{\partial \Gamma_i}{\partial c_{i,0}} \frac{\partial c_{i,0}}{\partial q_{\mathrm{m}}} j\omega \widetilde{q}_{\mathrm{m}} - \frac{s_i}{nF} \widetilde{i}_{\mathrm{F}} \tag{8–11}$$

Equations (8–8) and (8–11) can be applied as the boundary conditions to evaluate the impedance response without the assumption of *a priori* separation of Faradaic and double-layer charging currents.

8.1.2 *A Priori* Separation of Faradaic and Charging Currents

The conventional approach in treating the boundary conditions is to consider the double-layer charging and the Faradaic currents as separable quantities. The total current density is usually expressed by

$$i = i_{\mathrm{C}} + i_{\mathrm{F}} = C_0 \frac{\mathrm{d}V}{\mathrm{d}t} + i_{\mathrm{F}} \tag{8–12}$$

From the oscillation of the double-layer charging current

$$\widetilde{i}_{\mathrm{C}} = j\omega C_0 \widetilde{V} \tag{8–13}$$

and applying equation (7–14), the oscillation of the total current density is expressed by

$$\widetilde{i} = j\omega C_0 \widetilde{V} = j\omega \left(\frac{\partial q_{\mathrm{m}}}{\partial V}\right)_{c_{i,0}} \widetilde{V} + \widetilde{i}_{\mathrm{F}} \tag{8–14}$$

The comparison of equation (8–14) with equations (8–8) and (8–9) shows that the second term in equation (8–9) is neglected. This implies that the contribution of mass flux in charging the double layer is neglected and the Faradaic current and the double-layer charging current are considered separately. Since the change of surface charge density resulting from the concentration variation is neglected, the oscillation of flux

becomes

$$\widetilde{N}_{i,0} = -\frac{s_i}{nF}\widetilde{i}_{\mathrm{F}} \tag{8–15}$$

Under the assumption that there is *a priori* separation of Faradaic and double-layer charging currents, equations (8–14) and (8–15) are used as the boundary conditions to evaluate the transient responses of potential and concentrations.

8.2 Numerical Simulation

The nonlinear equations were solved by using the finite-element package *COMSOL Multiphysics*® with the Nernst-Planck module in a 2D axial symmetric coordinate system. The domain size and the mesh criteria are the same as those used in the steady-state model and were described in Chapter 6. The steady-state solutions of potential and concentrations of all species were used as input functions in the impedance model in the form of lookup tables from which appropriate values can be obtained by interpolation. The use of the same meshed domain in the steady-state and the impedance models reduces the error from interpolation between nodal points. The distributions of the double-layer capacitance and other thermodynamic parameters at electrode boundary were also applied in the impedance model to evaluate the impedance response under the assumption of no *a priori* separation of Faradaic current and double-layer charging current (case NAPS). When *a priori* separation of Faradaic and charging current applies (case APS), a surface averaged double-layer capacitance

$$\langle C_0 \rangle = \frac{1}{\pi r_0^2}\int_0^{r_0} C_0(r) 2\pi r \mathrm{d}r \tag{8–16}$$

was used to determine the charging current which did not include the contribution of mass transfer in the diffuse region of charge.

8.3 Calculated Impedance Responses for Reduction of Ferricyanide

The impedance response for reduction of ferricyanide was calculated in solution with excess supporting electrolyte. Although the distributions of surface charge and double-layer capacitance are almost uniform when the system is in the presence of

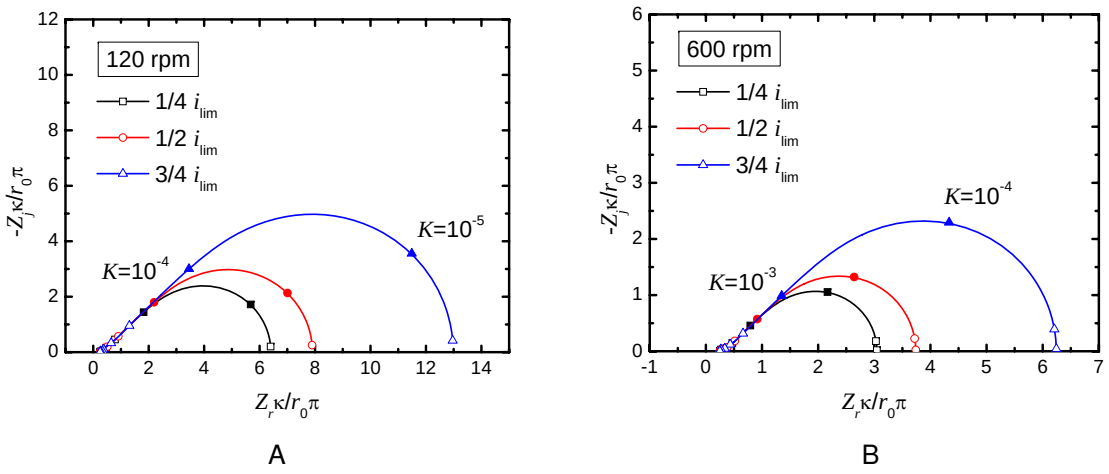

Figure 8-1. Nyquist representation of the global impedance response for reduction of ferricyanide on a rotating disk electrode rotating at A) 120 rpm and B) 600 rpm.

a supporting electrolyte, the calculations still applied the modified electrode process that did not account for the *a priori* separation of Faradaic and double-layer charging currents (case NAPS). The presented impedance values are normalized by electrolyte conductivity and electrode radius. The dimensionless frequency is defined as

$$K = \frac{\omega\langle C_0\rangle r_0}{\kappa} \tag{8–17}$$

in both cases.

8.3.1 Global Impedance

The global impedance calculated at different rotation speeds 120 rpm and 600 rpm are presented in Nyquist format in Figure 8-1A and 8-1B, respectively. The high-frequency loop associated with the charge-transfer reaction is small compared to the low-frequency loop associated with mass transfer, representing a reaction of fast kinetics and controlled by mass transfer of reacting species to electrode. Different rotation speeds should only have an effect at low frequencies. The smaller low-frequency loop and larger characteristic frequency in Figure 8-1B indicate a smaller mass-transfer resistance at a higher rotation speed. The comparison of the global impedance by assuming

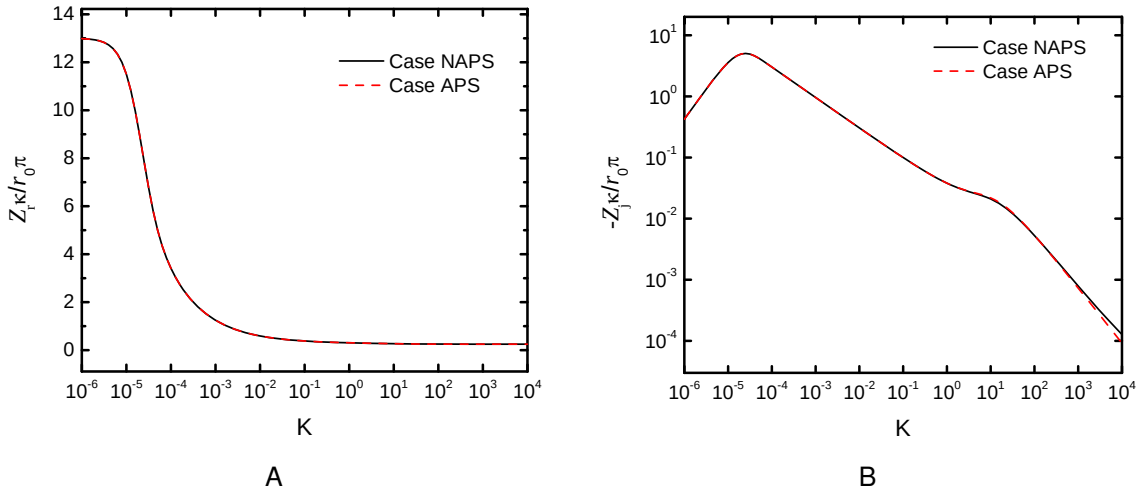

Figure 8-2. Real and imaginary components of the global impedance response for reduction of ferricyanide at three-fourths of limiting current on a rotating disk electrode rotating at 120 rpm.

a priori and no *a priori* separation of Faradaic and double-layer charging currents is shown in Figure 8-2 for the real and imaginary components as a function of frequency. In the presence of an excess supporting electrolyte, the contribution of mass flux to the charging current does not affect the impedance response significantly.

The global impedance is an average representation for the local impedances. The local impedances, however, do not always behave the same as the global response.

8.3.2 Local Impedance

The Nyquist representation of the local impedances are shown in Figure 8-3 with radial position as a parameter. The local impedance has a larger value at electrode center and a smaller value near the edge of the disk, representing a greater accessibility near the electrode periphery. Inductive loops are observed at high frequencies, which is due to the nonuniform current and potential distributions associated with the electrode geometry.

8.3.3 Local Interfacial Impedance

The Nyquist representation of the local interfacial impedances are shown in Figure 8-4 with radial position as a parameter. Interfacial impedance represents the

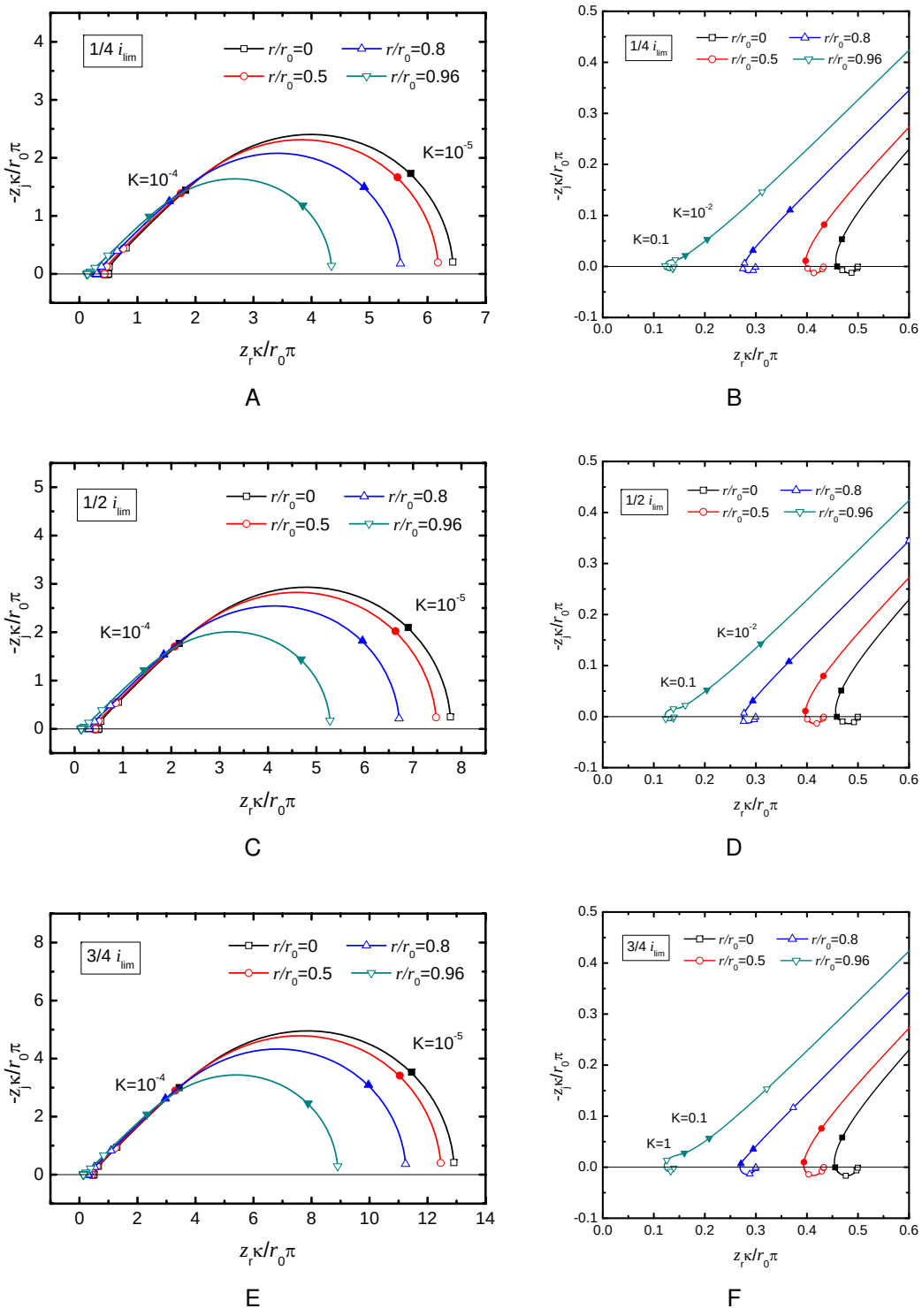

Figure 8-3. Nyquist representation of the local impedance for reduction of ferricyanide on a rotating disk electrode rotating at 120 rpm calculated at A), B) one-fourth, C), D) one-half, and E), F) three-fourths of limiting current. The enlargements of the high-frequency inductive loops are shown in (B),(D), and (E).

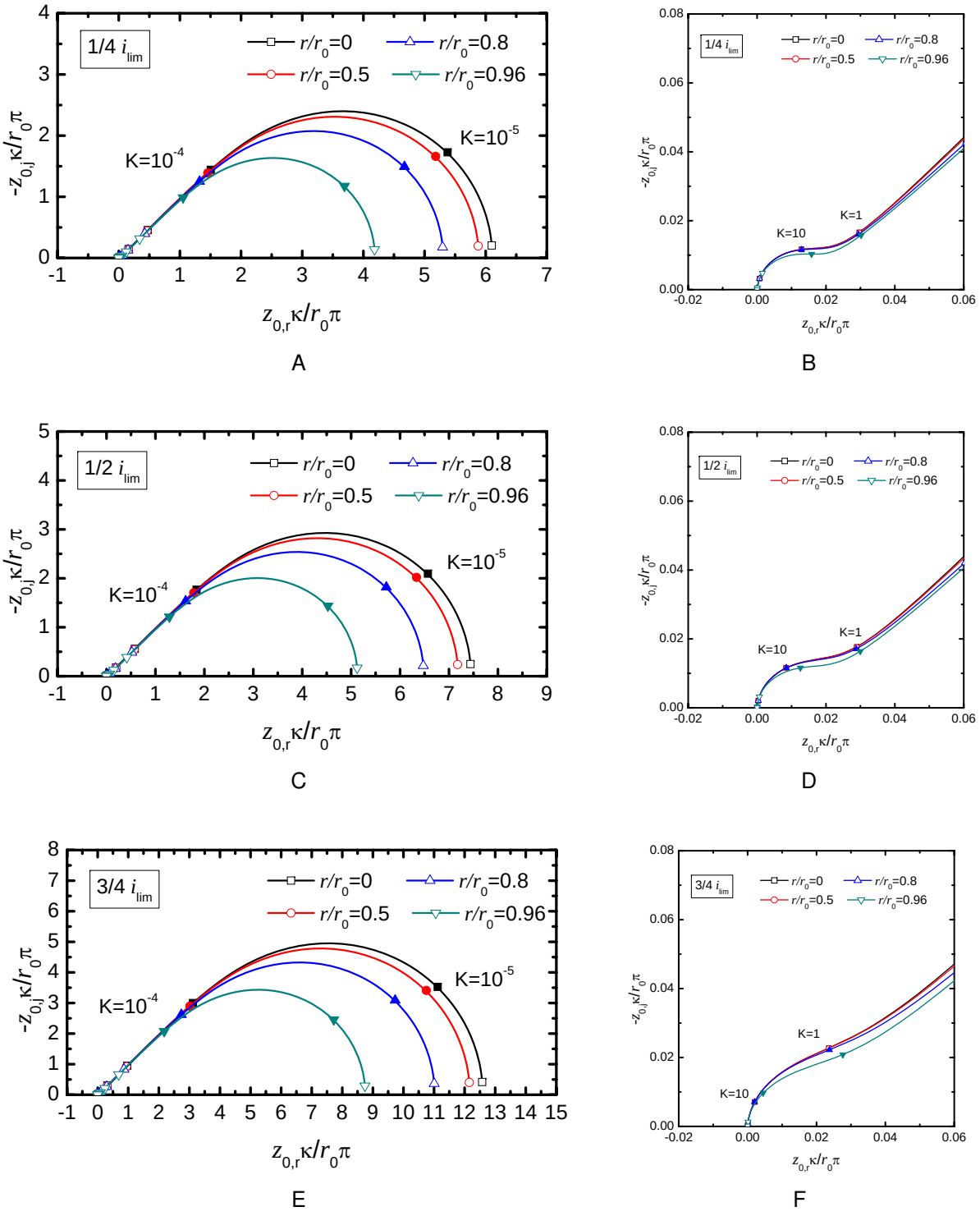

Figure 8-4. Nyquist representation of the local interfacial impedance for reduction of ferricyanide on a rotating disk electrode rotating at 120 rpm calculated at A), B) one-fourth, C), D) one-half, and E), F) three-fourths of limiting current. The enlargements of the high-frequency inductive loops are shown in (B),(D), and (E).

transient response of electric properties in the interfacial region. The high-frequency loop is associated with the charge-transfer reaction and the charging of the interface. Since the radial distributions of double-layer capacitance and other thermodynamic parameters are almost uniform on electrode surface in the presences of an excess supporting electrolyte, the dispersion of local interfacial impedance is not significant at high frequencies.

8.3.4 Local Ohmic Impedance

The Nyquist plots for the local Ohmic impedance are presented in Figure 8-5 as radial position as a parameter. The resistance of electrolyte exhibiting complex features is in agreement with the previous studies.[2,3,10–12,14,22] The local Ohmic impedance shows only inductive behavior near the electrode center, and shows both inductive and capacitive behavior at electrode periphery. The dependence of the complex values of the local Ohmic impedance with frequency is given in Figure 8-6 Complex values are observed in the whole frequency range. At the same rotation speed, the high-frequency complex values become larger when electrode reaction rate is larger. The low-frequency complex values, however, do not affected by the electrode reaction and remain the same when the disk rotation speed is fixed. With increasing rotation speed, the complex values at low frequencies are diminished and become almost zero when the rotation speed is up to 2,400 rpm. On the other hand, the complex values at high frequencies do no vary with rotation speed. These results demonstrate that the high-frequency complex behavior of the local Ohmic impedance is associated with the nonuniform Ohmic potential drop in solution, which is more significant when the electrode kinetics are fast. The low-frequency complex behavior is associated with the nonuniform mass transfer of reacting species to electrode which correlates with the disk rotation speed.

8.4 Calculated Impedance Responses for Deposition of Silver

The global and local impedance responses of the deposition of silver were calculated with different treatments of the boundary conditions (case APS and case NAPS)

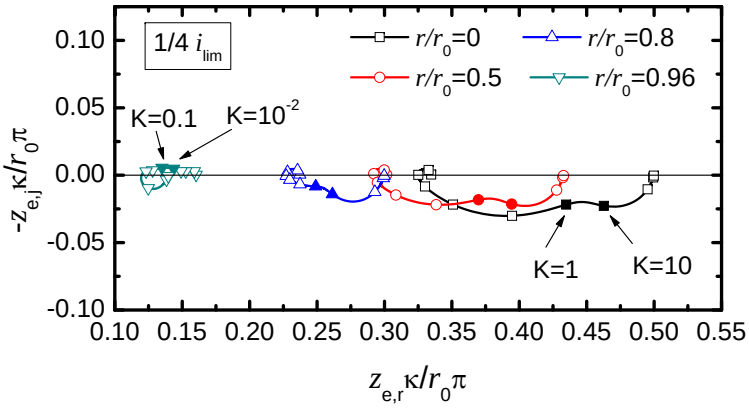

A

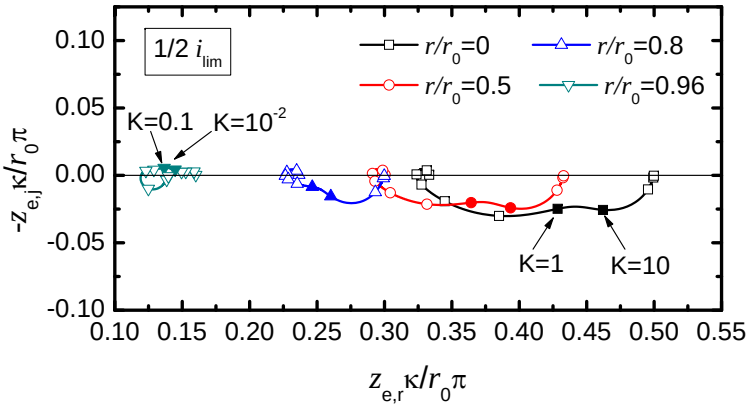

B

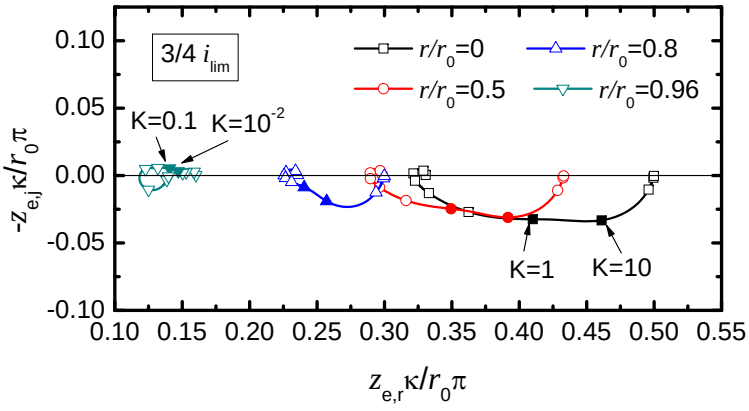

C

Figure 8-5. Nyquist representation of the local Ohmic impedance for reduction of ferricyanide on a rotating disk electrode rotating at 120 rpm and at A) one-fourth, B) one-half, and C) three-fourths of limiting current.

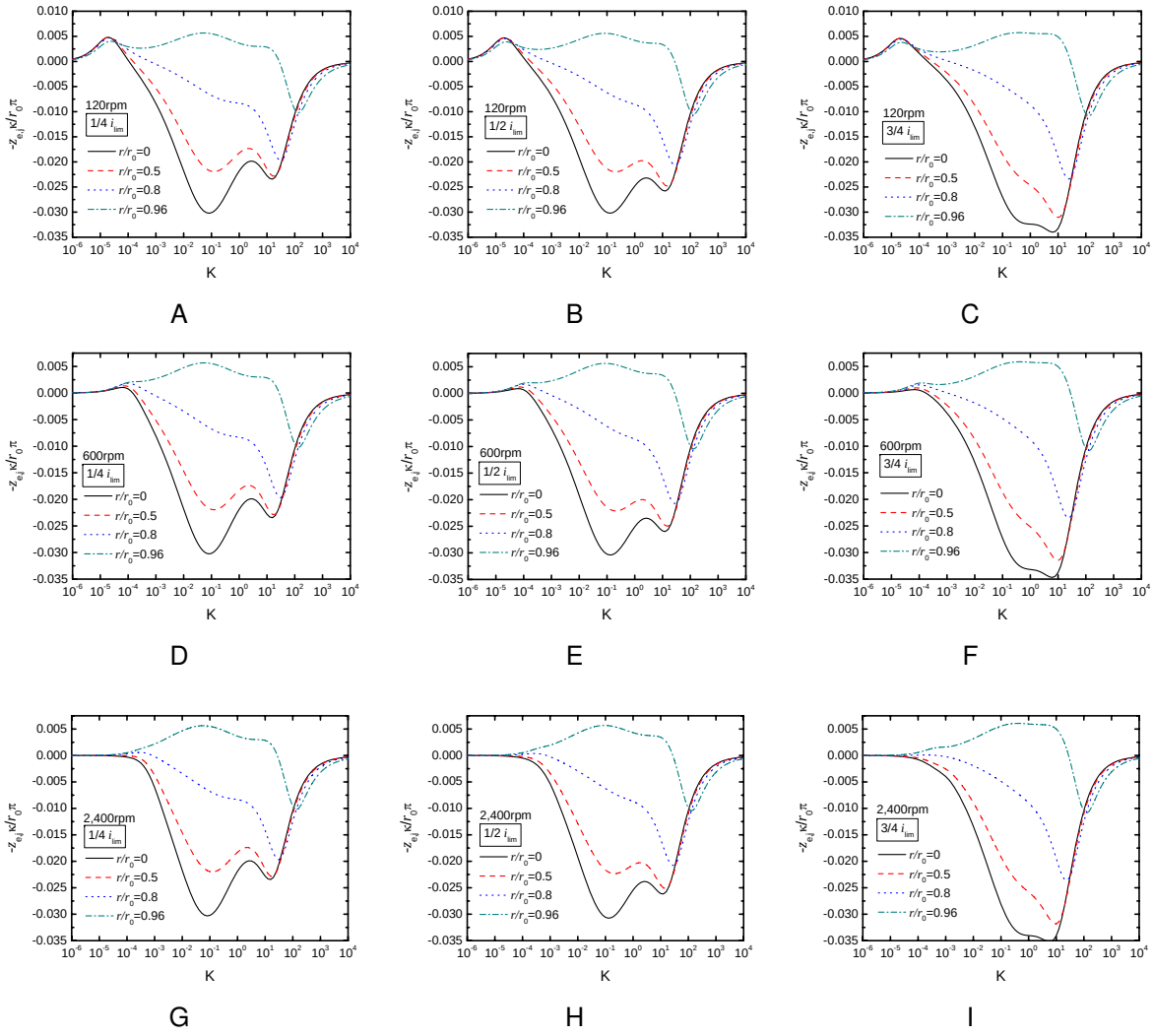

Figure 8-6. Imaginary components of the local Ohmic impedance for reduction of ferricyanide on a rotating disk electrode rotating at A), B), C) 120 rpm, D), E), F) 600 rpm, and G), H), I) 2,400 rpm.

and in different concentrations of supporting electrolyte. The presented impedance values are normalized by electrolyte conductivity and electrode radius. The frequency is normalized by electrolyte conductivity, electrode radius, and double-layer capacitance as defined in equation (8–17).

8.4.1 Global Impedance

The calculated global impedances for silver deposition in different concentrations of supporting electrolyte are shown in Figure 8-7. The influence of electrode process with and without *a priori* separation of Faradaic and double-layer charging currents on the global impedance is observed at high frequencies where the charging process is important. The depressed semicircles observed at high frequencies in cases APS and NAPS is due to the geometry induced current and potential distributions, and could also be due to the distributions of interfacial properties such as double-layer capacitance and other thermodynamic properties discussed in Chapter 7. In Figure 8-7B for a small amount of supporting electrolyte present in the system, the high-frequency loop shows a distortion in the case of NAPS. The discrepancies of impedance values between cases APS and NAPS can be observed more clearly in the representation of the real and imaginary components as a function of frequency give in Figure 8-8. The characteristic frequency of a given electrode process corresponds to the frequency where the imaginary component of the impedance has a maximum value. In Figure 8-8D, a larger characteristic frequency corresponding to the charging process is observed in case NAPS. The discrepancies in the value of characteristic frequency could be due to the extra contribution of flux in charging the double layer. The values of effective capacitance for different electrolytic systems are estimated and will be discussed at the end of this chapter.

The Ohmic resistance can be obtained from the high-frequency limit of the global impedance. The dimensionless Ohmic resistance obtained in the impedance model has a value of 0.249 at zero current. This value is different from 0.25, which was given

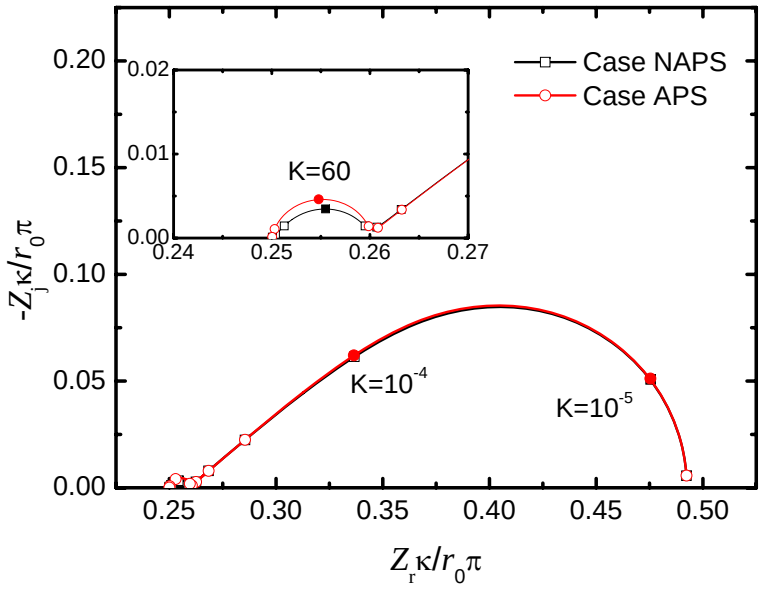

A

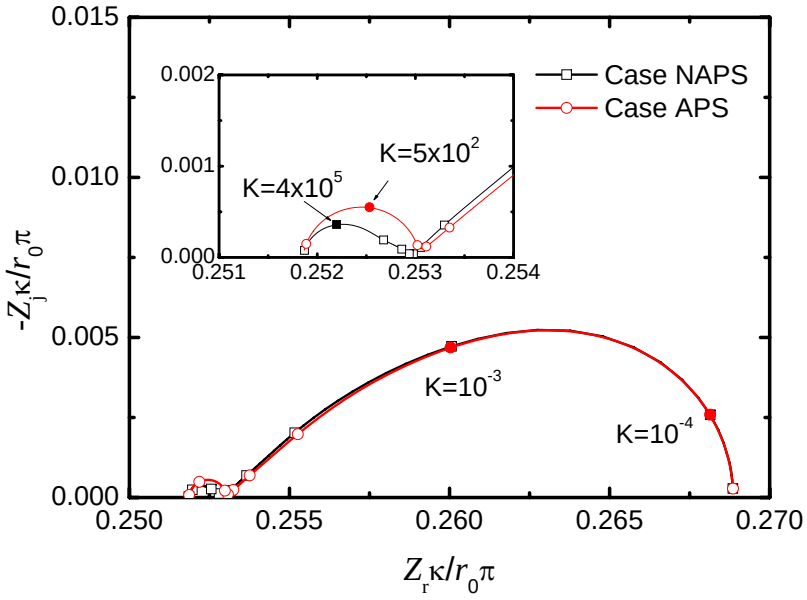

B

Figure 8-7. Nyquist representation of the global impedance response for deposition of silver at one-fourth of limiting current on a rotating disk electrode rotating at 120 rpm. The solution consists of 0.1 M $AgNO_3$ and A) 1 M and B) 0.01 M KNO_3 as a supporting electrolyte.

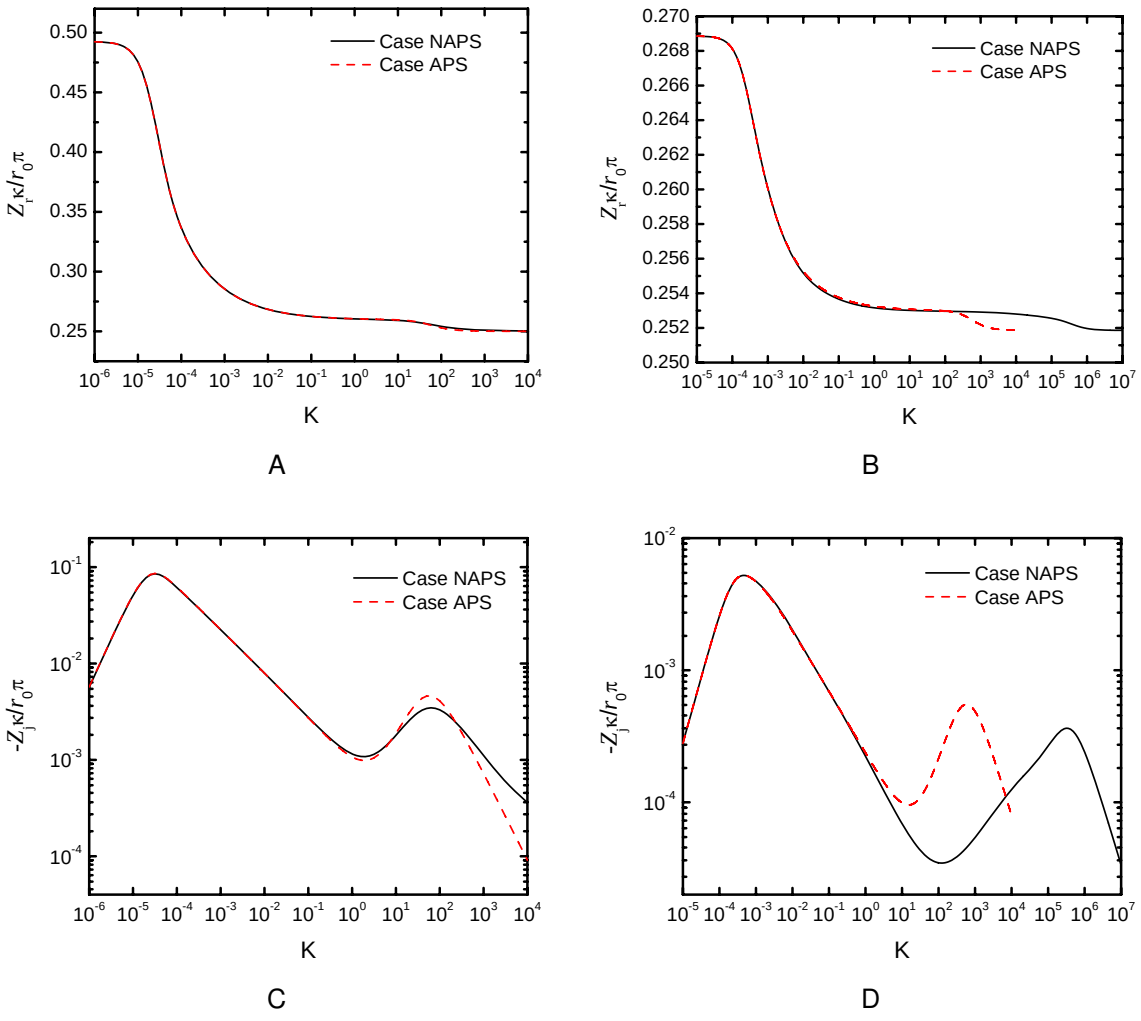

Figure 8-8. Calculated real and imaginary components of the global impedance response as a function of frequency for deposition of silver at one-fourth of limiting current on a rotating disk electrode rotating at 120 rpm: A) real part for 1 M KNO_3, B) real part for 0.01 M KNO_3, C) imaginary part for 1 M KNO_3, and D) imaginary part for 0.01 M KNO_3.

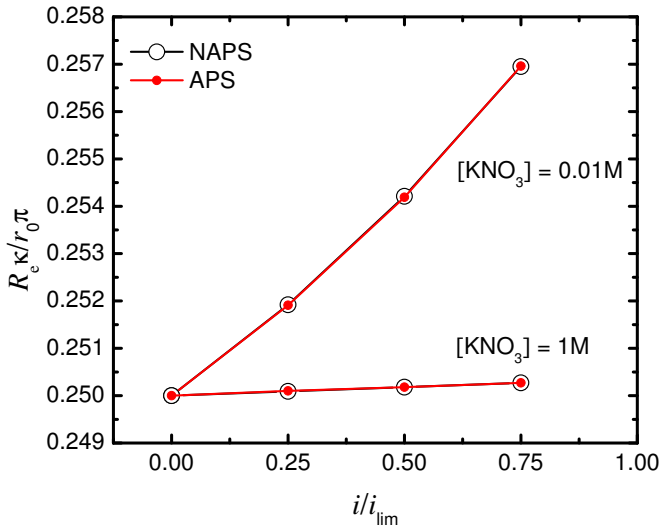

Figure 8-9. Normalized Ohmic resistance of electrolytic solution consisting of $AgNO_3$ and KNO_3 as a function of silver deposition rate.

by Newman[5] for the Ohmic resistance on a disk electrode with the counter electrode placed at infinity. The error in assessing the values of Ohmic resistance by using a finite domain was considered to be the same when there is current flowing in the system. Figure 8-9 shows the Ohmic resistances at different fractions of limiting current. The Ohmic resistances obtained at different fractions of limiting current were corrected by adding a given value that makes the Ohmic resistance to be 0.25 at zero current. The values of Ohmic resistance are not affected by the assumption that there is *a priori* or no *a priori* separation of Faradaic and double-layer charging currents, but are related to the solution composition and electrode reaction rate. When the ionic concentration is larger, the conductivity of solution is larger, and therefore the Ohmic resistance has a smaller value. The increasing Ohmic resistance with increasing reaction rate is a consequence of change of solution composition at the electrode-electrolyte interface. Figure 8-10 shows the axial distribution of solution conductivity in the diffusion layer for silver deposition at the electrode center. At a larger fraction of limiting current, silver

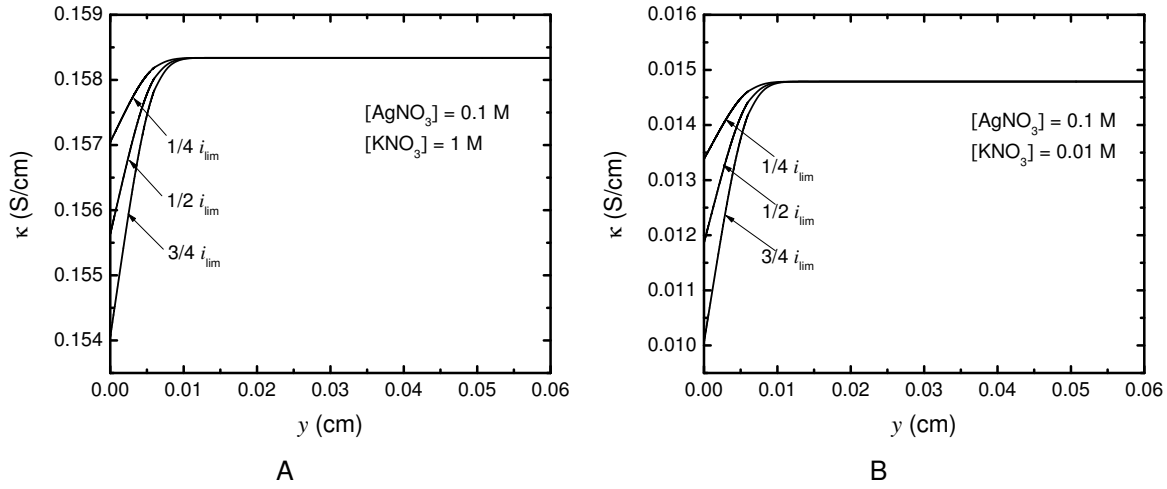

Figure 8-10. Axial distribution of solution conductivity at electrode center for deposition of silver. The electrolytic solution consists of 0.1 M $AgNO_3$ and A) 1 M and B) 0.01 M KNO_3.

ions are kept consuming and depleting at the electrode surface, resulting a smaller conductivity and larger resistance at the interface.

The effective conductivity in the interfacial region can be estimated from the Ohmic impedance that is obtained from the high-frequency limit of the global impedance by

$$\kappa_{\text{eff}} = \frac{\pi}{4}\frac{r_0}{Z_r(\omega \to \infty)} \tag{8–18}$$

Figure 8-11. shows the effective conductivity at the interface normalized by the conductivity in the bulk solution. The conductivity at the interface is equal to the value of bulk solution at zero current. The presence of an excess supporting electrolyte reduces the electric field in the diffusion layer, and the Ohmic resistance and the effective conductivity show a weaker dependency on reaction rate.

8.4.2 Local Interfacial Impedance

The calculated local interfacial impedances for the case NAPS are presented in Figures 8-12 and 8-13 for 1 M and 0.01 M KNO_3, respectively. At one-fourth of limiting current, the interfacial impedances have larger values at electrode center and smaller

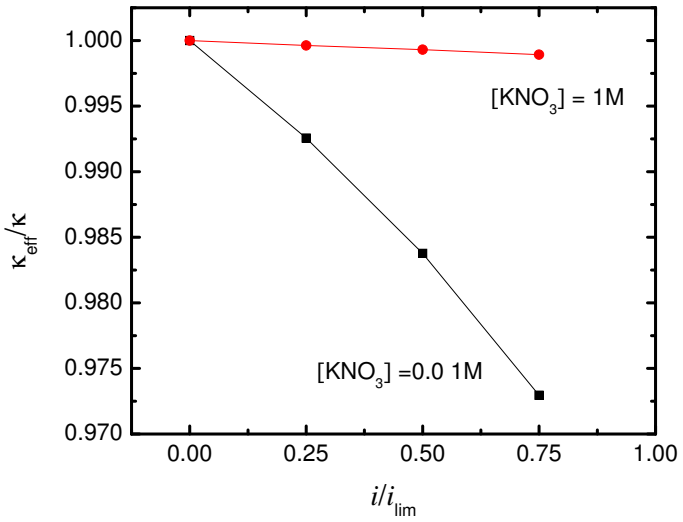

Figure 8-11. Normalized effective conductivity at the interface as a function of silver deposition rate.

values at electrode periphery, showing a larger reaction rate and a greater accessibility at the edge of electrode due to the disk geometry. The increasing overpotential enhances the reaction rate and reduces the concentration of reactant towards the electrode periphery. The local interfacial impedance at the electrode periphery can be increased due to the increasing resistance of the mass transfer of reacting species to the electrode surface. The distribution of the local interfacial impedance at large electrode potentials is therefore influenced by the coupled effect of electrode geometry and mass transfer as seen in Figures 8-12 and 8-13 at one-half and three-fourths of limiting current, respectively. The anomalously large interfacial impedance observed at the electrode periphery shown in Figure 8-13C is needed to be confirmed that it is not a numerical artifact.

The interfacial impedances at high frequencies and at the center of the electrode are given in Figure 8-14. A depressed semicircle is observed in case NAPS even in the presence of an excess supporting electrolyte as shown in Figure 8-14A. The appearance of the depressed semicircle in the local interfacial impedance cannot

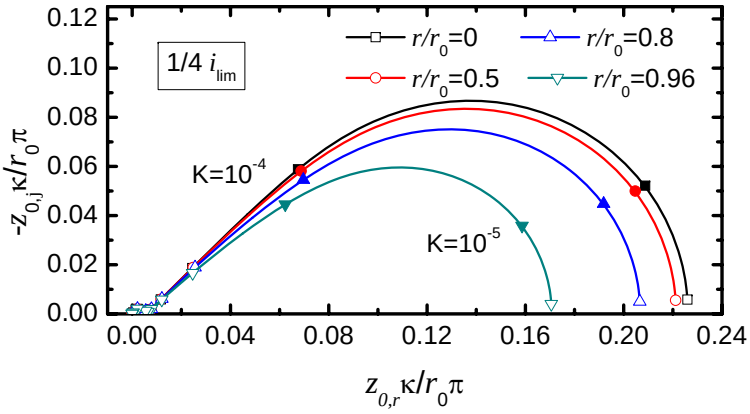

A

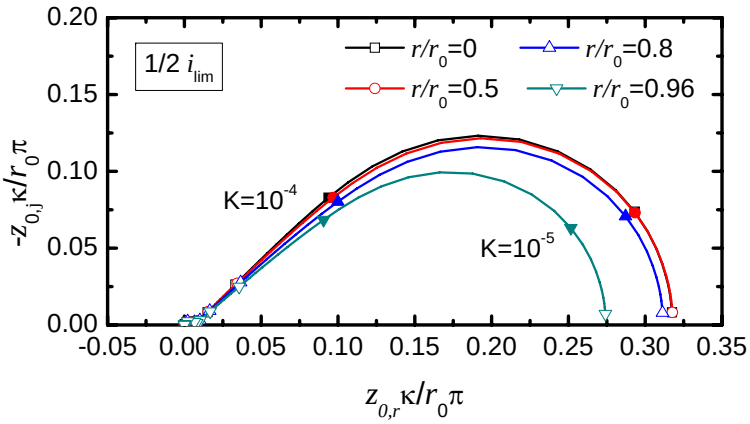

B

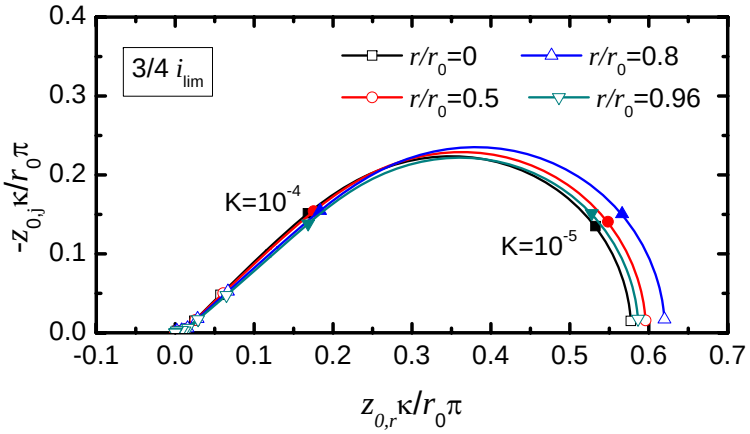

C

Figure 8-12. Nyquist representation of the local interfacial impedance for deposition of silver on a rotating disk electrode rotating at 120 rpm calculated at A) one-fourth, B) one-half, and C) three-fourths of limiting current. The electrolytic solution consists of 0.1 M $AgNO_3$ and 1 M KNO_3.

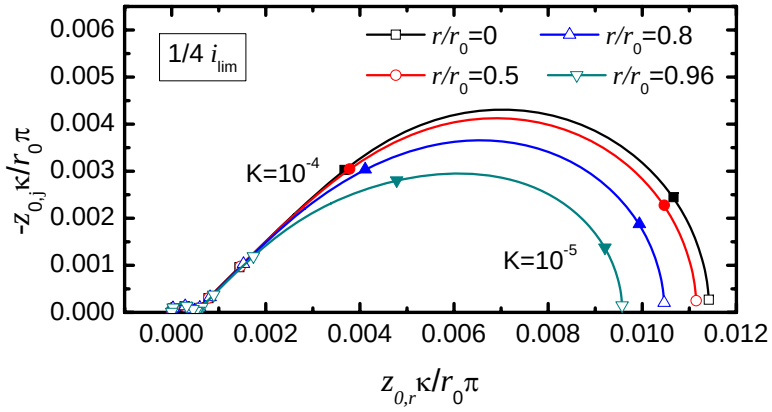

A

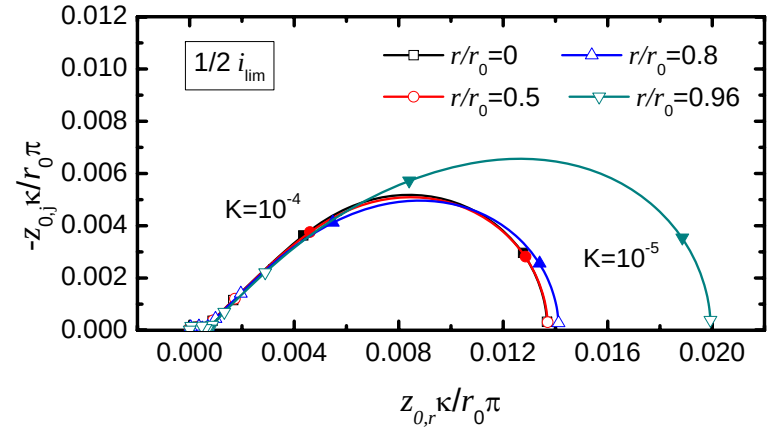

B

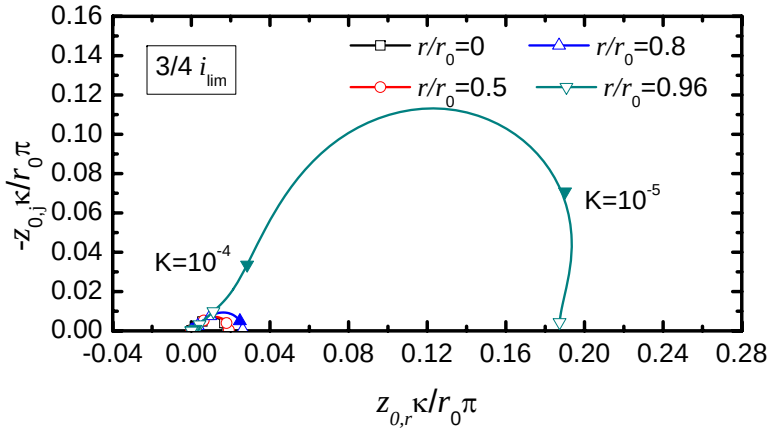

C

Figure 8-13. Nyquist representation of the local interfacial impedance for deposition of silver on a rotating disk electrode rotating at 120 rpm calculated at A) one-fourth, B) one-half, and C) three-fourths of limiting current. The electrolytic solution consists of 0.1 M $AgNO_3$ and 0.01 M KNO_3.

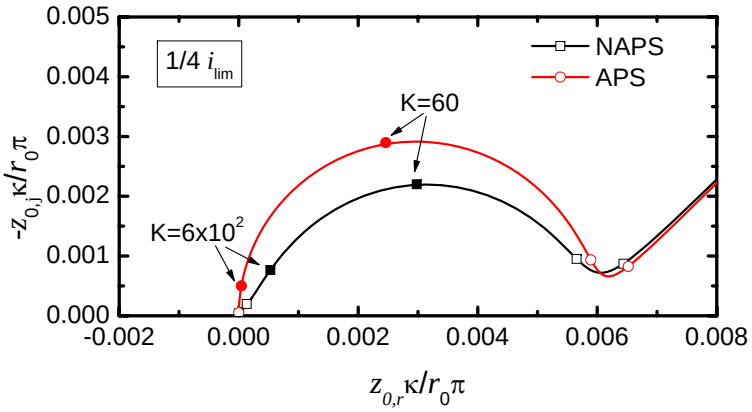

A

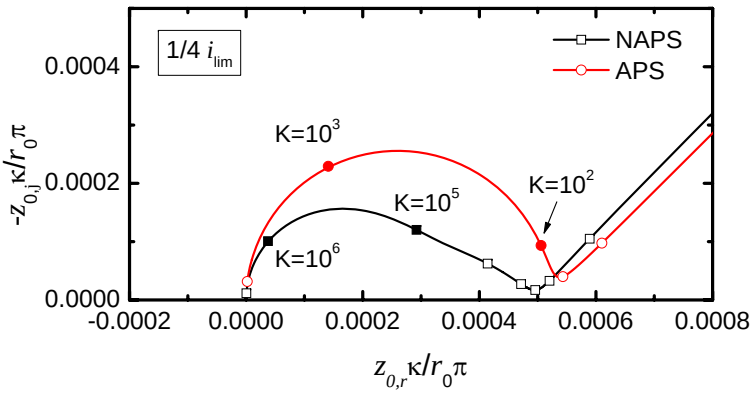

B

Figure 8-14. Nyquist representation of the interfacial impedance at electrode center for deposition of silver at one-fourth of limiting current on a rotating disk electrode rotating at 120 rpm. The solution consists of 0.1 M $AgNO_3$ and A) 1 M and B) 0.01 M KNO_3 as a supporting electrolyte.

be attributed to the geometry-induced current and potential distributions and the distributions of interfacial property. When the concentration of supporting electrolyte is small, the characteristic frequency is larger in case NAPS as shown in Figure 8-14B. The depressed semicircle and the larger value of characteristic frequency observed in case NAPS could be due to the contribution of flux in the charging of the interface, and will be discussed later in this chapter.

8.4.3 Local Ohmic Impedance

Nyquist representations of the local Ohmic impedance for the case of NAPS are presented in Figures 8-15 and 8-16 for 1 M and 0.01 M KNO_3, respectively. Inductive loops are observed at all positions on the electrode and capacitive loop is observed near the disk periphery. The imaginary component of the local Ohmic impedance is given Figure 8-17. While the high-frequency complex behavior is associated with the nonuniform Ohmic potential drop in the electrolyte, the complex behavior observed at low frequencies is attributed to the nonuniform mass transfer to electrode surface. In the presence of an excess supporting electrolyte, the local Ohmic impedance in the system of silver deposition is similar to that observed in the system of reduction of ferricyanide that the local-frequency complex values do not affected by the electrode reaction rate. In solution containing small amount of supporting electrolyte, the low-frequency complex values, however, are strongly dependent on the electrode reaction rate. The anomalously large Ohmic impedance at the periphery is needed to be confirmed that it is not a numerical artifact.

8.4.4 Local Impedance

Nyquist representations of the local impedance for the case of NAPS are presented in Figure 8-18 for 1 M KNO_3. The calculated local impedances show inductive behavior at high frequencies. The high-frequency inductive loops were not observed in the local interfacial impedances and must be attributed to the local Ohmic impedances. For the local impedances in the system in absence of supporting electrolyte as given in Figure

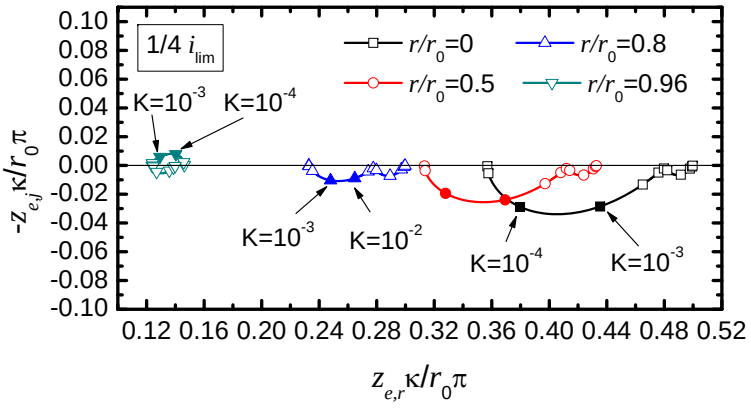

A

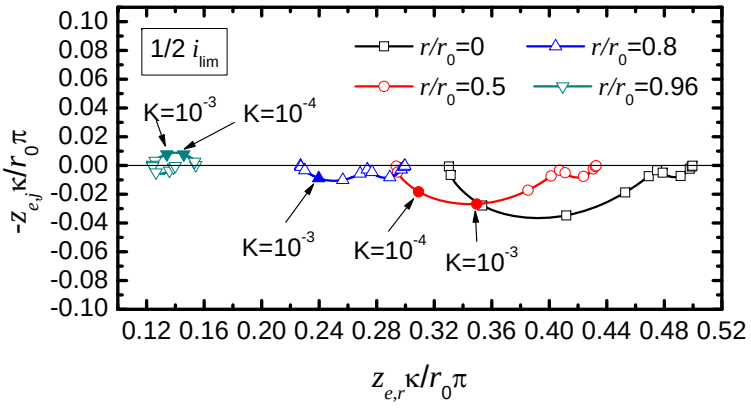

B

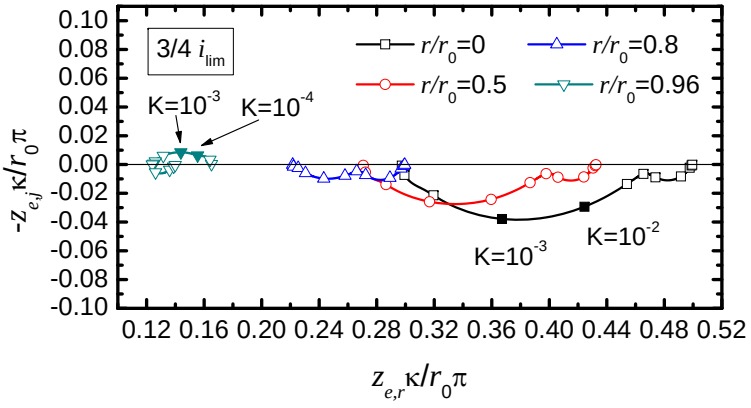

C

Figure 8-15. Nyquist representation of the local Ohmic impedance for deposition of silver on a rotating disk electrode rotating at 120 rpm calculated at A) one-fourth, B) one-half, and C) three-fourths of limiting current. The electrolytic solution consists of 0.1 M AgNO3 and 1 M KNO_3.

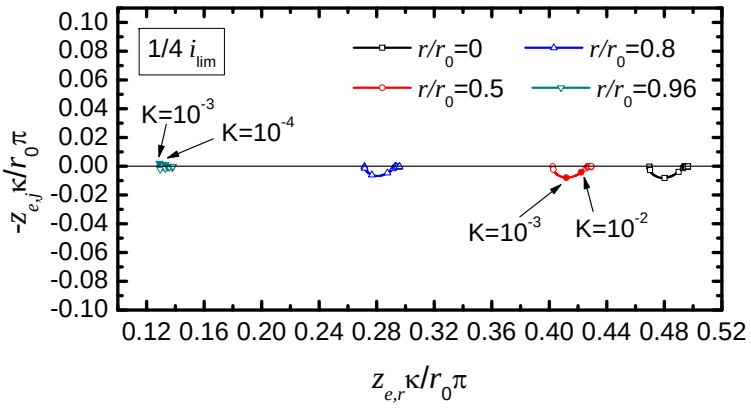

A

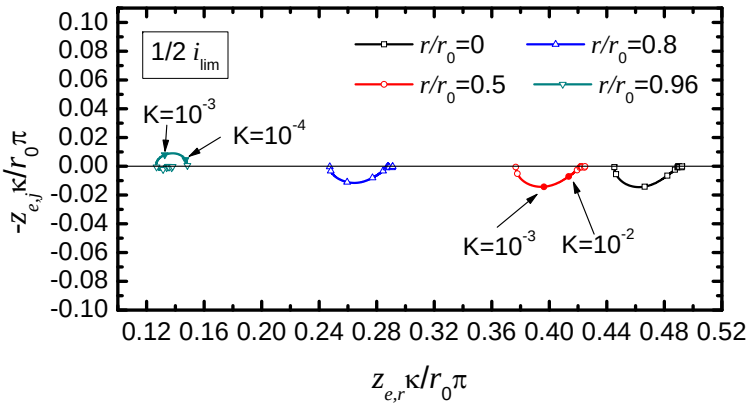

B

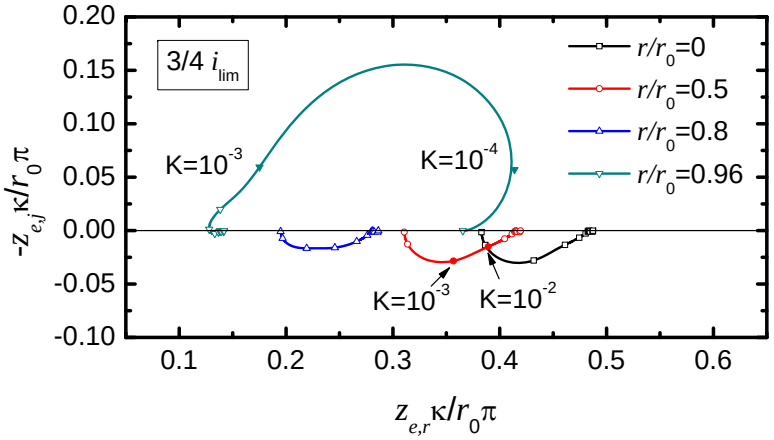

C

Figure 8-16. Nyquist representation of the local Ohmic impedance for deposition of silver on a rotating disk electrode rotating at 120 rpm calculated at A) one-fourth, B) one-half, and C) three-fourths of limiting current. The electrolytic solution consists of 0.1 M $AgNO_3$ and 0.01 M KNO_3.

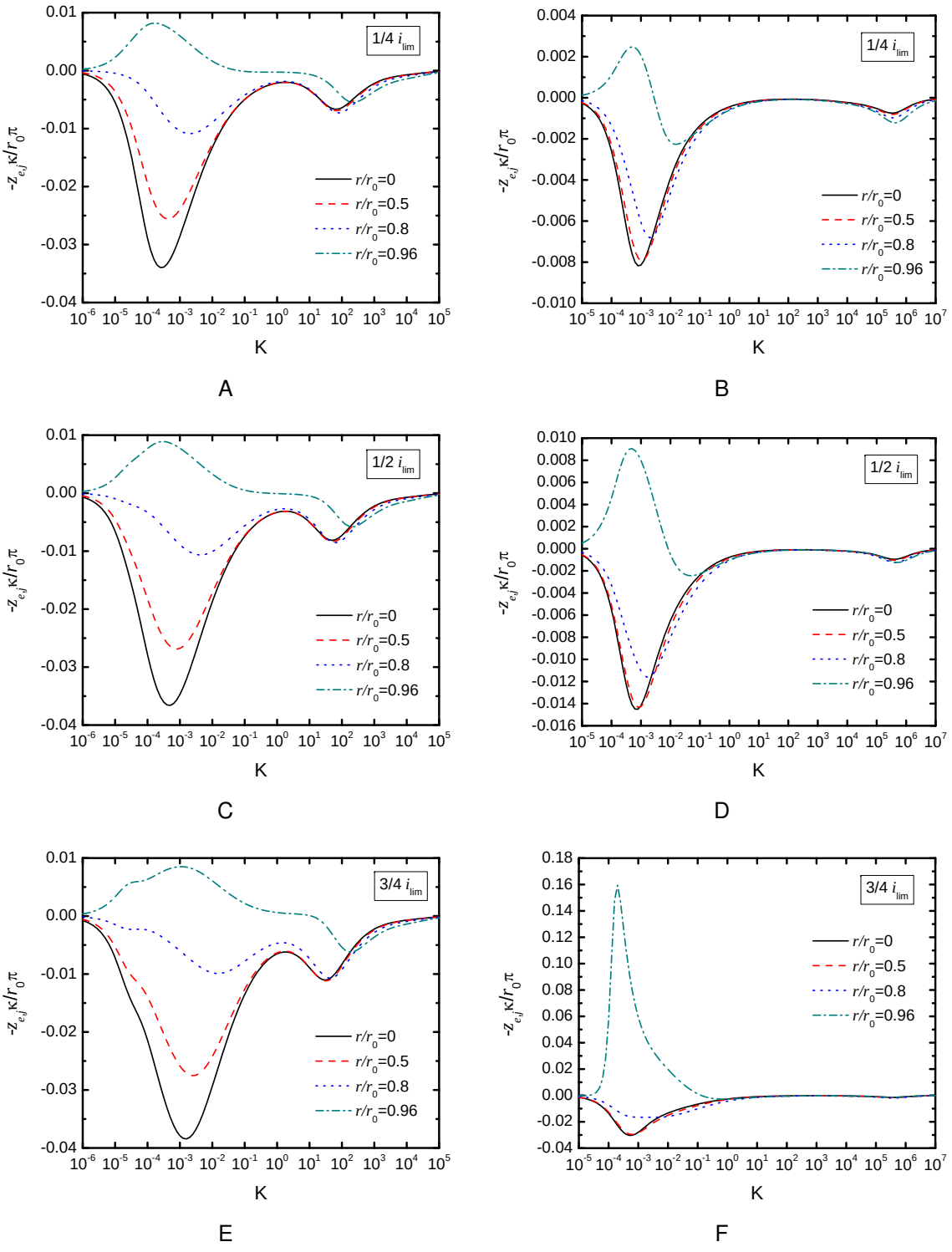

Figure 8-17. Imaginary components of the local Ohmic impedance for deposition of silver on a rotating disk electrode rotating at 120 rpm calculated at A), B) one-fourth, C), D) one-half, and E), F) three-fourths of limiting current. The solution consists of 0.1 M $AgNO3$ and A), C), E) 1 M and B), D), F) 0.01 M KNO_3.

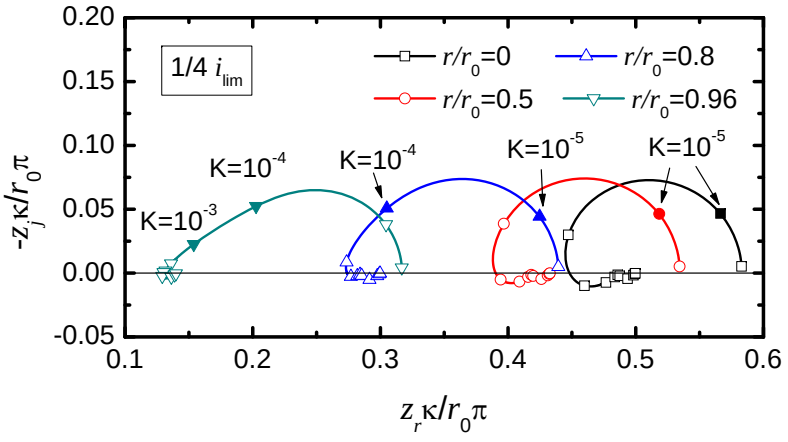

A

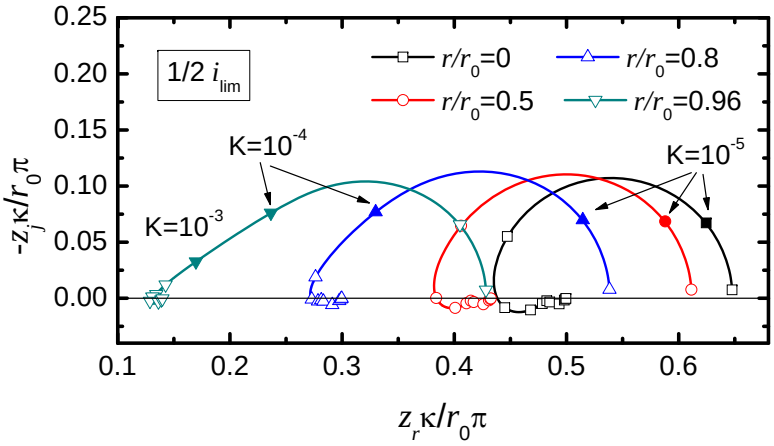

B

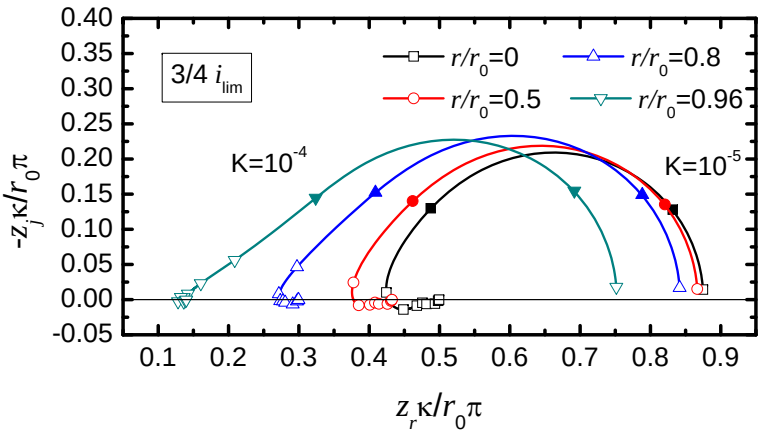

C

Figure 8-18. Nyquist representation of the local impedance for deposition of silver on a rotating disk electrode rotating at 120 rpm calculated at A) one-fourth, B) one-half, and C) three-fourths of limiting current. The electrolytic solution consists of 0.1 M $AgNO_3$ and 1 M KNO_3.

8-19, the local impedances are completely different from the global impedance. The local impedance represents the summation of the local interfacial and local Ohmic impedances. Since the values of the local interfacial impedances shown in Figure 8-13 are one order of magnitude smaller than the values of the local Ohmic impedances in Figure 8-16, the local impedances are strongly affected by the local Ohmic impedance, showing only inductive features near the center of electrode and both inductive and capacitive loops at electrode periphery. The extremely larger low-frequency loop at the disk periphery is needed to be confirmed that it is not a numerical artifact.

8.5 Effective Double-Layer Capacitance

Under the assumption that the Faradaic current and the charging current can be separated *a priori*, the flux of reactants and products are given by the rate of the electrochemical reaction. The double-layer capacitance C_0 is associated with the change of charge on electrode with the variation of interfacial potential. For electrochemical reactions dependent on mass transfer, part of the flux of reacting species contributes to the charging of the interface.

The variation of charge on electrode is also related to the variations of ionic concentration in the solution adjacent to the electrode surface. The effective double-layer capacitance that accounts for the contribution of the flux to the charging process is defined by

$$C_{\text{eff}} = C_0 + \sum_i \left(\frac{\partial \overline{q}_{\text{m}}}{\partial \overline{c}_{i,0}} \right)_{\overline{V}, \overline{c}_{j,0, j \neq i}} \frac{\widetilde{c}_{i,0}}{\widetilde{V}} \tag{8–19}$$

The first term on the right-hand side is the double-layer capacitance used in the case APS, and the second term is the contribution of flux of each species in the charging of the double layer. The effective double-layer capacitance is a function of radial potential and frequency. The values of double-layer capacitance used in the case APS and the effective capacitance obtained in the case NAPS at various radial positions are listed in Table 8-1. The radial distribution of the effective double-layer capacitance is almost uniform in solutions with an excess supporting electrolyte. For the system of reduction

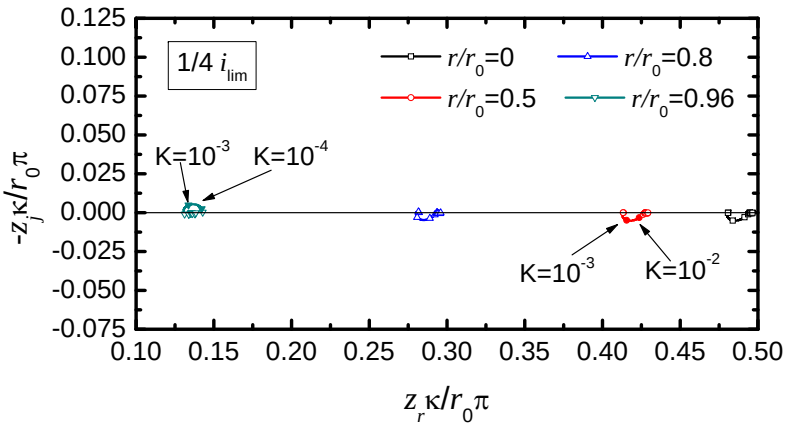

A

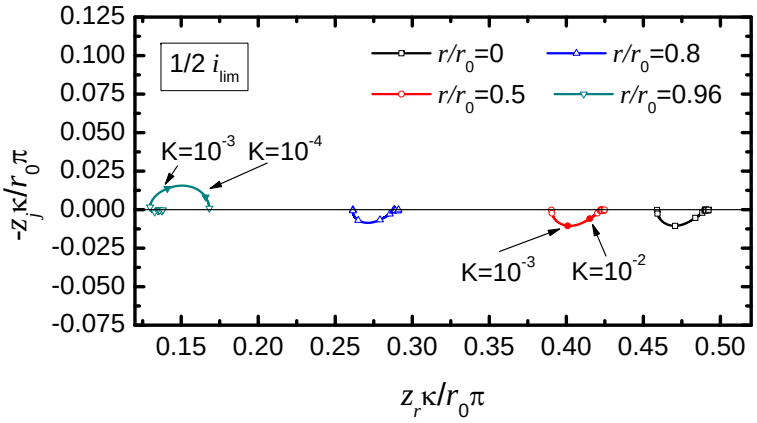

B

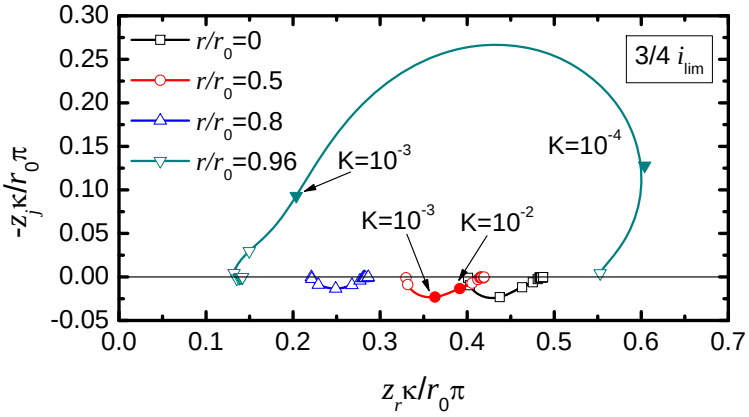

C

Figure 8-19. Nyquist representation of the local impedance for deposition of silver on a rotating disk electrode rotating at 120 rpm calculated at A) one-fourth, B) one-half, and C) three-fourths of limiting current. The electrolytic solution consisted of 0.1 M $AgNO3$ and 0.01 M KNO_3.

Table 8-1. Effective double-layer capacitance for the case NAPS at different positions on electrode and the surface-averaged double-layer capacitance for the case APS. The effective capacitance for NAPS were calculated at the characteristic frequency associated with the Faradaic reaction and the charging of the interface. The unit for the capacitance is μF/cm^2.

Electrolytic		NAPS: C_{eff}				APS
system	i/i_{lim}	$r/r_0 = 0$	$r/r_0 = 0.5$	$r/r_0 = 0.8$	$r/r_0 = 0.96$	$\langle C_0 \rangle$
$[\text{AgNO}_3] = 0.1$ M	1/4	0.0616	0.0606	0.0575	0.0501	16.9
$[\text{KNO}_3] = 0.01$ M	1/2	0.0508	0.0487	0.0428	0.0305	16.9
	3/4	0.0406	0.0373	0.0281	0.0168	16.9
$[\text{AgNO}_3] = 0.1$ M	1/4	12.9	12.9	12.9	12.9	17.1
$[\text{KNO}_3] = 1$ M	1/2	13.3	13.3	13.3	13.3	17.1
	3/4	14.1	14.1	14.1	14.1	17.1
$[\text{K}_3\text{Fe(CN)}_6] = 0.01$ M	1/4	15.8	15.8	15.8	15.8	16.7
$[\text{K}_4\text{Fe(CN)}_6] = 0.01$ M	1/2	16.0	16.0	16.0	16.0	16.7
$[\text{KCl}] = 1$ M	3/4	14.1	16.2	16.2	16.2	16.7

of ferricyanide, the values of the effective capacitance in case NAPS are closer to the values of the double-layer capacitance in case APS. For the system of silver deposition and in the presence of a small amount of supporting electrolyte, the values of the effective capacitance are about two or three orders of magnitude smaller than that of the double-layer capacitance. A smaller effective capacitance results in a smaller time constant and a larger characteristic frequency as observed in the high-frequency loop of the global and local interfacial impedances.

Figure 8-20 shows the effective double-layer capacitance as a function of frequency for the deposition of silver. In the presence of a small concentration of supporting electrolyte, the effective double-layer capacitance is strongly dependent on frequency. The values of C_{eff} at high frequencies becomes three orders of magnitude smaller than C_0. The frequency-dependent effective capacitance leads to the appearance of CPE behavior in the global and local interfacial impedances even when the solution contains an excess amount of supporting electrolyte. For the reduction of ferricyanide given in Figure 8-21, the dependence of the effective capacitance on the frequency is less significant than that in the silver deposition system. This result could

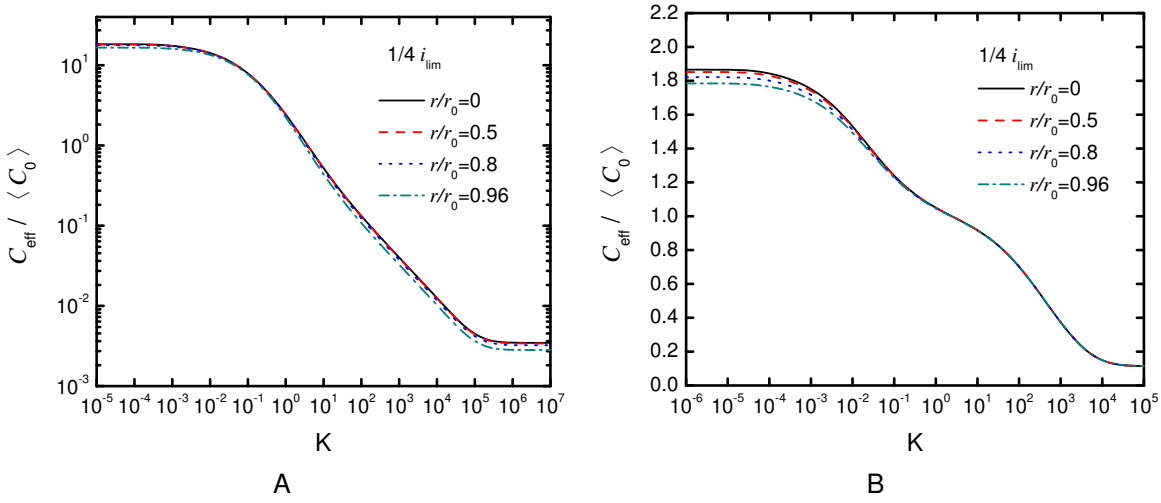

Figure 8-20. Effective double-layer capacitance for deposition of silver on a rotating disk electrode rotating at 120 rpm and at one-fourth of limiting current. The solution consists of 0.1 M $AgNO_3$ and A) 0.01 M and B) 1 M KNO_3.

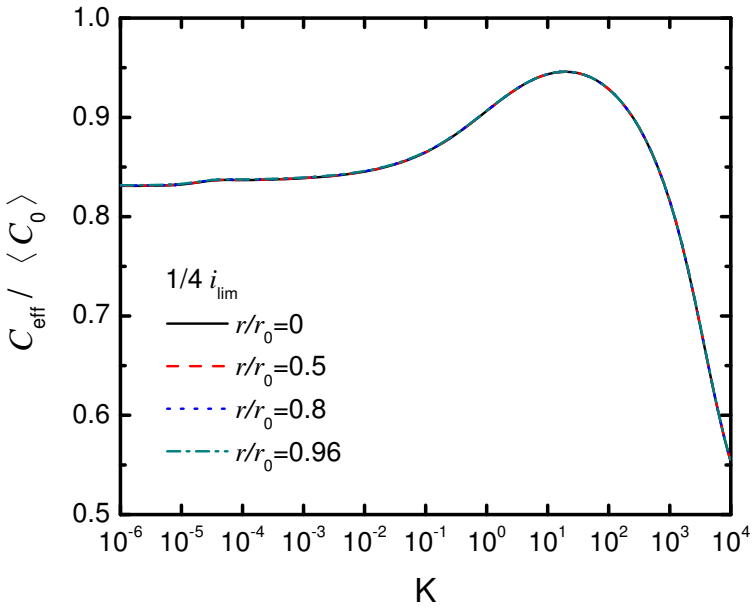

Figure 8-21. Effective double-layer capacitance for reduction of ferricyanide on a rotating disk electrode rotating at 120 rpm and at one-fourth of limiting current. The solution

Table 8-2. Comparison of results under different simulation conditions.

Electrochemical reaction	Electrode geometry	i_0 (A/cm^2)	r†	Ω (rpm)	$i/i_{\lim}$	NAPS =APS
Reduction of ferricyanide	RDE	0.3	0.93	120	1/4, 1/2, 3/4	Yes
		0.3	0.93	600	1/4, 1/2, 3/4	Yes
		0.3	0.93	2,400	1/4, 1/2, 3/4	Yes
Deposition of silver	RDE	1	0.91	120	1/4, 1/2, 3/4	No
		1	0.50	120	1/4, 1/2, 3/4	No
		1	0.091	120	1/4, 1/2, 3/4	No
		0.01	0.91	120	1/2	Yes
		0.01	0.091	120	1/2	No
	Recessed electrode	1	0.91	0	1/4	No
		1	0.091	0	3/4	No

$^\dagger \mathrm{r} = [\mathrm{Cl}^-]/[\mathrm{K}^+]$ for reduction of ferricyanide, $\mathrm{r} = [\mathrm{K}^+]/[\mathrm{NO}_3^-]$ for deposition of silver

explain the impedance responses for the reduction of ferricyanide that did not show significant difference between the cases APS and NAPS.

8.6 Discussion

Calculations were performed in different electrochemical systems and different kinetic and mass transfer conditions to examine the impedance responses under the assumptions that there is *a priori* separation and no *a priori* separation of Faradaic reaction and charging the interface. The comparison of the simulation results is given in Table 8-2. In the system of reduction of ferricyanide, the impedance responses were almost the same in cases NAPS and APS. Therefore, it is appropriate to assume that the Faradaic reaction and the double-layer charging process can be separated *a priori*. In the system of deposition of silver, the impedance results showing no significant difference in the two cases were observed only when the reaction rate is slow and when the concentration of supporting electrolyte is large. The charging process at electrodes seems to be related to the nature of the system, the reaction rate, and the amount of supporting electrolyte. A discrepancy between the impedance responses in the cases NAPS and APS was still observed on a recessed electrode, demonstrating that the CPE behavior observed in the local interfacial impedance was not due to the

nonuniform current and potential distributions. The appearance of CPE was attributed to the frequency dependent effective double-layer capacitance that accounts for the contribution of flux in charging the double layer.

While the electrode reaction rate increases with increasing surface overpotential towards the electrode periphery, the reaction rate could be limited by the mass transfer of reacting species when the surface overpotential is sufficiently large. The coupled effect of mass transfer and electrode geometry is more significant at a larger fraction of limiting current. In the solution containing a small amount of supporting electrolyte, a numerical artifact might be present near the electrode periphery due to the approach toward zero of the ion concentrations and is needed to be confirmed.

CHAPTER 9
CONCLUSIONS

The influence of current and potential distributions on the local and global impedance response is discussed in the present study. The current and potential distributions can be attributed to the electrode geometry and the nonuniform mass transfer on a rotating disk electrode below the mass-transfer-limited current. An impedance model for electrochemical systems with adsorbed intermediates is developed to study the role of geometry effect at lower frequencies. Another model is developed to investigate the mass-transfer effect in addition to the geometry effect on the impedance response.

9.1 Influence of Adsorbed Intermediates

The calculated impedance response for the system involving an adsorbed intermediate shows the influence of geometry-induced current and potential distributions at both high and low frequencies. The character of the low-frequency loop is dependent on the sign of the kinetic parameter A, which is itself a function of the interfacial potential. When $A > 0$, the low-frequency loop is inductive, and when $A < 0$, the low-frequency loop is capacitive. While high-frequency loops appearing in the local impedance are attributed to the distribution of current associated with electrode geometry, low-frequency loops associated with intermediates also show geometry-induced dispersion of the impedance response. The geometry effects are reflected in the local Ohmic impedance, which has complex behavior at both high and low frequencies. The surface coverage by intermediates is dependent on the interfacial potential which, in turn, is related to the radial position of the electrode. It has the most nonuniform distribution on the electrode when $\langle A \rangle = 0$ because the dependence on the interfacial potential is stronger in this case.

The results of the present work showed that the dispersion of time constant attributed to the disk electrode would also lead to a CPE behavior at low frequencies.

For different potentiostatic conditions, the extent of influence by electrode geometry can be observed by examining the value of $|\Delta Z_j/\Delta Z_r|$ for a particular impedance loop. When the applied potential to the electrode increases, the CPE behavior is more significant as the value of α deviates more from unity. The deviation of the low-frequency loop from the standard semicircle represents a dispersion of time constant exhibiting on the electrode surface which is a consequence of the geometry effect.

The distortion of the impedance response associated with the electrode geometry can have a significant impact on the interpretation of the resulting spectra. Depending on the value of $\langle J \rangle$, error of 10% can be found for the high-frequency loop, and error as large as 30% may be seen in identification of the low-frequency loop associated with the reaction intermediate.

The reaction mechanism for corrosion of iron is considered in the present study to comprise two successive charge-transfer steps involving one adsorbed intermediate. The local impedance measured by use of the LEIS technique shows frequency dispersion induced by the disk geometry. The low-frequency effect was more significant at the more anodic potential. Using small bielectrode for performing local impedance measurements, it was possible to observe the radial dependance of the iron electrode reactivity. The comparison between model and experiment was constrained to be qualitative only due to changes of the electrode surface during the course of the experiment. Nevertheless, the qualitative agreement confirms the predicted influences of electrode geometry on the low-frequency impedance response for reaction systems involving adsorbed intermediates.

9.2 Influence of Nonuniform Mass Transfer

The current density increases with increasing surface overpotential towards the periphery of the disk electrode, resulting a smaller local impedance that indicates a greater accessibility near the electrode periphery. When the concentration of reacting species on the electrode is sufficiently small, the reaction rate starts to be limited by

the mass transfer of reactant. The increasing overpotential no longer has an effect on the reaction rate, and the local impedance becomes larger at the periphery of the disk electrode. The mass transfer effect is more significant in the system of small concentration of supporting electrolyte. In the presence of a small amount of supporting electrolyte, an extremely large value of the local impedance at electrode periphery is observed. A numerical artifact might be present due to the approach toward zero of the ion concentrations near the electrode periphery and is needed to be confirmed.

The effects of electrode geometry and mass transfer results in the appearance of complex features in the local Ohmic impedance response. The high-frequency complex Ohmic behavior of the local Ohmic impedance is associated with the nonuniform Ohmic potential drop in solution, which is more significant when the electrode kinetics are fast. The low-frequency complex behavior is associated with the nonuniform mass transfer of reacting species to electrode, which correlates with the disk rotation speed.

Electrode process associated with Faradaic reaction and charging the interface can be observed in the local and global impedance responses at high frequencies. There are two contributions to current, *i.e.,* a Faradaic reaction and the charging of the interface. Under the assumption that the Faradaic reaction and the charging of the interface can be separated *a priori*, the flux of reactants and products are given by the rate of the electrochemical reaction. This assumption is not quite correct because part of the flux of reacting species contributes to the charging of the interface as well as to the Faradaic reaction. The application of the assumption that there is *a priori*separation of Faradaic and charging currents is justified for the reaction system of reduction of ferricyanide. In the system of deposition of silver, the assumption of NAPS is not valid unless the reaction rate is slow and the concentration of supporting electrolyte is large. The appearance of CPE observed in the local interfacial impedance cannot be attributed to the geometry-induced current and potential distributions, but was attributed

to the frequency dependent effective double-layer capacitance that accounted for the contribution of flux in charging the double layer.

CHAPTER 10
SUGGESTIONS FOR FUTURE WORK

The proposed impedance model incorporates the nonuniform mass-transfer and Ohmic potential drop on a rotating disk electrode. The assumptions that the concentration is uniform in the bulk solution and varies only in the diffusion layer are relaxed. The radial distribution of surface charge density that depends on the potential and concentration at the outer limit of diffuse layer was also discussed in the present study. The assumptions of uniform double-layer capacitance on electrode surface and negligible contribution of mass flux to the charing of the interface are also relaxed. The electrode process was modified without *a priori* separation of double-layer charging and Faradaic charging currents.

The double-layer model in the present study followed the Gouy-Chapman theory that shows an exponential decay of charge in the diffuse region. Stern's postulation of a combination of a compact ion layer in contact with metal and an outer region with loosely scattered ions was applied to estimate the distribution of charge density on the metal surface. The capacity of the compact layer was assumed to be a constant. Grahame[64] reported that the capacity of the compact layer is dependent on the charge on the electrode. The double-layer model can be modified by relaxing the assumption of a constant capacity $C_{\mathrm{m-ohp}}$. The variation of $C_{\mathrm{m-ohp}}$ with the surface charge density and the consideration of specific adsorption of species onto the metal surface can be the next step to improve the double-layer model. Also, instead of considering a continuous motion of species in the diffuse region of charge, a double-layer model with molecular-scale simulations[74] could be used to explore the charge distribution at the interface.

Furthermore, the thickness of the diffuse double layer is associated with the ionic concentration. The smaller ionic concentration gives a larger value of double-layer thickness which could lead to an error in assessing the charge distribution in the

interfacial region. The electrical double-layer model should be improved to takes into account the ionic concentration.

Under the assumption that there is no *a priori* separation of Faradaic and double-layer charging currents, the impedance responses showed a depressed semicircle at high frequencies even in the presence of an excess supporting electrolyte. Experimental verification of the impedance results is required.

REFERENCES

[1] J. S. Newman, Current distribution on a rotating disk below the limiting current, Journal of the Electrochemical Society 113 (1966) 1235–1241.

[2] I. Frateur, V. M.-W. Huang, M. E. Orazem, B. Tribollet, V. Vivier, Experimental issues associated with measurement of local electrochemical impedance, Journal of the Electrochemical Society 154 (2007) C719–C727.

[3] S.-L. Wu, M. E. Orazem, B. Tribollet, V. Vivier, Impedance of a disk electrode with reactions involving an adosrbed intermediate: Local and global analysis, Journal of the Electrochemical Society 156 (2009) C28–C38.

[4] K. Nisancioğlu, The error in polarization resistance and capacitance measurements resulting from nonuniform ohmic potential drop to flush-mounted probes, Corrosion 43 (1987) 258–265.

[5] J. S. Newman, Resistance for flow of current to a disk, Journal of the Electrochemical Society 113 (1966) 501–502.

[6] J. S. Newman, Frequency dispersion in capacity measurements, Journal of the Electrochemical Society 117 (1970) 198–203.

[7] K. Nisancioğlu, J. S. Newman, The transient response of a disk electrode, Journal of the Electrochemical Society 120 (1973) 1339–1346.

[8] K. Nisancioğlu, J. S. Newman, The transient response of a disk electrode with controlled potential, Journal of the Electrochemical Society 120 (1973) 1356–1358.

[9] K. Nisancioğlu, J. S. Newman, The short-time response of a disk electrode, Journal of the Electrochemical Society 121 (1974) 523–527.

[10] V. M.-W. Huang, V. Vivier, M. E. Orazem, N. Pébère, B. Tribollet, The apparent constant-phase-element behavior of an ideally polarized blocking electrode, Journal of the Electrochemical Society 154 (2007) C81–C88.

[11] V. M.-W. Huang, V. Vivier, I. Frateur, M. E. Orazem, B. Tribollet, The global and local impedance response of a blocking disk electrode with local constant-phase-element behavior, Journal of the Electrochemical Society 154 (2007) C89–C98.

[12] V. M.-W. Huang, V. Vivier, M. E. Orazem, N. Pébère, B. Tribollet, The apparent constant-phase-element behavior of a disk electrode with faradaic reactions, Journal of the Electrochemical Society 154 (2007) C99–C107.

[13] J.-B. Jorcin, M. E. Orazem, N. Pébère, B. Tribollet, CPE analysis by local electrochemical impedance spectroscopy, Electrochimica Acta 51 (2006) 1473–1479.

[14] I. Frateur, V. M.-W. Huang, M. E. Orazem, N. Pébère, B. Tribollet, V. Vivier, Local electrochemical impedance spectroscopy: Considerations about the cell geometry, Electrochimica Acta 53 (2008) 7386–7395.

[15] B. Tribollet, J. S. Newman, The modulated flow at a rotating disk electrode, Journal of the Electrochemical Society 130 (1983) 2016–2026.

[16] G. J. Brug, A. L. G. van den Eeden, M. Sluyters-Rehbach, J. H. Sluyters, The analysis of electrode impedances complicated by the presence of a constant phase element, Journal of Electroanalytical Chemistry 176 (1984) 275–295.

[17] Z. Lukács, The numerical evaluation of the distortion of EIS data due to the distribution of parameters, Journal of Electroanalytical Chemistry 432 (1997) 79–83.

[18] L. Young, Anodic oxide films. part 4.the interpretation of impedance measurements on oxide coated electrodes on niobium, Transactions of the Faraday Society 51 (1955) 1250–1260.

[19] R. Jurczakowski, C. Hitz, A. Lasia, Impedance of porous au based electrodes, Journal of Electroanalytical Chemistry 572 (2004) 355–366.

[20] T. Pajkossy, Impedance spectroscopy at interfaces of metals and aqueous solutions surface roughness, cpe and related issues, Solid State Ionics 176 (2005) 1997–2003.

[21] J. S. Newman, K. E. Thomas-Alyea, Electrochemical Systems, John Wiley and Sons, Inc., 2004.

[22] S.-L. Wu, M. E. Orazem, B. Tribollet, V. Vivier, Impedance of a disk electrode with reactions involving an adosrbed intermediate: Experimental and simulation analysis, Journal of the Electrochemical Society 156 (2009) C214–C221.

[23] C. Blanc, M. E. Orazem, N. Pebere, B. Tribollet, V. Vivier, S. Wu, The origin of the complx character of the ohmic impedace, Electrochimica Acta.

[24] H. Isaacs, M. Kendig, Determination of surface inhomogeneities using a scanning probe impedance technique, Corrosion 36 (6) (1980) 269 – 274.

[25] R. S. Lillard, P. J. Moran, H. S. Isaacs, A novel method for generating quantitative local electrochemical impedance spectroscopy, Journal of The Electrochemical Society 139 (4) (1992) 1007–1012.

[26] F. Zou, D. Thierry, Localized electrochemical impedance spectroscopy for studying the degradation of organic coatings, Electrochimica Acta 42 (20-22) (1997) 3293 – 3301.

[27] C. Gabrielli, F. Huet, M. Keddam, P. Rousseau, V. Vivier, Scanning electrochemical microscopy imaging by means of high-frequency impedance measurements in feedback mode, The Journal of Physical Chemistry B 108 (2004) 11620–11626.

[28] B. Levich, The theory of concentration polarization, Acta Physicochimica URSS 17 (1942) 257–307.

[29] W. G. Cochran, The flow due to a rotating disc, Mathematical Proceedings of the Cambridge Philosophical Society 30 (1934) 365–375.

[30] J. S. Newman, Schmidt number correction for the rotating disk, Journal of Pysical Chemistry 70 (1966) 1327–1328.

[31] P. Pierini, P. Appel, J. S. Newman, Current distribution on a disk electrode for redox reactions, Journal of the Electrochemical Society 123 (1976) 366–369.

[32] C. Deslouis, C. Gabrielli, P. S.-R. Fanchine, B. Tribollet, Electrohydrodynamical impedance on a rotating disk electrode, Journal of The Electrochemical Society 129 (1) (1982) 107–118.

[33] C. Deslouis, C. Gabrielli, B. Tribollet, An analytical solution of the nonsteady convective diffusion equation for rotating electrodes, Journal of The Electrochemical Society 130 (10) (1983) 2044–2046.

[34] B. Tribollet, J. S. Newman, Determination of the diffusion coefficient from impedance data in the low frequency range, Journal of the Electrochemical Society 135 (1988) 134–138.

[35] P. Appel, J. Newman, Radially dependent convective warburg problem for a rotating disk, Journal of the Electrochemical Society 124 (1977) 1864–1868.

[36] M. Durbha, M. E. Orazem, Current distribution on a rotating disk electrode below the mass-transfer-limited current, Journal of the Electrochemical Society 145 (1998) 1940–1949.

[37] M. Durbha, M. E. Orazem, B. Tribollet, A mathematical model for the radially dependent impedance of a rotating disk electrode, Journal of the Electrochemical Society 146 (1999) 2199–2208.

[38] M. Durbha, Influence of current distortions on the interpretation of the impedance spectra collected for a rotating disk electrode, Ph.D. thesis, University of Florida (1998).

[39] H. Gerischer, W. Mehl, Zum mechanismus der kathodischen wasserstoffabscheidung an quecksilber, silber und kupfer., Zeitschrift fur Elektrochemie 59 (1955) 1049–1059.

[40] A. Frumkin, Adsorptionserscheinungen und elektrochemische kinetik, Zeitschrift fur Elektrochemie 59 (1955) 807–822.

[41] E. Gileadi, B. E. Conway, Kinetic theory of adsorption of intermediate in electrochemical catalysis, The Journal of Chemical Physics 39 (12) (1963) 3420–3430.

[42] I. Epelboin, G. Loric, Sur un phenomene de resonance observe en basse frequence au cours des electrolyses accompagnees dune forte surtension anodique, Journal de Physique et le Radium 21 (1960) 74–76.

[43] R. D. Armstrong, R. E. Firman, H. R. Thirsk, The ac impedance of complex electrochemical reactions, Faraday Discussions 56 (1973) 244–263.

[44] I. Epelboin, M. Keddam, J. C. Lestrade, Faradaic impedances and intermediates in electrochemical reactions, Faraday Discussions 56 (1973) 264–275.

[45] R. D. Armstrong, K. Edmondson, The impedance of metals in the passive and transpassive regions, Electrochimica Acta 18 (1973) 937–943.

[46] C. Cao, On the impedance plane displays for irreversible electrode reactions based on the stability conditions of the steady-statei. one state variable besides electrode potential, Electrochimica Acta 35 (1990) 831–836.

[47] L. Bai, B. E. Conway, AC impedance of faradaic reactions involving electrosorbed intermediates: Examination of conditions leading to pseudoinductive behavior represented in three-dimensional impedance spectroscopy diagrams, Journal of the Electrochemical Society 138 (1991) 2897–2907.

[48] I. Epelboin, M. Keddam, Faradaic impedances: Diffusion impedance and reaction impedance, Journal of the Electrochemical Society 117 (1970) 1052–1056.

[49] L. Péter, J. Arai, H. Akahoshi, Impedance of a reaction involving two adsorbed intermediates: Alumium dissolution in non-aqueous lithium imide solutions, Journal of Electroanalytical Chemistry 482 (2000) 125–138.

[50] C. Wagner, Theoretical analysis of the current density distribution in electrolytic cells, Journal of the Electrochemical Society 98 (1951) 116–128.

[51] M. Keddam, O. R. Mattos, H. Takenouti, Mechanism of anodic dissolution of iron-chromium alloys investigated by electrode impedance I. experimental results and reaction model, Electrochimica Acta 31 (1986) 1147–1158.

[52] J. O. Bockris, D. Drazic, A. R. Despic, The electrode kinetics of the deposition and dissolution of iron, Electrochimica Acta 4 (1961) 325–361.

[53] M. E. Orazem, B. Tribollet, Electrochemical Impedance Spectroscopy, Wiley, Hoboken, N.J, 2008.

[54] B. Hirschorn, B. Tribollet, M. E. Orazem, On selection of the pertubation amplitude required to avoid nonlinear effects in impedance measurements, Israel Journal of Chemistry 48 (2008) 133–142.

[55] T. von Kármán, Uber laminare und turbulente reibung, Zeitschrift für angewandte Mathematik und Mechanik 1 (1921) 233–252.

[56] M. E. Orazem, M. Durbha, C. Deslouis, H. Takenouti, B. Tribollet, Influence of surface phenomena on the impedance response of a rotating disk electrode, Electrochimica Acta 44 (1999) 4403–4412.

[57] P. H. Daum, C. G. Enki, Electrochemical kinetics of the ferri-ferrocyanide couple on platinum, Analytical Chemistry 41 (1969) 653–656.

[58] P. Price, D. Vermilyea, Kinetics of electrodeposition of silver, Journal of Chemical Physics 28 (4) (1958) 720 – 721.

[59] D. Larkin, N. Hackerman, The Ag^{+}-Ag exchange reaction in aqueous acidic nitrate electrolyte, Journal of The Electrochemical Society 124 (3) (1977) 360–363.

[60] C. Beriet, D. Pletcher, A microelectrode study of the mechanism and kinetics of the ferro/ferricyanide couple in aqueous media: The influence of the electrolyte and its concentration, Journal of Electroanalytical Chemistry 361 (1993) 93–101.

[61] J. S. Newman, Effect of ionic migration on limiting currents, Industrial and Engineering Chemistry Fundamentals 5 (1966) 525–529.

[62] P. Delahay, Double Layer and Electrode Kinetics, New York, Interscience Publishers, 1965.

[63] J. O. Bockris, A. K. N. Reddy, Modern electrochemistry: An introduction to an interdisciplinary area, Plenum Press, New York, 1970.

[64] D. C. Grahame, The electrical double layer and the theory of electrocapillarity, Chemical Reviews 41 (3) (1947) 441–501.

[65] P. Delahay, Electrode processes without a priori separation of double-layer charging, Journal of Physical Chemistry 70 (7) (1966) 2373–2379.

[66] P. Delahay, G. G. Susbielle, Double-layer impedance of electrodes with charge-transfer reaction, Journal of Physical Chemistry 70 (10) (1966) 3150–3157.

[67] P. Delahay, K. Holub, G. G. Susbielle, G. Tessari, Double-layer perturbation without equilibrium between concentrations and potential, Journal of Physical Chemistry 71 (3) (1967) 779–780.

[68] K. M. Nisancioglu, Current distortion and mass transfer in rotating electrode systems, Ph.D. thesis, University of California, Berkeley (1973).

[69] K. Nisancioğlu, J. S. Newman, Separation of double-layer charging and faradaic processes at electrodes, Presented at the 215th ECS Meeting, Abstract No. 1075 (2009).

[70] J. H. Sluyters, On the impedance of galvanic cells i. theory, Recueil des Travaux Chimiques des Pays-Bas 79 (1960) 1092–1100.

[71] J. H. Sluyters, J. J. C. Oomen, On the impedance of galvanic cells ii. experimental verification, Recueil des Travaux Chimiques des Pays-Bas 79 (1960) 1101–1110.

[72] M. Sluyters-Rehbach, J. H. Sluyters, On the impedance of galvanic cells. vi. alternating current polarography in the complex impedance plane: general treatment, Recueil des Travaux Chimiques des Pays-Bas 82 (6) (1963) 525 – 534.

[73] M. Sluyters-Rehbach, J. H. Sluyters, On the impedance of galvanic cells vii. alternating current polarography in the complex impedance plane, experimental verification, Recueil des Travaux Chimiques des Pays-Bas 82 (6) (1963) 535 – 552.

[74] A. Oleksy, J.-P. Hansen, Towards a microscopic theory of wetting by ionic solutions. i. surface properties of the semi-primitive model, Molecular Physics 104 (2006) 2871–2883.

BIOGRAPHICAL SKETCH

Shaoling Wu's interest in the field of electrochemistry started from her junior year at the National Taiwan University. Since then she joined the Electrochemical Engineering Lab and worked on an undergraduate research project involving the characterization of nano-particles used in the slurry of chemical mechanical polishing process. She received the Bachelor of Science degree in Chemical Engineering from the National Taiwan University in June, 2004. Shaoling pursued her study in the same group and worked on the development of metallization by integrating electroless plating and ink-jet printing technology. After she received the Master of Science degree in June of 2006, she entered the graduate school at the University of Florida. Shaoling joined the research group under the direction of Professor Mark Orazem in January, 2007. She has been working on the research project in collaboration with the CNRS Laboratory in Paris for the numerical simulation of the influence of electrode geometry on impedance response. Shaoling graduated in the summer of 2010 with a Ph.D. in Chemical Engineering.